TRIPLET FUSION PHOTON UPCONVERSION SYSTEMS:

TOWARDS LOW THRESHOLD APPLICATIONS

A Dissertation
Presented to
The Academic Faculty

by

Ji-Hwan Kang

In Partial Fulfillment
of the Requirements for the Degree
Doctor of Philosophy in the
School of Chemical & Biomolecular Engineering

Georgia Institute of Technology

May 2017

TRIPLET FUSION PHOTON UPCONVERSION SYSTEMS:

TOWARDS LOW THRESHOLD APPLICATIONS

Approved by:

Dr. Elsa Reichmanis, Advisor
School of Chemical & Biomolecular Engineering
Georgia Institute of Technology

Dr. Sven H. Behrens
School of Chemical & Biomolecular Engineering
Georgia Institute of Technology

Dr. Dennis W. Hess
School of Chemical & Biomolecular Engineering
Georgia Institute of Technology

Dr. Bernard J. Kippelen
School of Electrical & Computer Engineering
Georgia Institute of Technology

Dr. William J. Koros
School of Chemical & Biomolecular Engineering
Georgia Institute of Technology

Date Approved: March 15th, 2017

This dissertation is dedicated to my family.

ACKNOWLEDGEMENTS

First and foremost, I would like to express my sincere appreciation to my advisor, Dr. Elsa Reichmanis, for all her strong support and guidance throughout my Ph.D. years. Without her, I would not be here. She has always encouraged me whenever I was in trouble with any academic or research concerns so that I could continue my work without frustration. I will keep in mind her valuable advice always.

I also want to thank my Ph.D. thesis committee, Dr. Dennis W. Hess, Dr. William J. Koros, Dr. Seven H. Behrens, and Dr. Bernard J. Kippelen who have advised me in all of the steps with their helpful comments during my Ph.D. They allowed me to broaden my perspective and contribute to my personal development by expanding my knowledge with high level of completion.

I wish to thank most sincerely the previous group members, Dr. Zhaokang Hu, Dr. Avishek Aiyar, Dr. Mincheol Chang, Dr. Boyi Fu, Dr. Dalsu Choi, Dr. Nabil Kleinhenz, Ashwin Ravi-Sankar, Jiho Lee, Dr. Cornelia Rosu and Dr. Gang Wang, and the current group members, Ping-Hsun Chu, Jeff Hernandez, Nils Persson, Rui Chang, Zhibo Yuan, Yo Han Kwon, Bailey Risteen, Mike McBride, Giovanni DeLuca, Krysten Minnici, Brian Khau and Dr. Guoyan Zhang for their valuable help and discussions.

Over the years, I have had opportunities to collaborate with other research groups, Dr. Jun Hyuk Moon at Sogang University (with Su-Jin Ha), Dr. Shin-Hyun Kim at KAIST (with Sang Seok Lee), Dr. Alberto Fernandez-Nieves at Georgia Tech (with Dr. Josefa Guerrero-Millan) and Dr. Ali Adibi at Georgia Tech (with Dr. Ali A.Eftekhar).

We have worked together a lot and it has been a great time to have unexpected experience and engage in learning from them.

I would like to express special thanks to all the friends I met in ChBE during my Ph.D, especially the Korean Student Association for their strong friendship and support to living in this community.

Finally and most importantly, I would like to express my sincere gratitude to my family for their continuous support and encouragement, especially my wife, Sowon, for her love, faith and understanding. It is to her and to my son and daughter, Insung & Chloe, that this work is dedicated.

TABLE OF CONTENTS

LIST OF FIGURES

SUMMARY

Photon upconversion (UC), a promising anti-Stokes process that can convert two or more photons with low energy to a single photon of higher energy, can be readily achieved via triplet fusion or triplet-triplet annihilation (TTA) using low incident power density. To facilitate energy migration required for TTA-based upconversion systems, triplet exciton diffusion of the chromophores within an inert medium is of paramount importance, especially for practical device integration. However, the majority of studies have been carried out where the conditions have limitations such as deoxygenated organic solvents and bulk polymer matrices. The research objective here, therefore, is to find effective ways to apply active UC materials into potential devices powered by sunlight.

In this thesis, we will investigate how to improve the diffusion-limited energy transfer in TTA-UC processes and demonstrate diverse approaches to enhance their optical properties in terms of materials science and engineering perspectives. First, we will discuss two microfluidics-based approaches which allow for the controlled formation of uniform microcapsules that contain a chromophore-embedded solution core. One is photo-induced interfacial polymerization and the other is multiple emulsion encapsulation using coaxially focused glass capillaries. These core-shell structures provide high quantum yields due to the preservation of molecular mobility in the fluidic phase, as well as structural rigidity and photochemical stability. In addition, we will address alternative photon energy manipulating approaches using the tunable interference structure of cholesteric liquid crystals and surface plasmon resonance coupling of gold

nanorods to increase TTA-UC emission intensities and tailor the resultant optical properties.

CHAPTER 1. INTRODUCTION

1.1 Photophysical Processes

Light is an electromagnetic radiation, i.e. an electric field that oscillates in both time and space and a corresponding orthogonal magnetic field that oscillates with the same spatial and temporal periodicity. When a molecule interacts with light, and energy is absorbed, the molecule is said be excited and a transition occurs which can take that molecule from an initial state to a higher energy state. According to the energy conversion law, a transition is accompanied by absorption of a photon with the energy.[1]

$$h\nu = E_{excited\ state} - E_{ground\ state} \quad (1)$$

where $h\nu$ is the energy of the photon corresponding to the energy gap between the states.

Photophysical processes refer to a number of physical processes induced by the absorption of light that do not lead to overall changes in the chemical identity of the molecules. This includes generation of excited states, transitions between the excited and ground states, relaxations to the ground state, and energy transfer to a new level. The photophysical processes between the electronic states are usually illustrated by a Jablonski diagram,[2] as shown in **Figure 1.1**. The singlet ground, first and second electronic excited states are depicted by S_0, S_1 and S_2, respectively. The purple or blue arrow indicates a transition between states to illustrate the instantaneous nature of light absorption which occurs on a time scale of around 10^{-15} sec. Because the mass of the electron is much less than that of the nuclei, a good approximation is that the nuclei remain fixed on the time scale of light absorption and then relax to new equilibrium

geometries subsequent to the absorption process (Frank-Condon principle).[3-4] An atom or molecule in the ground state can absorb a photon that will allow it to be excited to a higher energy level excited state, either S_1 or S_2. At each of these electronic energy levels, the molecules can exist in a number of vibrational energy levels.

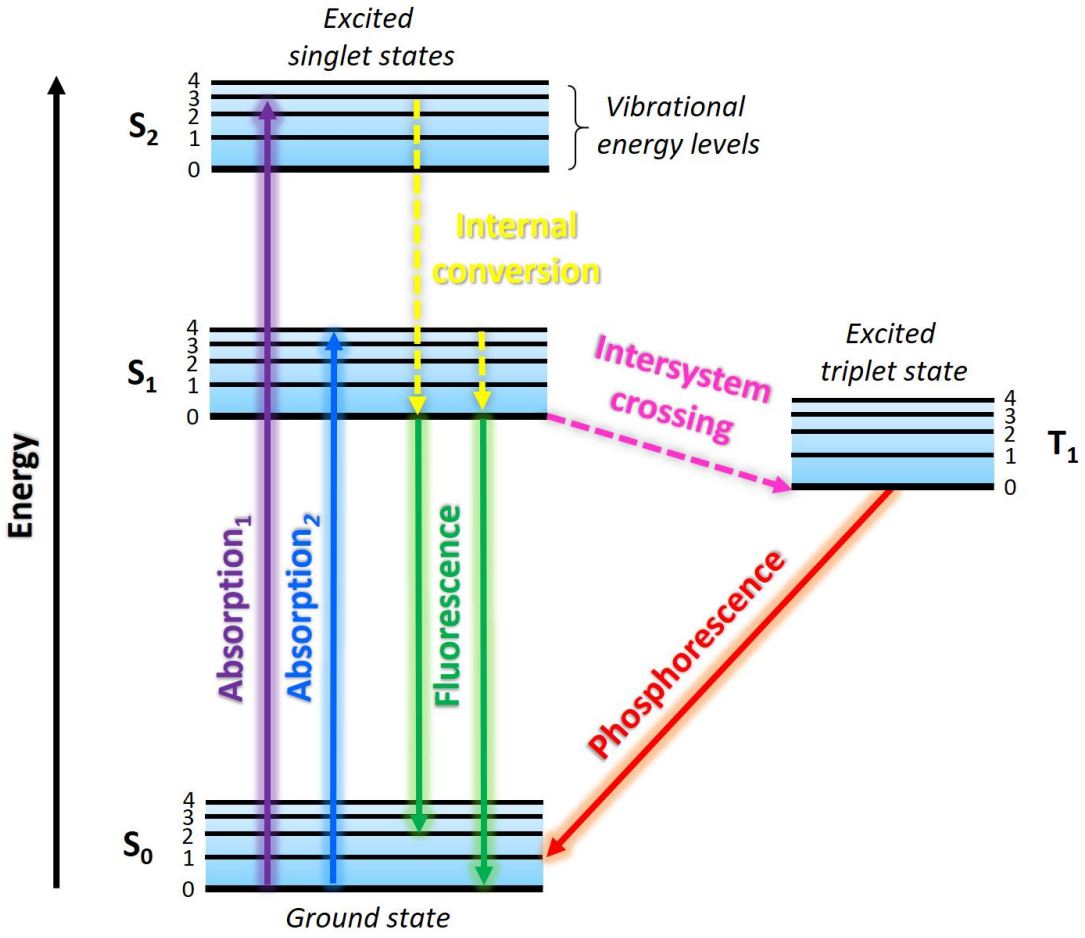

Figure 1.1. Typical Jablonski energy level diagram of photophysical processes.

Following light absorption, several subsequent processes usually occur. According to Kasha's rule,[5] the excited molecules rapidly relax to the lowest vibrational levels of S_1 without emission of a photon. This process, known as internal conversion (IC), generally occurs within 10^{-12} sec. The molecules in the S_1 state will return to the

singlet ground state through fluorescence emission, called the Stokes shift.[6] Since the fluorescence lifetimes are typically near 10^{-8} sec, it generally occurs after the internal conversion, which is determined as a difference between the position of the maxima of the absorption and emission spectra. Return to the ground state typically occurs to a higher excited vibrational ground state level, which then quickly reaches thermal equilibrium. The molecules in the S_1 state can also undergo a spin conversion process known as intersystem crossing (ISC) to the first triplet state T_1. Then, the molecules in the T_1 state relax to the singlet ground state through emission termed phosphorescence, which is generally shifted to longer wavelengths relative to the fluorescence. Because the transition between triplet and singlet involves two states of different multiplicity, the quantum yield of phosphorescence is several orders of magnitude smaller than that for fluorescence. Also, this process is much slower than fluorescence since it is quantum mechanically forbidden. Often its rate constant is so small that it cannot be observed, because other processes deactivate T_1 before phosphorescence can occur. However, molecules containing heavy atoms are frequently phosphorescent. The heavy atoms facilitate intersystem crossing and thus enhance phosphorescence quantum yields.

1.2 Intermolecular Electronic Energy Transfer

Electronic energy transfer (EET) occurs via a bimolecular quenching mechanism between two light-sensitive molecules in media.[7] It could take place via the interaction between an excited molecule as the donor (D*) and a ground state molecule as the acceptor (A) without emitting a photon when transferring energy. During the absorption process, the donor is excited to a higher vibrational level of its first electronic excitation state. From there, it is converted to a lower vibrational level of the same electronic state by obtaining thermal equilibrium with the surrounding medium. A donor molecule in its electronic excited state may transfer energy to an acceptor chromophore through either non-radiative long-range dipole-dipole coupling known as Förster (or fluorescence) resonance energy transfer (FRET) or electron exchange in short distances known as Dexter energy transfer (DET). In both cases, interactions between the donor and acceptor are a requirement either within a single bifunctional molecule or between adjacent molecules. The rate constant for EET is given by the equation below:[8]

$$k_{EET} = \frac{2\pi}{\hbar} V_{DA}^2 \rho_{DA} \qquad (2)$$

where V_{DA} contains both the electronic coupling and the Franck-Condon factors for the transition and ρ_{DA} is the density of states. This general equation describes the rate constant as the probability of a transition per unit time.

1.2.1 Förster resonance energy transfer

The first observation of a long-range energy transfer was made by Cario and Franck in their experiments on sensitized fluorescence of atoms in a mixture of mercury

and thallium vapor.[9] Afterwards, the sensitized fluorescence of molecules in solution was proposed by J. Perrin, and is a mechanism that is being used more and more in a variety of fields such as biomedical research and drug delivery today.[10] The mechanism of FRET involves a sensitizer molecule in an excited electronic state, which may transfer its excitation energy to a nearby acceptor molecule in a non-radiative fashion through long-range dipole-dipole coupling (Coulombic) interactions.[10] To provide large probability of resonance paths for FRET, there are a few criteria that must be satisfied: 1) a good spectral overlap between the fluorescence emission of the donor and the excitational absorption of the acceptor and 2) close proximity of the two fluorophores (typically 10-100 Å). The efficiency of the FRET process depends on the inverse sixth power of the distance (r) between the donor and acceptor and is given by

$$\eta_{FRET}(r) = \frac{1}{1 + (r/R_0)^6} \tag{3}$$

where R_0 is the Förster radius at which half of the excitation energy of donor is transferred to the acceptor. There are no spin restrictions, so the energy transfer can be efficient in both singlet-singlet transfer and singlet-triplet transfer. The schematic diagram of FRET is shown in **Figure 1.2**.

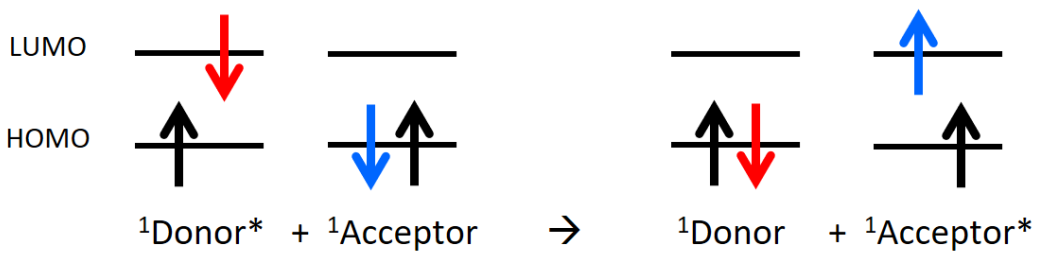

Figure 1.2. Schematic diagram for Förster resonance energy transfer between the excited singlet state of donor and ground singlet state of acceptor.

1.2.2 Dexter energy transfer

The mechanism of Dexter energy transfer is a quantum mechanical effect and arises because of the symmetry requirement of electronic wave functions with respect to exchange of space and spin coordinates of any two electrons simultaneously in the donor or acceptor complex (intermolecular orbital overlap).[11-12] Therefore, it can occur only as a short-range phenomenon (typically within 10 Å). The transfer occurs at a diffusion-controlled rate. For efficient Dexter energy transfer, there should be an effective overlap of electron orbitals between the donor and acceptor: the overall spin of the system should not change after the energy transfer. As a result, the Dexter mechanism is highly efficient for singlet-singlet and triplet-triplet energy transfer. The schematic diagram of Dexter energy transfer is shown in **Figure 1.3** and the details will be further described in Chapter 1.4.5.

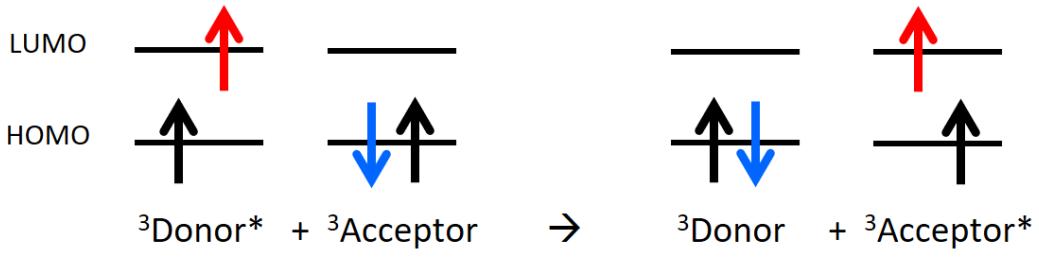

Figure 1.3. Schematic diagram for Dexter energy transfer between the excited triplet state of donor and ground triplet state of acceptor.

1.3 Photon Energy Upconversion

Photon upconversion (UC) is an anti-Stokes emission process that converts two or more low energy photons (from incident light) to a single higher energy photon. For an example of the frequency amplification as shown in **Figure 1.4**, fluorescence emission of short wavelength light (green) was observed under irradiation at a longer wavelength (red).

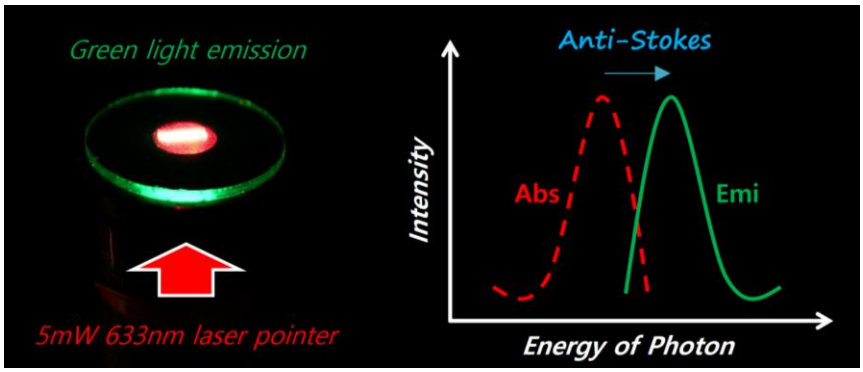

Figure 1.4. Anti-Stokes emission with higher energy photons via photon upconversion

The anti-Stokes shift is promising because of its potential applications in photosensitive devices, including photovoltaics,[13-17] photocatalyst systems,[18-20] photochromic displays,[21-22] and biological imaging,[23-26] as shown in **Figure 1.5**. However, conventional UC systems based upon nonlinear phenomena such as two-photon absorption (TPA) and second-harmonic generation (SHG) require very high excitation power densities ($MWcm^{-2}$-$GWcm^{-2}$), and as a result may be undesirable for low threshold applications.[27-28] Alternatively, lanthanide-doped upconversion, typically classified by excited state absorption (ESA) or energy transfer upconversion (ETU), has

emerged due to its use of physically existing intermediate energy states, resulting in high conversion efficiency with relatively lower density excitation sources ($kWcm^{-2}$).[29-30] However, efficient upconversion is restricted to very few rare-earth activators, and their several orders of magnitude smaller absorption cross-sections in spectral regions of interest relative to organic dyes still remain as a big challenge.[27]

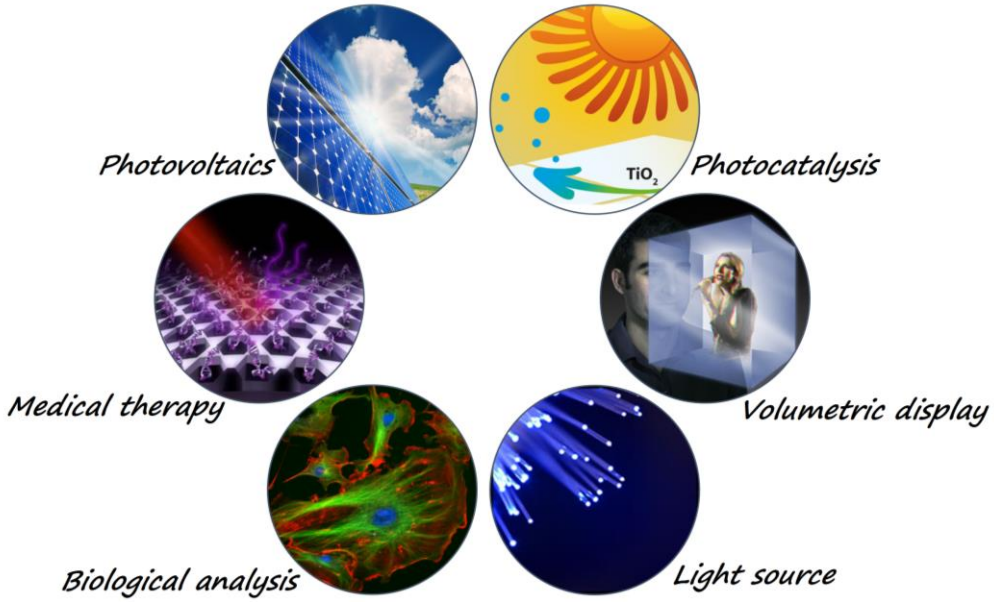

Figure 1.5. Potential applications of photon upconversion

1.4 Triplet-Triplet Annihilation

An attractive alternative for UC approach uses a triplet fusion or triplet-triplet annihilation (TTA) based process which allows the use of low-power density ($mWcm^{-2}$) noncoherent continuous-wave excitation, e.g. sunlight (100 $mWcm^{-2}$, AM 1.5G).[31-34] Although TTA-sensitized UC was first introduced by Parker and Hatchard in the early 1960's,[35-36] this phenomenon was only sparingly investigated over the subsequent decades because the noncovalent organic systems whose triplet sensitizers exhibited low intersystem crossing yielded only limited upconverted fluorescence efficiency. However recently, many research groups have demonstrated that the incorporation of metal-organic chromophores can markedly enhance upconversion yield since the sensitizer triplet state can be populated with high efficiency upon absorption of light.[28, 31] Most recently, this UC method was proposed to be integrated into a solar cell to overcome the theoretical power efficiency limit.[16, 37]

1.4.1 Photon upconversion based on triplet-triplet annihilation

The TTA approach typically uses an organometallic complex and an aromatic hydrocarbon as the sensitizer and emitter, respectively. Upon irradiation, the metal-to-ligand charge-transfer (MLCT) characteristics of the sensitizer enables its long-lived triplet excited state by enhancing the intersystem crossing (ISC) rate,[38] which results in triplet-triplet energy transfer (TTET) from the sensitizer to the acceptor. With the increased population of triplet acceptors, there becomes large probability that two triplet excited acceptor molecules then undergo TTA through direct collision, which leads to subsequent generation of one singlet excited state, producing the upconverted

fluorescence upon decay to the ground state. This sensitized TTA mechanism involves the transfer of energy between a donor and an acceptor. Hence, several factors are considered when determining the proper combination of chromophores in a viable upconverting system.[22] A schematic representation of the TTA-UC process in a static condition is shown in **Figure 1.6**.

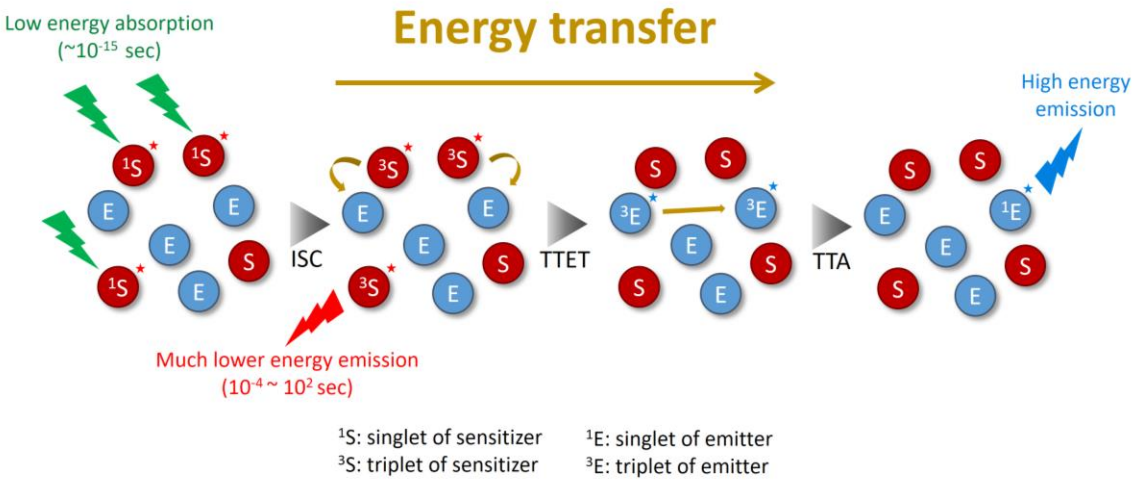

Figure 1.6. Schematic photophysical processes of bimolecular photon upconversion between the sensitizer and emitter upon low energy absorption to produce high energy emission in a static condition: ISC, TTET and TTA stand for intersystem crossing, triplet-triplet energy transfer and triplet-triplet annihilation, respectively.

1.4.2 Requirements for TTA-based upconversion

After long wavelength selective excitation of the sensitizer, TTA-based upconversion must be considered as an inherently connected chain of three processes[31] as shown in the energy level diagram of **Figure 1.7**.

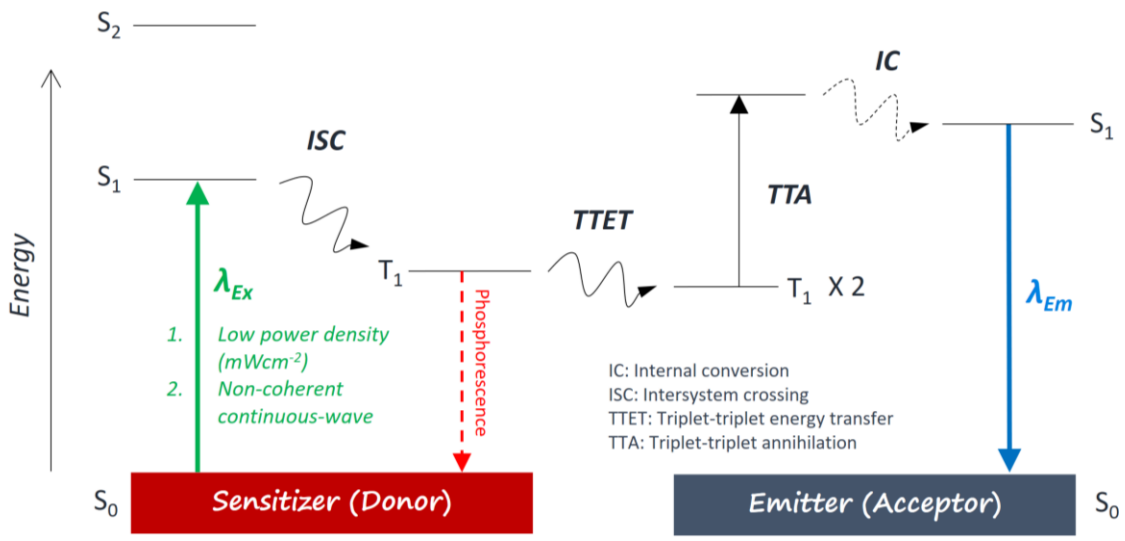

Figure 1.7. Generalized Jablonski energy level diagram of the bimolecular photon upconversion process via sensitized triplet-triplet annihilation leading to the delayed fluorescence.

The first process in the chain is the ISC, which is strongly enhanced by spin-orbit coupling to the metal center of metallated macrocyclic sensitizer molecules.[5] Efficient ISC within the sensitizer molecules ensures a high population of the sensitizer triplet level via single photon absorption. On the other hand, the very weak ISC of the emitter molecules substantially prohibits the depopulation of the excited emitter triplet states via phosphorescence and thus preserves the created triplet population of the emitter for the process of TTA. Therefore, a large difference between the ISC coefficients of the sensitizer and emitter molecules is required.[22]

$$C_{sensitizer}^{ISC} \gg C_{emitter}^{ISC} \quad (4)$$

The second process in the chain is energy transfer of the excitation of the sensitizer triplet to the emitter triplet, which is called triplet-triplet energy transfer

(TTET). The efficiency of the TTET is predetermined by the extent of overlap of the sensitizer and emitter triplet manifolds.[39]

$$E_{sensitizer}^{triplet^*} >\cong E_{emitter}^{triplet^*} \quad (5)$$

The third process is the subsequent TTA.[36] As a precondition for efficient energetically conjoined TTA-UC, there are two requirements related to the molecular structures of the sensitizer and the emitter molecules. The combined triplet energy level from two excited emitter molecules is greater than or equal to the first excited singlet state of the emitter molecule without using thermal energy.

$$2\, E_{emitter}^{triplet^*} \geq E_{emitter}^{singlet^*} \quad (6)$$

The final requirement for the UC system relates to the structure of the sensitizer absorption spectrum. In order to reduce the re-absorption of the generated UC emission from sensitizer molecules which are in the ground state, there should be a large enough transparent window. Metallated macrocycles such as porphyrins have band-like absorption spectra grouped around two strong bands, which are the Soret- and Q-bands. Therefore, photons with energies lying sufficiently far away from those two absorption maxima will be absorbed less by a sensitizer molecule, and the position of the first excited singlet state level of the emitter should not overlap with the absorption maximum of the sensitizer.

$$E_{sensitizer}^{Soret-band} > E_{emitter}^{singlet^*} \gg E_{sensitizer}^{Q-band} \quad (7)$$

As long as these specific energy criteria are met, the conditions are appropriate for the observation of anti-Stokes upconverted fluorescence.

Sensitizers are selected based on their ability to absorb light in the visible-to-near-IR region of the spectrum allowing for low energy excitation, and must possess a relatively long triplet excited state lifetime, typically on the order of several microseconds and beyond. This is necessary to allow for bimolecular diffusional energy transfer. The greater the energy difference between the triplet sensitizer and triplet acceptor, the greater the driving force for this reaction and the more favorable the triplet energy transfer process. The anti-Stokes shift is defined as a fluorescence emission band that is displaced to a higher energy with respect to the excitation wavelength. A large anti-Stokes shift is observed as the distance between the excitation wavelength and the maximum of the acceptor's singlet emission increases. When the two triplet states of the acceptor combine through triplet-triplet annihilation, one goes to the ground state while the other is excited to a singlet state double the energy of the acceptor triplet state. That state relaxes down to the acceptor's lowest energy singlet excited state, which must be higher than the singlet state of the donor. It is also advantageous to use acceptors/annihilators with near unity fluorescence quantum yield since this value ultimately contributes to the overall upconversion quantum efficiency.

1.4.3 Spin statistical factors

TTA is the photophysical process that involves interactions between two excited triplet states of acceptor molecules. Spin statistical factors are considered to play an important role in determining the efficiency of the process, leading to simultaneous

transitions in both molecules. Higher excited spin allowed products, encounter complexes $(AA)^*$, are formed between a pair of excited triplet molecules when they collide with each other. The complex is not stable, and it will dissociate into one of nine spin states with equal probability: one singlet ($^1A_0{}^*$), three triplets ($^3A_1{}^*$) and five quintets ($^5A_2{}^*$).[40-41] These sublevels showing the excited state interactions between acceptor molecules are described in the below equations:

$$\begin{aligned} {}^3A_1{}^* + {}^3A_1{}^* &\leftrightarrow {}^5(AA)_2{}^* \leftrightarrow {}^5A_2{}^* + {}^1A_0 \\ {}^3A_1{}^* + {}^3A_1{}^* &\leftrightarrow {}^3(AA)_1{}^* \leftrightarrow {}^3A_1{}^* + {}^1A_0 \\ {}^3A_1{}^* + {}^3A_1{}^* &\leftrightarrow {}^1(AA)_0{}^* \leftrightarrow {}^1A_0{}^* + {}^1A_0 \end{aligned} \quad (8)$$

where $^3A_1{}^*$ is an excited triplet state, $^5A_2{}^*$ is an excited quintet state (which is not observed for organic molecules), $^1A_0{}^*$ is an excited singlet state and $^1A_0$ is the ground state. $^{1,3,5}(AA)^*$ denote doubly excited states of excimers which then dissociate into corresponding monomers.

Accordingly, the statistical factors predict a quantum yield for upconversion to be a maximum of 11.1 % (by generating a singlet state of the acceptor in a triplet-triplet annihilation process) if the quenching efficiency and fluorescence quantum yield of the acceptor is 100 %.[41] Although theoretically predicted, it is also noted that the quintet has a 92 % chance of decaying into two molecules as the excited triplet state.[40] Therefore, it follows that the upconversion yield can be higher than previously expected. The excited triplet states are likely recycled from quintet and triplet dimers. Instead of the predicted 11.1%, the quantum efficiency of triplet-triplet annihilation has approached an upper

limit exceeding 40 %.[42]

1.4.4 Excitation power dependence: quadratic-to-linear

In general, emission intensity of upconversion based on sensitized TTA possesses a quadratic dependence on incident light power as TTA-UC is initiated by two sequential photon absorptions. This power dependence is typically evaluated in steady-state photoluminescence experiments using a variety of either coherent (i.e. laser) or non-coherent (i.e. lamp) excitation sources that can vary in irradiance over many orders of magnitude. However, it has recently been shown that this observation results when experiments are performed in the weak-annihilation kinetic limit and most of the sensitized triplets decay prior to fusion.[43] Utilizing either continuous wave or high powered pulse ultrafast lasers, it has been demonstrated that a linear power law can be achieved also. In the latter regime, highest possible quantum efficiency for the specific composition can be realized since the emission intensity of upconversion is directly proportional to the number of excited triplet states.[44]

Sensitized TTA-UC processes require absorption of two photons for emission of every one photon. As a result, the upconversion does not have a simple linear dependence on light intensity.[31] Related to intensity of the upconverted fluorescence, therefore, the concentration of triplet acceptors is a function of two competing rates for the mechanism of the quadratic-to linear power dependence. There are two kinetic limits that are related to the $^3A^*$ decay, as shown in the equations below.

$$\frac{d[^3A^*]}{dt} = -k_T[^3A^*]_t - k_{TT}[^3A^*]_t^2 \quad (9)$$

$$N_F = \int_0^\infty I_F(t)dt \; = \; \int_0^\infty \emptyset_F k_{TT} \, [^3A^*]_t^2 \, dt \tag{10}$$

The intensity of delayed fluorescence (N_F) is proportional to the square of the population. In the equation, k_T represents all the unimolecular and pseudo-first-order decay pathways for $^3A^*$, k_{TT} is the TTA bimolecular rate constant, and $\emptyset_F$ is the fluorescence quantum yield of the acceptor.[43] The analytical solution from Bachilo and Weisman[45] is presented by the below equations.

$$[^3A^*]_t = \; [^3A^*]_0 \frac{1-\beta}{e^{k_T t} - \; \beta} \tag{11}$$

The dimensionless parameter β equals the fraction of initial decay that occurs through the second-order channel.

$$\beta = \; \frac{k_{TT} \, [^3A^*]_0}{k_T + \; k_{TT} \, [^3A^*]_0} \tag{12}$$

In the weak annihilation limit, $k_T \gg \; k_{TT} \, [^3A^*]_0$, first order decay to the ground state is the dominant relaxation pathway for $^3A^*$. Therefore, equation (11) can be reduced to equation (13) This is substituted into equation (10) and integrated with respect to time in order to produce equation (14)

$$[^3A^*]_t = \; [^3A^*]_0 e^{-k_T t} \tag{13}$$

$$N_F = \frac{\emptyset_F k_{TT} [^3A^*]_0^2}{2k_T} \tag{14}$$

The total upconverted fluorescence intensity is proportional to $[^3A^*]_0^2$, the square of the

triplet acceptor population, which means it has a quadratic dependence on excitation light intensity. Therefore, in the low power region, the intensity of upconversion emission is quadratic with respect to the absorbed optical power.

In the strong annihilation limit, $k_T \ll k_{TT}\,[^3A^*]_0$, TTA becomes the dominant relaxation pathway for $^3A^*$. Equation (11) can be reduced to equation (15). This is substituted into the equation (10) and integrated with respect to time in order to produce equation (16)

$$[^3A^*]_t = \frac{[^3A^*]_0}{1 + k_{TT}\,[^3A^*]_0 t} \tag{15}$$

$$N_F = \emptyset_F [^3A^*]_0 \tag{16}$$

As shown in the strong annihilation limit where the efficiency of TTA becomes maximized, the total emission intensity is linearly proportional to $[^3A^*]_0$ and should directly scale with the absorbed optical power. It is desirable for the process to operate under this condition limit. This exploration into the linear regime does not disprove previous kinetic analysis of the delayed fluorescence, but instead shows consistency with kinetic treatments proven over 40 years ago by Birks and Parker.[43]

From the kinetic analysis study, we conclude that highly efficient TTA-UC can be achieved in the strong annihilation limit by reducing the pseudo-first-order quenching process. The pumping wavelength and the associated sensitizer optical densities, along with the triplet state of the acceptor in photophysical processes, are also of vital importance. Although the intrinsic decay rate of $^3A^*$ cannot be changed, the k_T term

shows the pseudo-first order quenching of $^3A^*$ due to the dissolved oxygen in the medium. Thus, complete exclusion of oxygen from the system is the way to minimize k_T. This is the reason that vacuum degassed or purged solvents as well as oxygen impermeable host media are widely used. Assuming that TTET quenching has already reached the saturation regime, maximizing $k_{TT}\,[^3A^*]_0$ is afforded by increasing the concentration of $^3A^*$, either by increasing the absorbance of the sensitizer or the intensity of the excitation light. More importantly, using low viscous media which facilitates molecular mobility enables reaching the linear dependence even at low power density excitation such as sunlight.

1.4.5 Kinetics of collisional quenching for diffusion-controlled energy transfer

In this bimolecular system, the overall efficiencies of the delayed fluorescence process are mainly limited by two diffusion-limited steps involving energy transfer between molecules in a given medium: TTET and TTA, as shown in **Figure 1.8**.

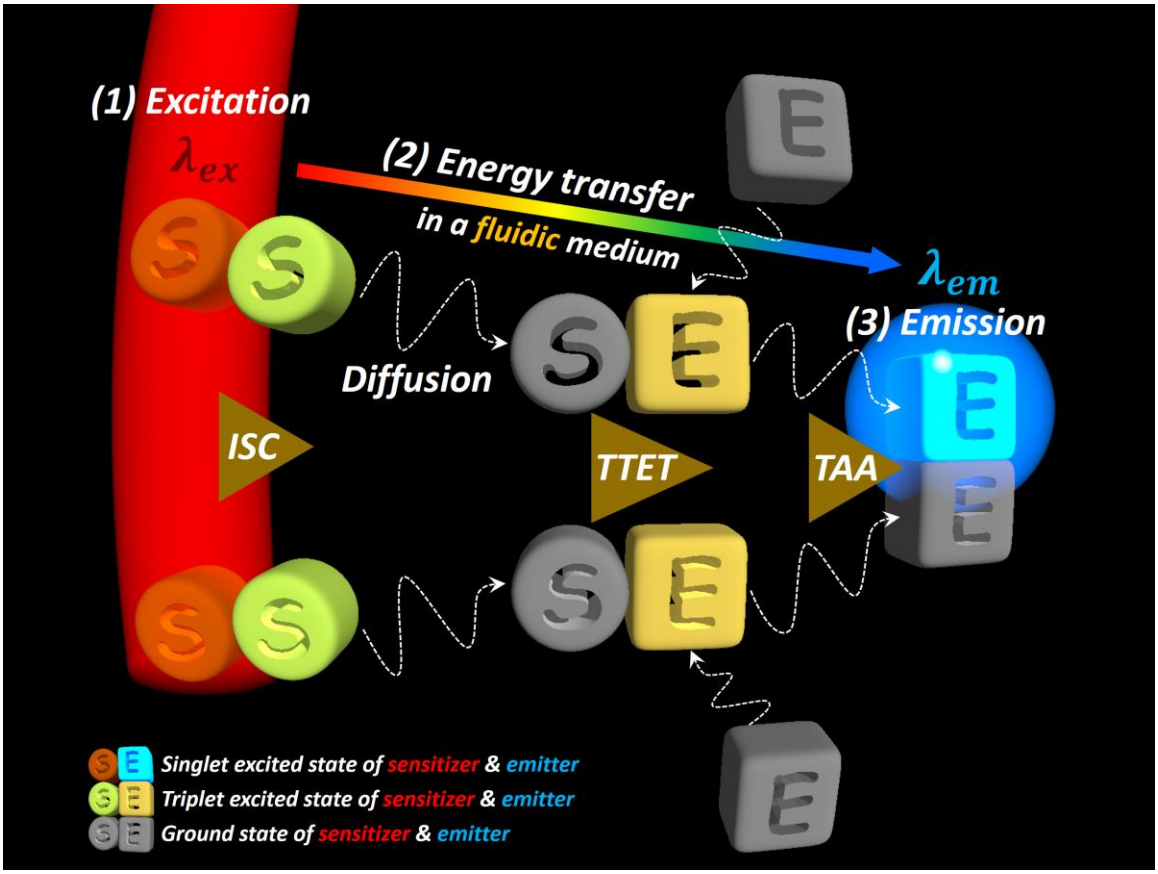

Figure 1.8. A schematic process of collisional quenching for diffusion-controlled energy transfer in a fluidic medium.

When metastable or forbidden transitions are involved in the process, resonant energy transfer takes place via exchange interaction, so called Dexter energy transfer,[11] provided that a good match between relevant energy levels of donor and acceptor exists. Unlike the sixth-power dependence of Förster energy transfer,[46] only spatial overlap between the donor and acceptor wave functions is required. In such a case, the energy transfer rate (k_{ET}) at distance R can be written as

$$k_{ET}(R) = \frac{2\pi}{\hbar} K^2 \exp\left(-\frac{2R}{L}\right) \int F_D(E) G_A(E) dE \qquad (17)$$

where F_D and G_A are the normalized donor (*D*) emission and acceptor (*A*) absorption spectra, respectively; *K* is a constant with the dimension of energy and *L* is the effective average Bohr radius, which measures the special extent of the donor and acceptor wave functions. The rate equation shows the distance dependence as a consequence of the wave function exponential decays in the space between the two parties.

As a simplified approach, the Perrin model implies an extremely fast rate at short distance ($R << L$), while the rate becomes negligible at $R > L$. Therefore, the Perrin approximation assumes there is 'an active quenching spherical radius (R_0)' for each isolated pair interaction under static conditions.[47] The Dexter radius can be obtained from measurements of photoluminescence (PL) relative to the quantum yield of the donor which is defined as the ratio between the donor PL intensity (*I*) in the presence of a defined acceptor concentration (C_A) and that (I_0) without the acceptor. This relative quantum yield[48] in the Perrin model can be written as

$$I/I_0 = \exp\left(-\frac{C_A}{C_0}\right) \tag{18}$$

or

$$\ln(I_0/I) = K_p C_A \tag{19}$$

$$K_p = 1/C_0 = (4/3)\pi {R_0}^3 N_A \tag{20}$$

where C_0 is a constant critical transfer concentration which has an inverse value of the Perrin constant (K_p). By using units of moles per liter for C_0, R_0[Å] is equal to 7.346 $C_0^{-1/3}$.

For instance, a pair of Pt(II)-octaethylporphyrin (PtOEP) and 9,10-diphenylanthracene (DPA) in a frozen solution such as 1,1,1-trichloroethane at 77K was experimentally demonstrated as perfectly fitted data by the equation above and their Dexter radius for collisional overlap was calculated to be approximately 26.5 Å,[12] which is relatively shorter than the distance of Coulombic interactions. Meanwhile, in order to explore the kinetics of a photophysical intermolecular quenching process in the statistical mixing condition of fluidic media, the Stern-Volmer relationship[49] provides dynamic behavior of the energy transfer between molecules at high quencher concentrations by measuring of relative donor fluorescence quantum yield. The bimolecular quenching rate constant (k_q) can be obtained according to the kinetics of a collision quenching process:

$$I_0/I = \tau_0/\tau = 1 + K_{SV}C_A \quad \& \quad K_{SV} = k_q\tau_0 \tag{21}$$

where I is the emission intensity in photoluminescence, τ is the lifetime of the excited state of donor, K_{SV} is the Stern-Volmer constant and C_A is the concentration of acceptor (or quencher). The subscript '0' represents the value in the absence of acceptor molecules.

It should be noted that the energy transfer process becomes much more efficient at higher temperature because molecular diffusion is completely prevented in a pure Dexter mechanism. Therefore, the diffusion-controlled Dexter energy transfer rate[12, 50] can be described as a donor quenching through a direct collision with the acceptor with the Dexter radius in steady-state conditions:

$$k_q = 4\pi D R_0 = \frac{2k_B T R_0}{3\eta(R_{m,D} + R_{m,A})} \tag{22}$$

where D is the overall diffusion coefficient defined as the sum of the diffusion coefficient of donor and acceptor. In addition, the Stokes-Einstein relationship provides diffusion coefficients of molecules: T and η are the temperature and viscosity of the solvent respectively, and R_m is the effective molecular radius.

The modified diffusive Dexter energy transfer rate indicates that molecular diffusion plays a key role in enhancing the efficiency in bimolecular systems for delayed UC fluorescence because the diffusion lengths are orders of magnitude larger than the Dexter radius with long lived triplet states of molecules. In terms of the short-range nature of Dexter energy transfer, therefore, it is necessary to improve molecular mobility by using inert media with low viscosity and small molecular species at room temperature, rather than finding a pair of chromophores with large Dexter radii.

1.4.6 Quantum yield

TTA-based upconversion is controlled by a variety of factors including relative concentrations of chromophore along with the quadratic excitation power dependence. Therefore, the upconverted quantum yield ($\emptyset_{UC}$) is the product of the yields of all the steps involved in the process:

$$\emptyset_{UC} = \emptyset_{ISC} \text{ x } \emptyset_{TTET} \text{ x } \emptyset_{TTA} \text{ x } \emptyset_{F} \tag{23}$$

where $\emptyset_{ISC}$ is the intersystem crossing yield in the sensitizer, $\emptyset_{TTET}$ is the triplet-triplet energy transfer yield, $\emptyset_{TTA}$ is the triplet-triplet annihilation yield, and $\emptyset_F$ is the fluorescence quantum yield of the acceptor. However, it is difficult to quantify absolute quantum yields for the relevant process. In the sensitized upconverted fluorescence, thus,

quantum yield measurements were practically measured relative to a known standard in the optically diluted solution utilizing the equation below:[31]

$$\emptyset_{UC} = 2\emptyset_{std}\left(\frac{A_{std}}{A_{UC}}\right)\left(\frac{I_{UC}}{I_{std}}\right)\left(\frac{n_{UC}}{n_{std}}\right)^2 \quad (24)$$

where ϕ, A, I and n represent the quantum yield, absorbance, integrated photoluminescence intensity, and refractive index of the medium at the excitation wavelength, respectively. The subscript 'UC' and 'std' stand for the upconversion sample and standard counter under the identical excitation source. The equation is multiplied by a factor of 2 to scale the maximum quantum yield to 1 rather than 0.5, since absorption of two photons are required to produce one higher energy photon in TTA-UC processes, while the emission in standard counters is directly proportional to the number of the incident photons.

1.5 Microfluidic Encapsulation by Photoinduced Interfacial Polymerization

To date, the majority of sensitized UC studies have been carried out in deoxygenated organic solvents at room temperature. In order to fully exploit the upconversion process for potential device integration, however, it would be highly attractive if solid materials could be developed that were capable of displaying this effect. This advance would, for example, permit the utilization of wavelength-shifting films in combination with solid-state lasers, or in photovoltaics, enabling more complete harnessing of the solar spectrum. Ultimately, this is particularly valuable for making better use of the near-IR region in real devices. With the notion that chromophore diffusion must be possible to allow for the energy transfer of two triplets in low-concentration dye/polymer blends, copolymers such as poly(ethyleneoxide epichlorohydrin(EO-EP)) and polyurethane have served as examples of rubbery polymer host matrices as shown in **Figure 1.9**.[31] However, translational mobility of the chromophores in the matrix polymer was completely suppressed below the glass transition temperature and even partially suppressed at room temperature, preventing the necessary bimolecular interaction between donor and acceptor required for TTET and between two acceptor/annihilator molecules required for TTA.

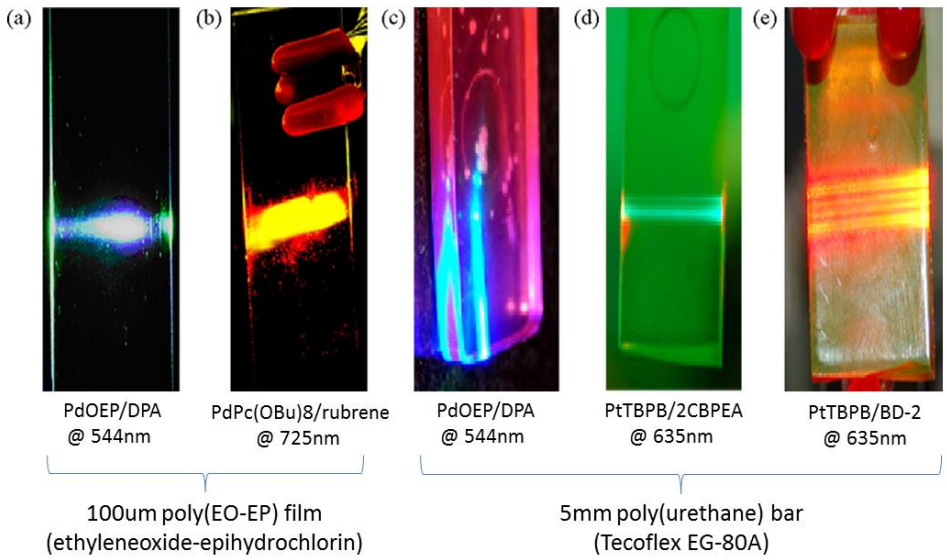

Figure 1.9. Selectively excited photon upconversion systems in rubbery polymers.[31]

These observations are qualitatively consistent with sequential bimolecular chemical steps under diffusion control as predicted by the Stokes-Einstein relationship ($D = kT/6\pi\eta R_m$) where the chromophore diffusion coefficients are directly proportional to the temperature and inversely proportional to the viscosity of the medium. Therefore, the overall upconverting efficiency was determined by these cooperative effects which promote fast diffusion and more efficient energy transfer collisions rendering improved upconversion yields. The lower observed quantum efficiency reported in the solid state at room temperature was proposed to be a result of low triplet exciton mobility and hence it was concluded that a fluidic host with an increased diffusion coefficient needs to be considered.

Overall efficiencies of triplet fusion upconversion are determined by the diffusion length of the triplet excitons: spatial overlap between the donor and acceptor wave functions is required for exchange interaction. Thus, molecular diffusivity of the

chromophores within an inert solid medium is of paramount importance for practice operation. Although rubbery polymers with low glass-transition temperature had been demonstrated to be effective at room temperature, molecular mobility is still restricted compared to common organic solvents. We had developed an alternative method to encapsulate active fluidic UC solution which allows for high translational mobility, preventing the large decrease in efficiency observed in conventional solids. Through the previous work in our group, microfluidic encapsulation was successfully demonstrated as an effective approach to provide for low-threshold, uniform sized UC microcapsules, where a polymer resin served as both a medium for TTA-based UC and a shell for protection and device integration.[51]

1.5.1 Fabrication of dual phase UC capsules from a single photocurable emulsion

Materials: For an example of the chromophore pairs, Platinum(II)-tetraphenyl Tetra-benzoporphyrin (PtTPBP, Frontier Scientific) and 9, 10-bis(phenylethynyl)anthracene (BPEA, 97 %, Sigma-Aldrich) were initially dissolved in chloroform and blended into ethoxylated trimetylolpropane (ETPTA, SR454, Sartomer) with weak sonication. Insoluble impurities were removed by filtration through a 0.2 μm syringe membrane (VWR). Chloroform was selectively removed using a rotary vacuum evaporator and a vacuum oven, and the resultant prepolymer solution was purged with nitrogen for 30 minutes. The final concentration of PtTPBP and BPEA was 0.44 mM and 5.82 mM, respectively.

Fabrication: To produce monodisperse emulsion droplets, a T-junction microfluidic channel was assembled using a metal needle and capillary glass tube. Oil

and water phases were pumped into the inner and outer capillary at specified volumetric flow rates. The prepolymer was injected into the water containing photoinitiator and surfactant. The ETPTA emulsion droplets were polymerized by subsequent UV exposure (**Figure 1.10**). Stable capsules were obtained by gently rinsing several times with deionized water to remove photoinitiator and surfactant.

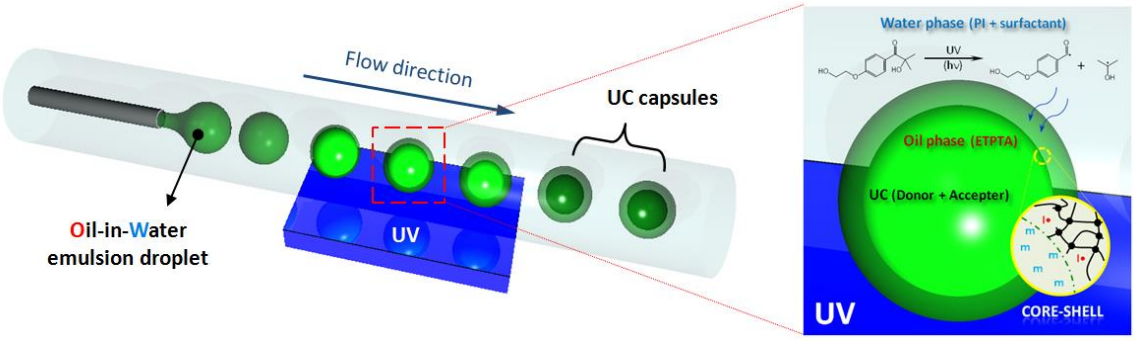

Figure 1.10. Fabrication of monodisperse UC capsules through interfacial photopolymerization.[51]

Characterization: The photoluminescence (PL) properties of the capsules were inspected using a confocal microscope (LSC 510 Vis, Zeiss) fitted with a 633 nm laser for excitation, and both 650 nm long-pass and 465-510 nm band-pass filters for detection. Absorption measurements were carried out using a 1 cm by 1 cm quartz cuvette through a UV-Vis spectrometer. For PL measurements of the assembled monolayer of capsules, 620±1.5 nm light was used as an excitation source through a spectrofluorophotometer. Also, observation of fluorescence was performed using an optical microscope.

1.5.2 Shell thickness control of UC capsules via curing time

The capsule shell thickness can be controlled via UV exposure time. Here, the range from 33 to 120 seconds under illumination of 3.7 $mWcm^{-2}$ at 365 nm was used, and the impact of shell thickness on capsule PL was investigated. **Figure 1.11** depicts confocal microscope images at the clear-cut focal plane of the capsules. Two distinctly different emission bands were observed, one associated with the core and another from the shell. The intensities of these bands are dependent upon the respective diffusivities of the chromophores and required molecular energy transfer; upon 633 nm excitation, annihilation fluorescence induced green emission emanates from the core, whereas the magenta signal derives from emission associated with phosphorescence of the sensitizer through the crosslinked shell. Increasing UV curing time leads to a thicker downconverted PL region, which indirectly indicates shell thickness. The corresponding profiles display the relative intensities of upconverted and downconverted emissions. Their onset positions coupled with the PL peaks define the interfaces between the core and shell of the capsules. If the shell layer was too thin, the capsules did not have sufficient mechanical strength and the core resin easily leaked out upon washing and drying. An overly thick shell layer reduces the volume of the core leading to a reduction in upconverted emission. With controlled UV exposure, the solid capsule shell has reversible elastic properties and no leakage of core contents was detected.[51]

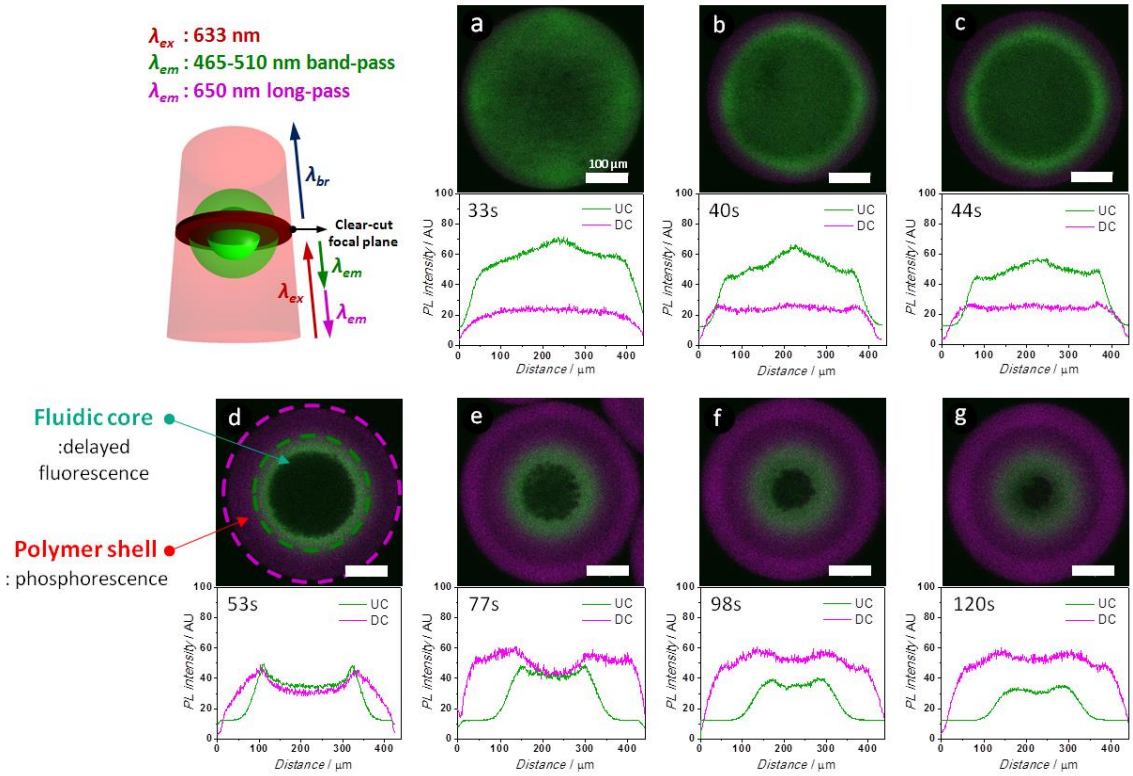

Figure 1.11. Confocal microscope images and the corresponding upconverted (UC) and downconverted (DC) PL profiles at clear-cut focal plane of capsules with variable UV curing times. All scale bars are 100 μm.[51]

1.5.3 Assembled arrays of UC capsules with different thickness and their stabilities

Since each capsule behaves as a single, isolated photon upconverting unit, it can be used as a building block for a multi-dimensional optical system. Uniformly sized capsules enable self-assembly of the structures into a hexagonal close-packed monolayer array and the relative PL yield is determined by the number of capsules per unit area. As illustrated in **Figure 1.12**a, bluish green emission from the array was generated at the region of excitation in **Figure 1.12**b. Although a portion of red excitation light was scattered at the surface of the capsules due to their spherical shape and refractive index

difference between air and ETPTA (n~1.469), a bandpass filter allowed for distinguishing upconverted emission from scattered light of the source. Fluorescence optical microscopic images also depict the dramatic emissive response of the capsules. While upconverted emission is barely discernible under conditions of no excitation (top) or filtered blue light (middle), the bottom image shows the intensely condensed emission from the capsule cores upon excitation with a conventional laser pointer. **Figure 1.12**c depicts the relevant PL intensities of monodisperse capsule arrays with different shell thicknesses. Integrated spectra of upconversion at a 510 nm peak and downconversion at 770 nm were obtained under exposure to ultralow density radiation (approximately 0.165 $mWcm^{-2}$ at 620±1.5 nm).

Meanwhile, the shield offered by encapsulation prolongs the natural lifetime of the process by retarding oxygen penetration which typically quenches the excited states in organic systems and represents a significant drawback for standard TTA-assisted upconversion processes.[14] For evaluation of capsule stability, integrated upconverted PL was measured as a function of time in ambient air, as shown in **Figure 1.12**d. Except for the first two samples receiving the shortest UV curing times (33/40 sec), most of the core-shell structured capsules appear very stable, with no apparent reduction in PL intensity over 240 hours. Thus, through appropriate control of shell thickness (with more than around 40 μm), the active core is readily protected from the ambient.

We have designed an effective approach to provide for low-threshold TTA-based UC within a structure that could be readily incorporated into a photonic device using conventional processing methodologies. The microfluidic fabrication of monodisperse core–shell microcapsules using UV-initiated free-radical inverse polymerization has been

demonstrated, where a photocurable resin served as both a medium for TTA-based UC and a shell for practical passive protection. By taking advantage of a structure composed of a liquid core and a solid shell, self-assembled capsule arrays were shown to offer outstanding optical emission under ultralow power excitation coupled with high mechanical integrity and strength. Thus, dual phase structure has significance not only for enabling promising applications in photovoltaic devices and photochromic displays, but also for providing a useful platform for photocatalytic and photosensor units.

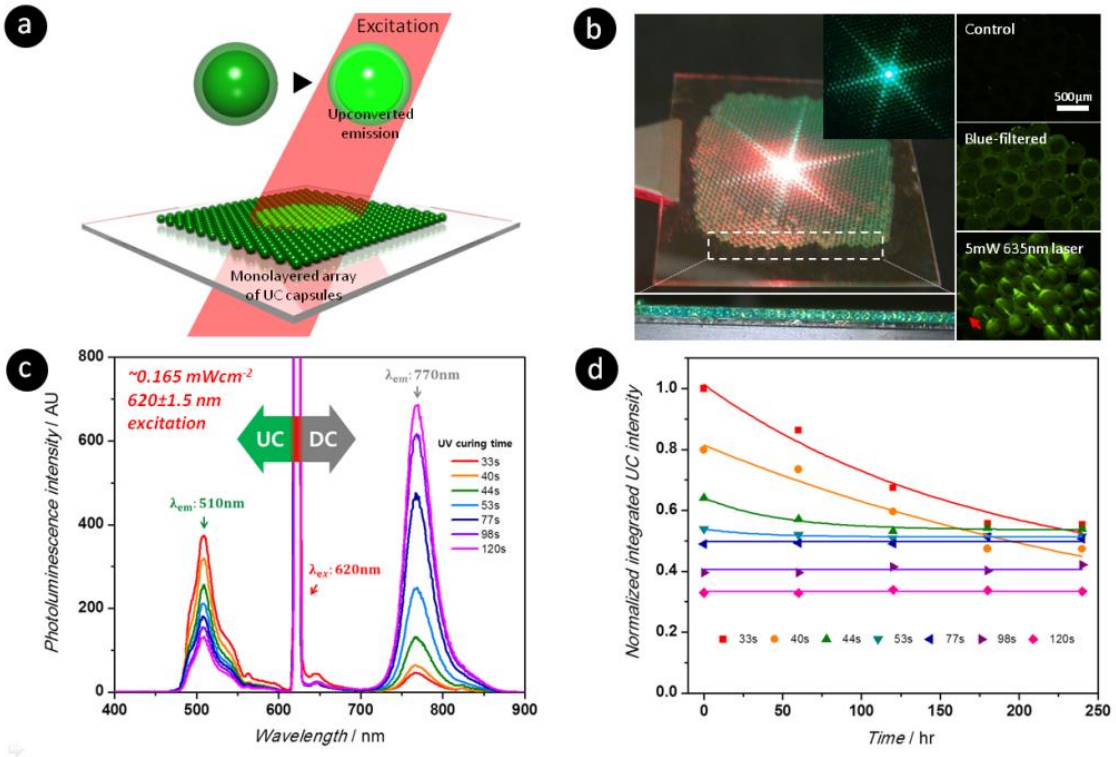

Figure 1.12. a) Upconverted emission from monolayered array of capsules, b) Optical images of the array under a laser of 633nm 5 mW; Inset shows a 515-525nm bandpass filtered emission, c) PL spectra of the arrays with variable UV curing times, and d) Normalized integrated UC intensities of the arrays as a function of time under ambient condition.[51]

CHAPTER 2. ULTRATHIN DOUBLE-SHELL CAPSULES FOR HIGH PERFORMANCE PHOTON UPCONVERSION

Ultrathin shell triple emulsion capsules fabricated via consecutively controlled dripping instability are developed to achieve highly efficient triplet-triplet annihilation (TTA)-based photon upconversion (UC). Spatial confinement of the injection capillary allows formation of a stable jet by suppressing biphasic flow instabilities, while a flow-focusing geometry induces subsequent breakup of the coaxial jet into monodisperse triple emulsion drops through abrupt enlargement of the channel diameter. The single-step multiphasic emulsification, facilitates continuous fabrication of core-shell-shell structures having controllable shell layer thickness. A thin inner aqueous layer serves to separate the hydrophobic core and outer shell, thereby providing for highly efficient encapsulation of the hydrophobic fluidic cargo containing upconversion chromophores. Chromophore molecular mobility is thus retained and high quantum yields result. The compartmentalized structure, enables use of a heavy atom containing oil that affords significantly enhanced upconversion quantum yield, and incorporation of stabilizers into the core solution improves photochemical stability. Furthermore, magnetic nanoparticles are readily incorporated into the perfluorinated photocurable monomer that serve as a transparent thin outer performance shell to impart motion control via application of a magnetic field. The results represent a significant advance in the development of solution-based TTA-UC for low threshold applications.

2.1 Introduction

The photochemical process of triplet fusion, or alternatively triplet-triplet annihilation (TTA), is a recognized low threshold upconversion (UC) strategy that produces higher energy photons than those associated with excitation.[31, 42, 52] TTA-based UC is typically achieved by long-lived triplet excited states of an organometallic sensitizer which allows the absorption of non-coherent continuous wave from low power density sources such as sunlight.[38, 53] The sensitized UC approach enables recycling of sub-bandgap photons, thereby offering opportunities to overcome efficiency limits of solar harvesting devices.[13, 16, 54-56] The anti-Stokes process is implemented by consecutive, bimolecular energy transfer steps between chromophores; two instantaneous triplet-triplet energy transfer (TTEA) couplings occur from sensitizer to acceptor molecules, with subsequent TTA between the acceptors.[57] The energy transfer processes, associated with metastable states, require direct collision or electron exchange for effective wavefunction overlap between the excited chromophore molecules.[58-60] Triplet exciton or excited molecule diffusion is of paramount importance to facilitate the required TTA-UC energy transfer sequence. Past TTA-UC studies have focused primarily on sensitizer – acceptor interactions in organic solvents; however, media that allow solid-state diffusion are required for practical implementation. Thus, research efforts to explore TTA processes in materials such as rubbery polymers[17, 61-63] and nanoscale confined particles[64-65] have expanded rapidly. Unfortunately, these solid hosts restrain the mobility of the embedded chromophores, resulting in lower quantum yield efficiencies compared to liquid phase UC. Further, oxygen permeation into the material is another prevalent problem that reduces stability/lifetime in UC processes. Metal-organic

frameworks (MOFs) have been recently used as a new solid-state medium to promote TTA-UC. The MOF provides for a high diffusion rate of triplet excitons owing to an organized structure of acceptor molecules in the crystalline structures;[66-68] however, the nanocrystals must be encapsulated in polymers to avoid local heating and bleaching, and be sealed in an inert gas. Semi-solid-state organogels that microscopically trap a liquid phase have also been reported to show upconversion performance comparable to liquid systems,[69-70] but there are limits to the gel crosslinking density and the gelation step requires high temperature processes and/or air-free conditions in a molding container.

Microfluidic encapsulation of solutions containing TTA-chromophores with a polymeric membrane represents an attractive alternative approach.[51, 71] A fluidic active capsule core supports chromophore molecular mobility and enables high quantum yield. The polymeric shell serves as both a protective barrier to retard diffusion of reactive oxygen species into the core and a container for the fluid core. The capsules can be individually deposited in any form, shape or state for a given application; for example, a packed array of capsules in the dry state behaves as an integrated light emitting film for volumetric displays,[72] whereas dispersed in the aqueous medium, the capsules act as homogeneous light sources for photocatalysis[73] or bioimaging.[23, 26, 74] Despite the promise provided by this compartmentalized core-shell structure, conventional microfluidic approaches based on single (oil-in-water) or double (oil-in-oil-in-water) emulsions produce capsule shells that are not fully isolated from the core and thus, exhibit inexorably strong phosphorescence emission due to inhibition of the energy transfer steps required for TTA-UC and resultant significantly decreased UC yield.[51, 71, 75]

2.2 Experimental Section

2.2.1 *Materials*

As stock solutions, palladium tetraphenyltetrabenzoporphyrin (PdTPBP, American Elements) and 9,10-bis(phenylethynyl) anthracene (BPEA, Sigma-Aldrich) were separately dissolved in 1-bromohexadecane oils by heating at 75 °C. Light stabilizer additives like BHT and HALS were added to the mixture of PdTPBP and BPEA solutions and blended using sonication. The final concentrations of PdTPBP and BPEA were about 0.22 mM and 2.64 mM, respectively. The innermost oil solution was stored in an amber vial at room temperature and was filtered using 0.2 μm syringe membrane (VWR) before use. The inner shell phase was composed of 90:10 v/v D.I. water and glycerol (Sigma-Aldrich) containing 4 wt% PVA (Mw 13000-23000, 87-89% hydrolyzed, Sigma-Aldrich). The outer shell phase was a monomer of perfluoropolyether-urethane dimethacrylate (Fluorolink MD700, Solvay) containing 5 wt% photoinitiator (Irgacure 2100, BASF). For magnetoresponsive capsules, iron oxide nanoparticles (hematite; α-Fe_2O_3 smaller than 50 nm, Sigma-Aldrich) were treated with oleic acid using a probe sonicator (Q700, Qsonica) and added into the monomer solution. The suspension was sonicated for 30 minutes prior to its use. The continuous phase was 6 w/w% aqueous solutions of PVA (Mw 13000-23000, 87-89% hydrolyzed, Sigma-Aldrich).

2.2.2 *Device preparation*

A coaxial microfluidic device was assembled by oppositely aligning two tapered glass cylindrical capillaries into a square capillary (AIT Glass), as shown in Figure 1a. As an injection capillary, the cylinder with 200 μm inner diameter (AIT Glass) was tapered

using a puller (P-97, Sutter Instrument) and then carefully sanded to have about a 160 μm outer orifice. After cleaning with isopropyl alcohol and treatment with an oxygen plasma (PDC-32G, Harrick Plasma), the inner surface of the capillary was selectively rendered hydrophilic by infiltrating 2-[methoxy(polyethyleneoxy)propyl] trimethoxy silane (Gelest) through untapered opening by capillary force and then incubated for 15 minutes. Whereas, the outer wall of the capillary was rendered hydrophobic by exposing it to trimethoxy(octadecyl)silane (Sigma-Aldrich) for 5 minutes. For the collection capillary, a glass cylinder with a 580 μm inner diameter (World Precision Instrument) was tapered and sanded to have about a 300 μm orifice. Both inner and outer surfaces of the capillary were treated by dipping it into the solution of 2-[methoxy(polyethyleneoxy)propyl] trimethoxy silane (Gelest) to render both surfaces hydrophilic. Using an epoxy glue (Devcon), the two injection and collection capillaries were coaxially assembled in the square capillary to have 160 μm distance between tips. Then, a second small capillary with a 170 μm outer diameter (VitroCom) was inserted into the untapered opening of the injection capillary. Finally, all inlets were sealed with hub of dispensing needles (20G, McMaster-Carr) on a slide glass. The needles were connected into each phase with syringes (Hamilton or Henkesasswolf) through polyethylene or polytetrafluoroethylene tubing (Scientific Commodities). The digital image of the capillary microfluidic device is shown in **Figure 2.1**.

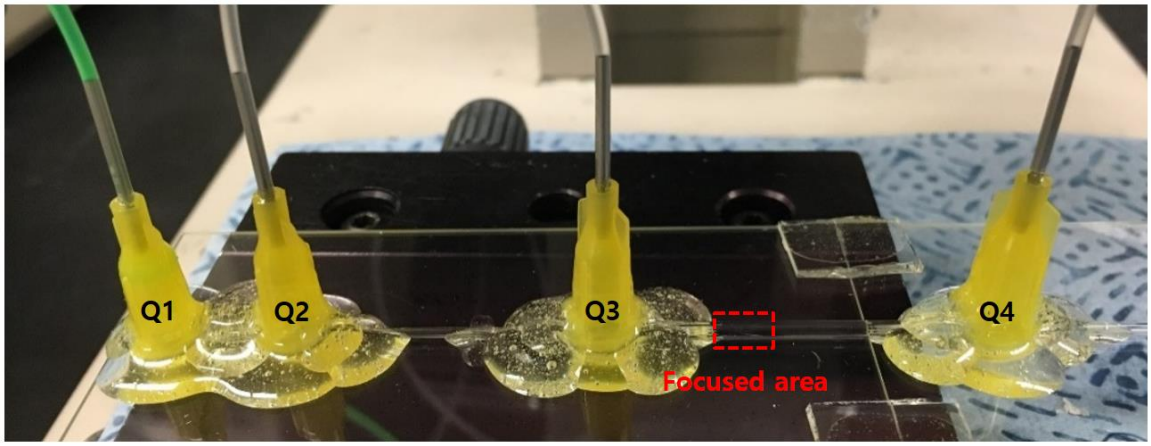

Figure 2.1. Digital image of the capillary microfluidic device.

2.2.3 *Device operation and encapsulation*

The volumetric flow rates of the four fluids were controlled using syringe pumps (Kd Scientific and Harvard Apparatus) and typically set to be 1300-2000, 100-300, 300-600 and 6000 µl hr^{-1} from innermost to continuous phase for continuous generation of triple emulsions. The formation of emulsion drops was observed using an optical microscope (Axio-observer, Carl Zeiss) equipped with a high speed camera (Phantom v9.1). During collection, each emulsion drop was continuously irradiated by spot UV curing light (OmniCure S2000, Lumen Dynamics) for one second to polymerize the outer shell phase.

2.2.4 *Characterization*

The photoluminescence properties of the microcapsules were observed using a confocal microscope (LSM 700, Zeiss) equipped with 639 nm laser for excitation and both a 640 nm long-pass and 555 nm short-pass filter for detection. Absorption and photoluminescence measurements were carried out with a 1 cm by 1 cm quartz cuvette

through a UV-Vis spectrometer (8453, Agilent) and a spectrofluorophotometer (RF-5301pc, Shimadzu), respectively. The quantum yield for TTA-UC (ϕ_{UC}) was calculated relative to methylene blue in ethanol as a standard (ϕ_{std} = 0.04)[76] using the following equation:[31]

$$\phi_{UC} = 2\,\phi_{std}(A_{std}/A_{UC})(I_{UC}/I_{std})(n_{UC}/n_{std})^2$$

where ϕ, A, I and n represent the quantum yield, absorbance, integrated photoluminescence intensity, and refractive index of the medium, respectively. The subscript 'UC' and 'std' stand for the upconversion sample and standard counter under the identical excitation source, 500 μWcm^{-2} 633 ± 1.5 nm. The refractive indices of the 1-bromohexadecane, hexadecane and ethanol were 1.461, 1.434 and 1.36, respectively. The equation is multiplied by a factor of 2 since absorption of two photons are required to produce one higher energy photon in TTA-UC process while the emission in standard counter is directly proportional to the number of the incident photons. Magnetic movement was observed using an optical microscope (BX51, Olympus).

2.3 Results and Discussion

In this work, we designed robust, triple microcapsules housing a liquid core to implement low threshold triplet-fusion-based UC. To achieve highly efficient TTA-UC, a solubilized sensitizer and emitter pair was encapsulated with a double shell comprising an ultrathin separation layer and an outer polymer shell using triple emulsions. A stable jet of oil-in-water biphasic flow is formed in a narrow capillary channel, which is then encased by a hydrophobic photocurable oil phase and simultaneously emulsified into a continuous water phase to form oil-in-water-in-oil-in-water (O/W/O/W) triple-emulsion drops in a capillary microfluidic device. This single-step emulsification allowed high loading of the UC-active materials by reducing the volume occupied by the aqueous layer and continuous production of the capsules. A brominated hydrocarbon used for the UC medium is an outstanding solvent to achieve dramatic improvement in quantum yield compared to conventional options. Furthermore, photochemical stability of the core oil phase was significantly enhanced by incorporation of light stabilizers. A perfluorinated resin used to form the polymer shell is an effective encapsulating material: the prepolymer solution can be quickly stabilized through photoinduced covalent crosslinking. Moreover, the high density of the resin complements the low density of the core oil, rendering the capsules slightly heavier than the continuous phase and easy to handle. The polymer shell was tailored further by incorporation of magnetic nanoparticles, which imparted the ability to remotely control capsule position and properties without undesired light scattering from the nanoparticles.

Since the overall efficiency of the delayed fluorescence led by TTA-UC process is significantly affected by the total amount of chromophores and photons available within a

core solution, transparent complex emulsions represent an attractive alternative approach to achieving efficient TTA-UC systems. Triple emulsions have onion-like architecture, where an intermediate layer separates the inner core and the outer shell. Thus, triple emulsions can serve as a template to make capsules composed of TTA-UC cores, with a separation layer and polymeric shell. However, typical microfluidic processes require two or more steps of emulsification at different junctions to produce triple emulsions, which in turn necessitates precisely controlled operations to optimize channel volume and flow rate. Furthermore, the process window for synchronized one-by-one encapsulation is narrow, providing limited control over the cargo volume.[77] Therefore, there is an unfulfilled need for a microfluidic emulsification technique to achieve highly efficient encapsulation and retention of TTA-UC cores. Recent advances in microfluidics have provided for single-step emulsification of multiple phases by employing a flow-focusing geometry, which enables precise control of volumes and properties of each compartment/layer in multiple emulsions.[78-79]

2.3.1 Fabrication of monodisperse ultrathin double-shell capsules

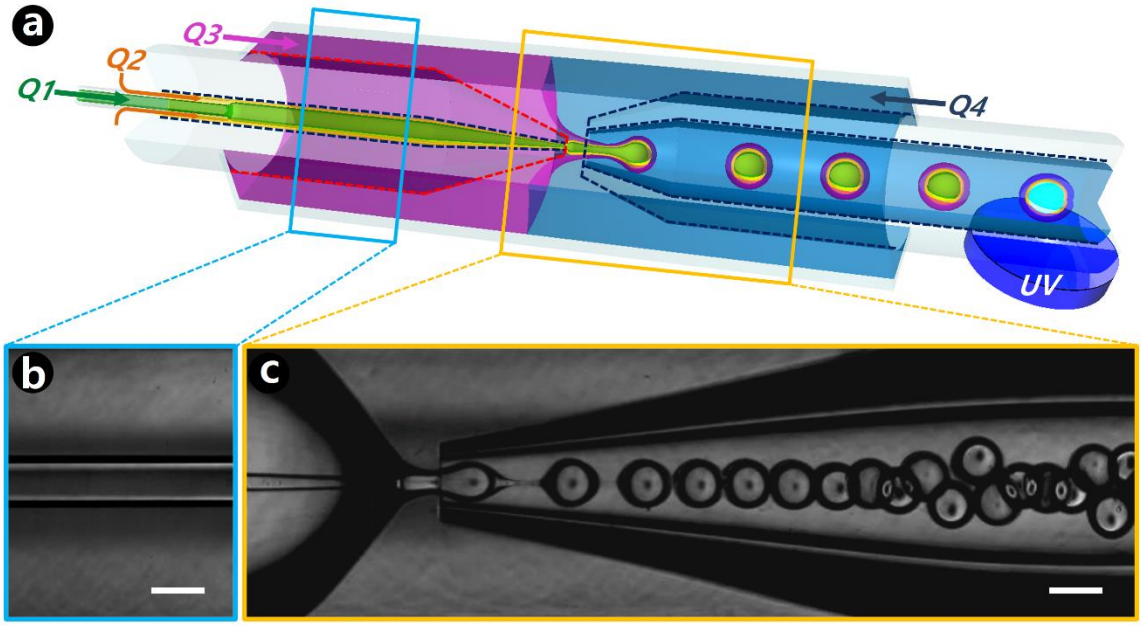

Figure 2.2. a) Schematic illustration of a glass capillary microfluidic device used for the production of the oil-in-water-in-oil-in-water triple-emulsion drops consisting of an innermost UC hydrocarbon core oil (Q1), an aqueous inner shell with 4 wt% PVA and 10 vol% glycerol (Q2), and an outer shell oil of photocurable monomer (Q3), and a continuous aqueous phase with 6% PVA (Q4). The blue dotted lines indicate hydrophilic-rendered surface, while the red dotted lines show hydrophobic-rendered surface. b, c) High speed optical microscopy images showing formation of a biphasic jet flow confined in an injection capillary and continuous generation of triple emulsion drops with ultrathin shells in a dripping mode. All scale bars represent 200 µm.

We used a glass capillary microfluidic device to encapsulate the brominated hydrocarbon oil, which served as an efficient, inert medium for triplet-fusion-based photon upconversion. The device consists of two different tapered cylindrical capillaries,

one for injection and the other for collection, aligned by oppositely inserting them within a square glass tube that has an inner cross sectional area (1.05 x 1.05 mm^2) slightly larger than that of the cylindrical ones (1.00 mm outer diameter), as shown schematically in **Figure 2.2**a. To precisely control wettability and fluid behavior in the injection capillary, one cylindrical capillary (inner diameter of 200 μm) was tapered to have a 160 μm orifice diameter, and was treated to have hydrophilic inner and hydrophobic outer walls. A second small capillary (outer diameter of 170 μm) was inserted into the untapered opening of the injection capillary to enable simultaneous pumping of two immiscible fluids, namely, the brominated hydrocarbon and aqueous phases. The collection capillary, which is also cylindrical and has an inner diameter of 580 μm, was tapered to have a 300 μm orifice diameter and both walls were rendered hydrophilic to decrease the propensity of the polymer precursor to wet the surface.

A UC oil solution of the chromophores embedded in the brominated hydrocarbon was injected through the small cylindrical capillary to form the innermost phase. A 4 wt% aqueous PVA solution containing 10 vol% glycerol was then injected through the untapered opening of the injection capillary; the concentration of solutes was chosen such that the viscosity difference between these two liquids would be small to reduce the downstream propagation of flow instabilities. To provide steady, axisymmetric and laminar flow, the Reynolds number of the inner fluid was less than 1. Coaxial flow of the two immiscible fluids leads to formation of a jet that subsequently breaks into a stream of plug-like drops, which results from surface-tension driven instabilities. Owing to the wetting affinity, the flowing aqueous PVA solution behaved like a lubricant along the hydrophilic inner wall of the injection capillary, while the UC oil solution formed the

core emulsion flow without physically contacting the wall. In a given confined geometry, the behavior of this core-sheath flow is affected by flow rates. Additionally, it is possible to suppress the hydrodynamic instability of the inner fluid in a two-phase flow through geometric confinement.[80-81] By reducing the channel cross-section, we were able to produce a stable jet over a long distance. With a 200 μm diameter injection capillary, we observed formation of a 3 cm long oil jet in the aqueous PVA solution, as shown in the **Figure 2.2**b. The confinement with controlled affinity near the tip of the injection capillary minimized distortion of the fluid interface, resulting in stable formation of a thin PVA aqueous phase layer. A photocurable solution of perfluoropolyether (PFPE)-urethane with dimethacrylate functional groups, which wets the hydrophobic outer wall of the injection capillary, was injected through the interstice between the injection and square capillaries. Another 6 wt% PVA aqueous solution was injected as a countercurrent continuous phase through the other side of the interstice between the collection and the square capillaries. The jet of oil-in-water flow in the injection capillary coflows with the surrounding photocurable oil precursor, which was emulsified by shearing of the continuous water solution at the end of the tip. The pressure-driven flow then broke up into monodisperse triple emulsion drops in the focused area as shown in the high speed image of **Figure 2.2**c. As a result, the triple emulsions are produced in the so called "dripping" mode;[82] in this case, the abrupt increase in channel dimensions slows down the fluids enabling Rayleigh-Plateau breakup to happen right at the entrance of the collection capillary.

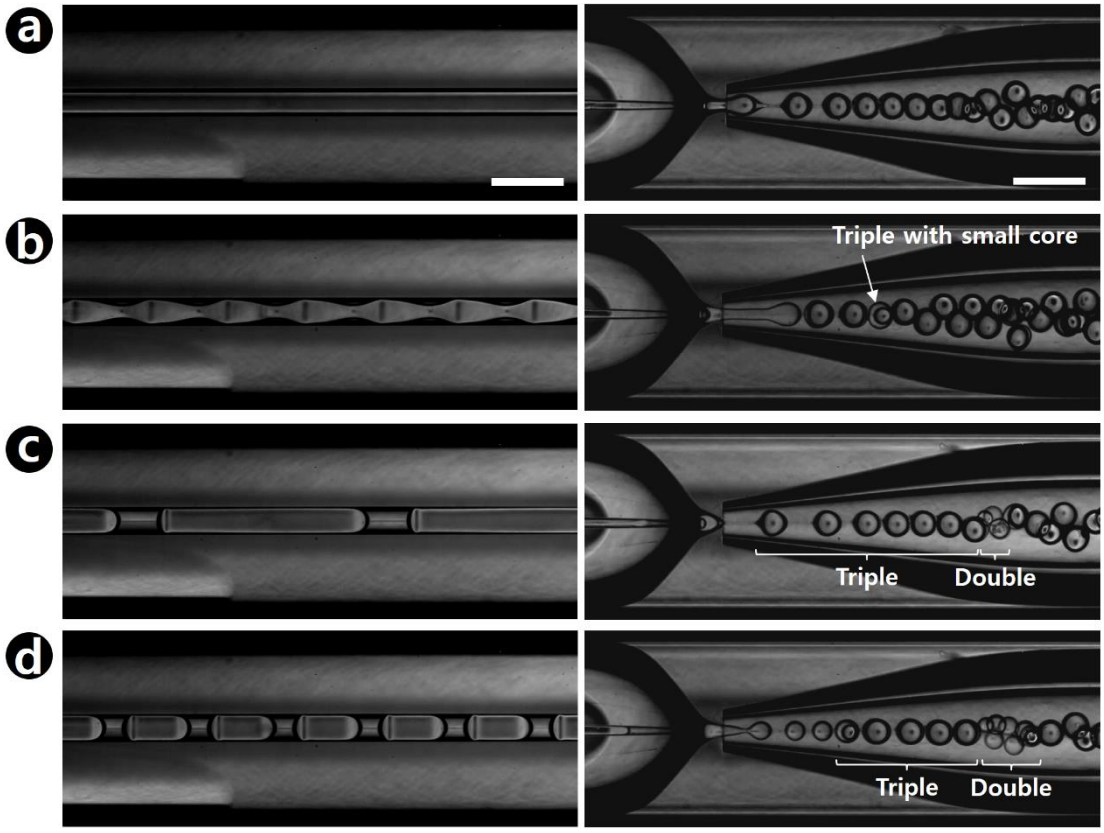

Figure 2.3. Optical microscopy images showing biphasic flow behavior confined in an injection capillary (left column) and dripping mode pattern of triple emulsion generation at the focused region (right column) as a function of Q1 which ranges from a) 2000 to b) 1500, c) 1000 and d) 500 µl hr^{-1}, where Q2, Q3 and Q4 are maintained at 300, 600 and 6000 µl hr^{-1}, respectively. All scale bars are 500 µm.

The flow rates of the innermost (Q1), inner (Q2) and outer shells (Q3), and the continuous (Q4) phases each influence the flow patterns in the injection capillary and the triple emulsion that is generated. As shown in the left image of **Figure 2.3**, a stable oil jet forms in the capillary for sufficiently large Q1 at a given Q2. For high Q1, the jet was emulsified in dripping mode near the orifice tip of the collection capillary, and triple emulsion drops were continuously generated, as shown in the right image of **Figure 2.3**a.

In contrast, for relatively low Q1, the jet became unstable and exhibited fluctuations of the interface leading to formation of double and triple emulsions with small cores, as shown in the **Figure 2.3**b. A further reduction of Q1 afforded plug-like oil drops in the injection capillary, which resulted in the formation of a discontinuous flow of double emulsion drops without the UC core, or triple emulsion drops including small volumes of UC core as defects, as shown in **Figure 2.3**c-d. Because the density of 1-bromohexadecane is slightly lower than that of water (0.999), the average density of the double emulsion drops without a UC oil core is similar to that of the triple emulsion drops. Thus, removal of the defects from the mixture is not easily accomplished by the density difference, which is a useful but necessary step in the case of plug-type biphasic injection.[79] To avoid laborious post-separation processing, the continuous generation mode is preferred over the discontinuous mode. To polymerize the outer shell resin, the triple emulsion drops were irradiated by focused ultraviolet light irradiation for one second. The capsules were then collected in a glass petri dish containing 6 wt% PVA solution.

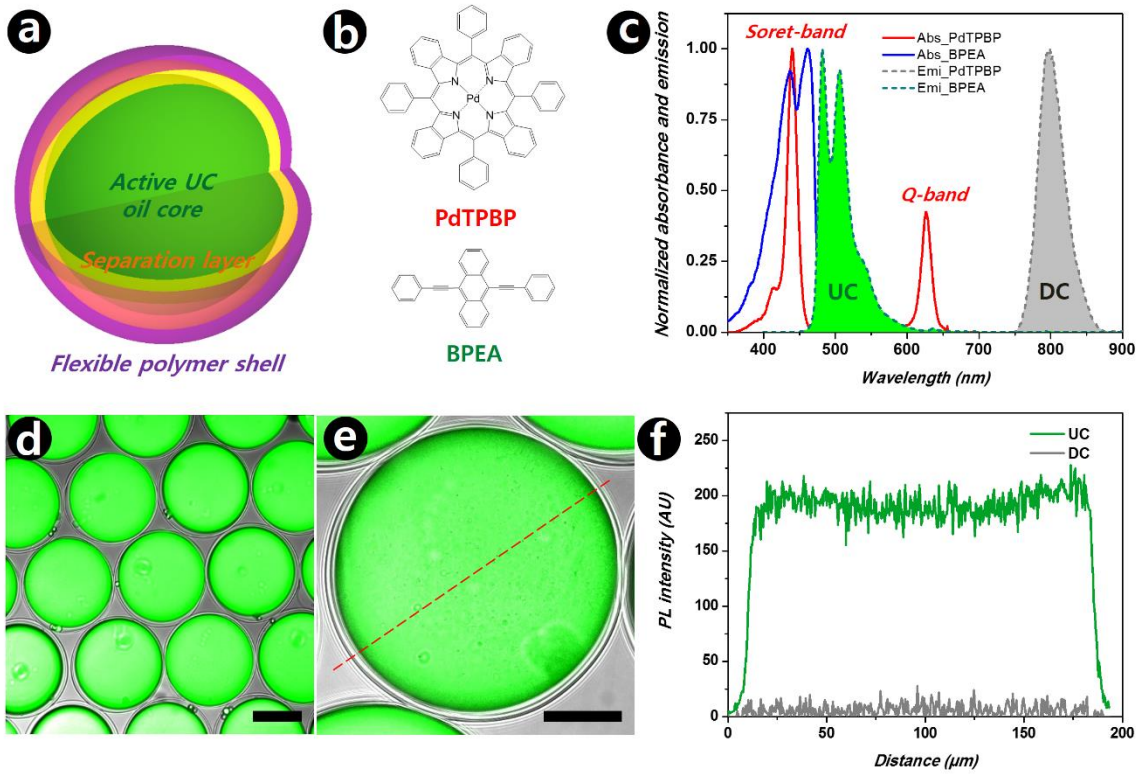

Figure 2.4. a) Schematic of UC capsule with onion-like topology; UC-active oil is encapsulated by double shells of aqueous separation layer and flexible polymer shell. b) Molecular structures of a representative red-to-cyan upconversion pair of sensitizer (PdTPBP) and emitter (BPEA). c) Normalized absorbance and photoluminescence spectra of the sensitizer and emitter dissolved in 1-bromohexadecane. Green shading area indicates upconversion (UC) emission while gray shading area exhibits downconversion (DC). d) Confocal microscopy image of hexagonally packed array of capsules. Scale bar represents 100 μm. e) Magnified confocal microscopy image of a single capsule. Scale bar represents 50 μm. f) Photoluminescence profiles cut by the red dotted line in e)

As shown in the scheme presented in **Figure 2.4**a, the resultant microcapsules were composed of an active UC oil core, an inner separation shell layer, and an outer

polymer shell. As a representative UC pair, palladium tetraphenyltetrabenzoporphyrin (PdTPBP) and 9,10-bis(phenylethynyl) anthracene (BPEA) were used as the sensitizer and emitter, respectively,[31] to demonstrate red-to-cyan upconversion in the microcapsules (**Figure 2.4**b). As shown in **Figure 2.4**c, PdTPBP exhibits Soret- and Q-bands at about 440 and 630 nm, respectively, where the latter band was used for selected excitation. Upon irradiation with red light, phosphorescence (gray area) was observed from decay of the triplet excited state of the sensitizer, while delayed fluorescence (green area) was detected by a series of triplet-triplet energy transfer and annihilation steps.

In continuous mode, the shell layer thicknesses are determined by mass balance. Control of the flow rate in Q1 at fixed Q2 allows generation of an ultrathin inner separation layer. The ultrathin PVA aqueous layer in the triple emulsion drops separates the innermost TTA-UC core oil from the photocurable oil phase, enabling encapsulation of high volumes of the hydrophobic core. Confocal microscopy images presented in **Figure 2.4**d-e show monodisperse microcapsules with an ultrathin layer separating the TTA-UC core and polymeric flexible PFPE-urethane shell. Also, the controlled wetting and high viscosity of the hydrophobic prepolymer solution enabled formation of a thin layer at a relatively low flow rate. Because the thin shell layers are not discernable microscopically, the thicknesses of inner (2-4 μm) and outer shells (7-10 μm) produced at the given flow rates, were calculated according to the mass balance and radius of the drop. As shown in the emission profiles of **Figure 2.4**f selected from **Figure 2.4**e (red dotted line), strong intense upconversion emission appears only in the core region; no phosphorescence was observed. Note that phosphorescent emission is undesired, but is typically produced in viscous solutions and non-fluidic media such as cured polymers.

The triple emulsion microcapsules occasionally contained satellite triple drops in the polymer shell; at high flow rates, a few small emulsions were produced from the long neck that forms during the breakup process and then merged into the shell of neighboring large emulsions (**Figure 2.5**a). Owing to the surrounding water layer, however, the satellites also exhibit intense emission with higher frequency photons than the excitation. The presence of glycerol in the aqueous PVA solution enabled retention of the hexagonal array of microcapsules after drying because of its non-volatile nature. Retention of glycerol in the layer supported the triple emulsion structure (**Figure 2.5**b).

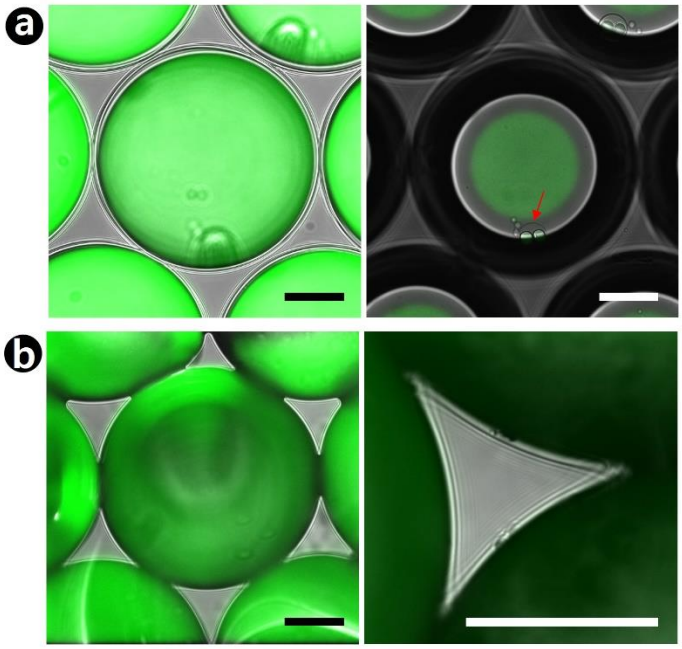

Figure 2.5. a) Confocal microscopy images of microcapsules containing satellite triple drops in the shell taken at two different positions of focal plane; Clear-cut focal plane (left) and a bottom slide from Z-stack (right). b) Confocal microscopy images of microcapsules after water evaporation of inner separation layer at room temperature. All scale bars represent 50 µm.

2.3.2 External heavy atom effect on quantum yield of TTA-UC

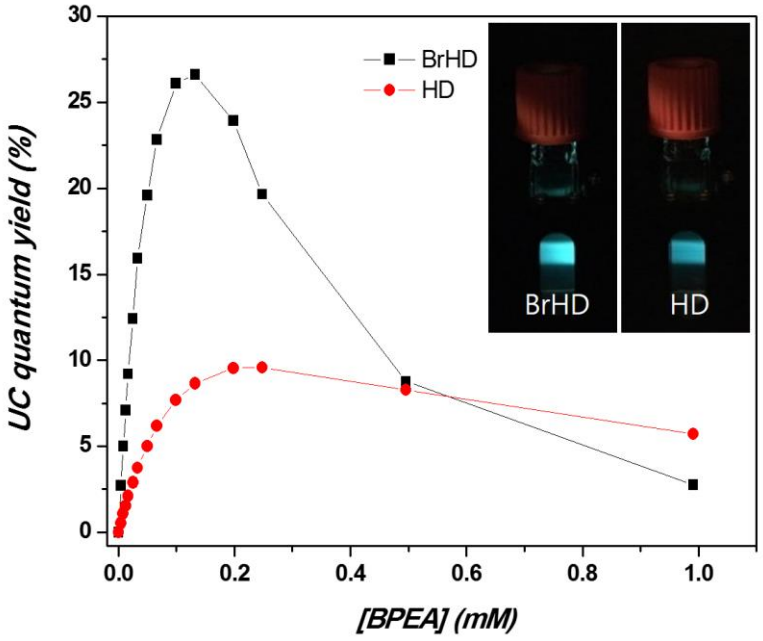

Figure 2.6. Relative upconverted fluorescence quantum yield of 1-bromohexadecane (BrHD) and hexadecane (HD) as a function of BPEA concentration at a fixed PdTPBP (~8.2 µM) under the selected excitation (500 µWcm^{-2} 633 ± 1.5 nm).

The core solution phase was 1-bromohexadecane. Among hydrocarbon oils, hexadecane was previously used as a representative medium for TTA-UC because of its relatively low viscosity (4.29 mm^{2}s^{-1}, Sigma-Aldrich), transparency and non-volatile nature. Despite its analogy to the hydrophobic carbon backbone of anthracene-based chromophores, hexadecane suffers from limited dye solubility. While adding polyisobutylene (PIB; MW~1350 Da, Polyscience) increases the solubility of dyes in hexadecane or mineral oil,[71, 75] the resultant mixtures have lower bimolecular diffusional mobility due to the honey-like, highly viscous PIB. The brominated hydrocarbon,1-bromohexadecane, resembles the parent alkane; it is colorless, hydrophobic and has

relatively low viscosity, but exhibits better solvation capacity for upconversion dyes because of the increased strength of the intermolecular forces or the polarity derived from the strongly electronegative halogen atom. More importantly, incorporation of heavy atoms into the solvent increases spin-orbital coupling of the excited singlet and triplet states, resulting in enhancement of intersystem crossing and increased lifetime of phosphorescent decay.[83-84] The relative quantum yield of the upconversion fluorescence for the PdTPBP - BPEA pair is shown as a function of BPEA concentration in **Figure 2.6**. At a fixed sensitizer concentration (~8.2 μM), the external heavy atom effect combined with higher solubility lead to about a three-fold enhancement (blue shading area, maximum yield ~26.6 %) in upconversion quantum yield for 1-bromohexadecane vs. hexadecane based UC oils under low-power density (633 ± 1.5 nm, 0.5 $mWcm^{-2}$) illumination. In the case of 1-bromohexadecane, the quantum yield dramatically decreased after reaching the saturation point, which indirectly indicates its better solvation characteristics. The upconversion intensity with two distinctive peaks (blue and green arrows) increased gradually until the solution became saturated. As BPEA concentration increased further, the intensity of the 0-0 transition peak (blue arrow) from the lowest vibration states decreased rapidly due to photon reabsorption (**Figure 2.7**).

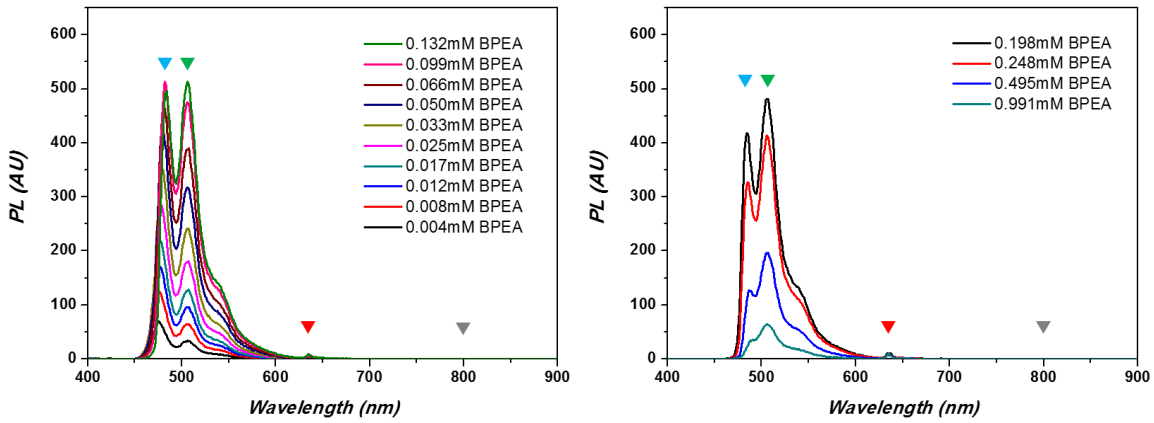

Figure 2.7. Photoluminescence spectra of 1-bromohexadecane UC solution as increase in concentration of BPEA with ~8.2 µM PdTPBP under the selected excitation (500 µWcm^{-2} 633 ± 1.5 nm). Blue and green arrows indicate two peaks of the upconversion emission. Also, red and gray arrows show the scattered light of excitation and phosphorescence, respectively.

2.3.3 Light stabilizer effect on stability of TTA-UC against photo-oxidation

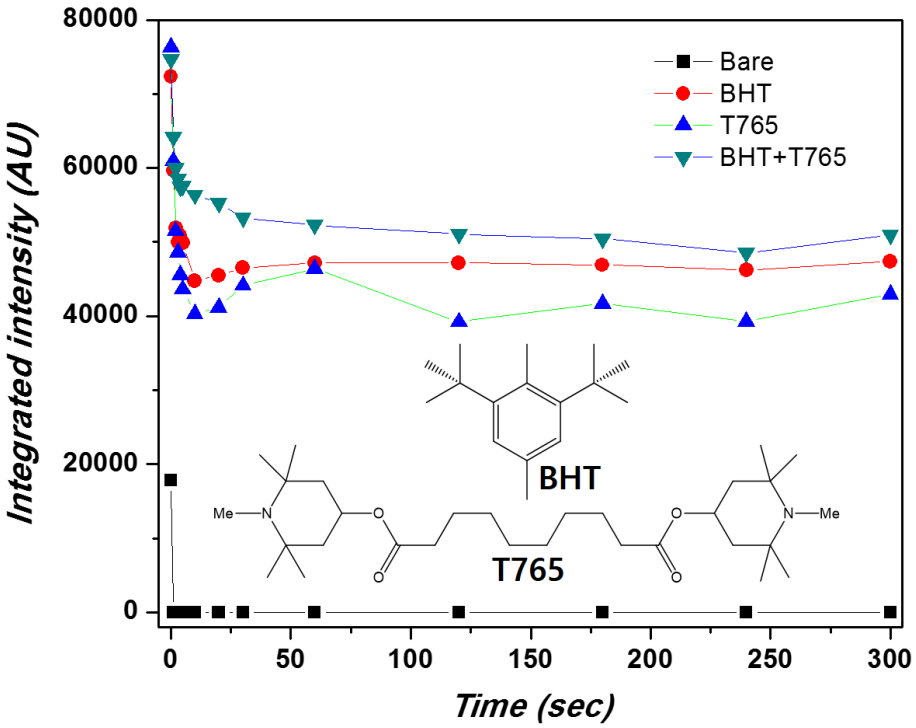

Figure 2.8. Effect of light stabilizers on TTA-UC system in ambient condition; integrated photoluminescence of upconverted emission intensity as a function of exposure time under a 5 mW 633 nm laser. Inset shows molecular structures of the butylated hydroxytoluene (BHT) and Tinuvin 765 (T765).

In the presence of oxygen, the photosensitizer in the TTA-UC system absorbs electromagnetic radiation to become excited, but readily transfers that energy to molecular oxygen without photon emission or exciton transfer. To ensure an anaerobic environment, we employed stabilizer additives, namely, butylated hydroxytoluene (BHT, Sigma-Aldrich) and Tinuvin 765 (T765, BASF). These additives are used as a lipophilic antioxidant and a hindered amine light stabilizer, respectively, either directly or in combination to prevent dynamic quenching by molecular oxygen dissolved in the solution. By trapping reactive oxygen species such as singlet oxygen, the dominant chromophore excited state quenching reaction can be suppressed, facilitating diffusional energy transfer required for the TTA-UC process. In the absence of deoxygenation steps such as nitrogen purging and vacuum degassing used for common organic solvent- or polymer-based TTA-UC, the simply prepared oil solution exhibited much higher and longer photochemical performance against oxidation under ambient room conditions. BHT acts as a terminating agent that prevents a process whereby unsaturated organic compounds are attacked by atmospheric oxygen. **Figure 2.8** shows the dramatic improvement of upconversion intensity obtained by adding 5 wt% BHT to 1-bromohexadecane system. While the pristine solution exhibited very weak cyan emission along with red excitation scattering, the solution containing BHT displayed long lasting upconversion. Tinuvin 765 acts as a weak base to scavenge reactive oxygen radicals so it

presents strong delayed fluorescence upon photon absorption but quickly sacrifices itself. The combination of 5 wt% BHT and 2 wt% T765 significantly delayed or inhibited oxidation damage of the upconversion process (see also **Figure 2.9**). Upon irradiation, the emission intensity for all samples decreased in the first few seconds, most likely because of oxygen molecules present in the medium. Initially, most of the dissolved reactive oxygen species in the solution were trapped or scavenged by the added stabilizers leading to higher emission intensity. Upon excitation, while the stabilizers inhibited oxidation of the UC system, ambient oxygen could still quickly diffuse into the solution. Once the rate of deactivation and diffusion of oxygen reached an equilibrium, UC emission stabilized.

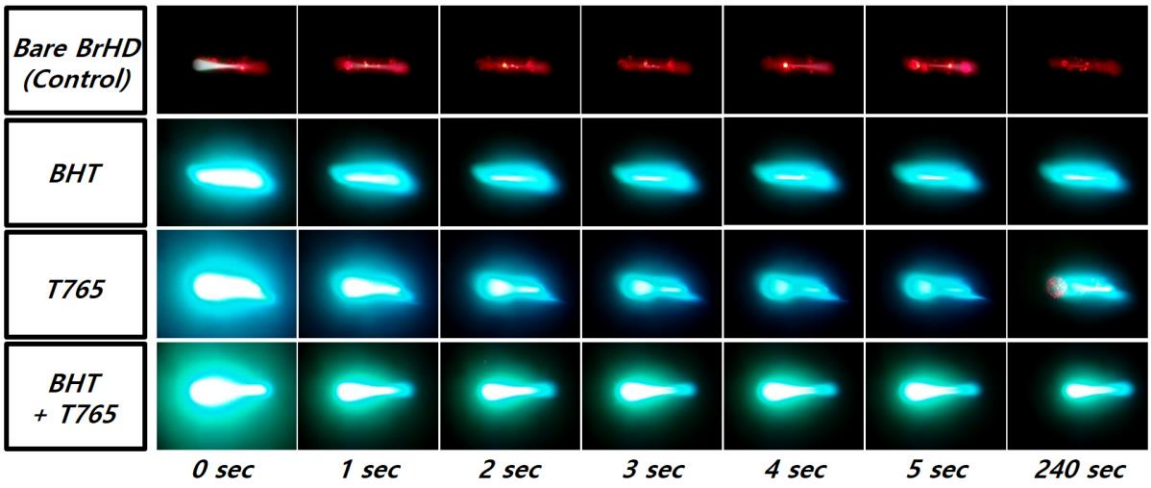

Figure 2.9. Optical microscopy still images of light stabilizers-assisted photoluminescence in TTA-UC system as a function of the exposure time under a 5 mW 633 nm laser pointer.

2.3.4 Magenetoresponsive microcapsules

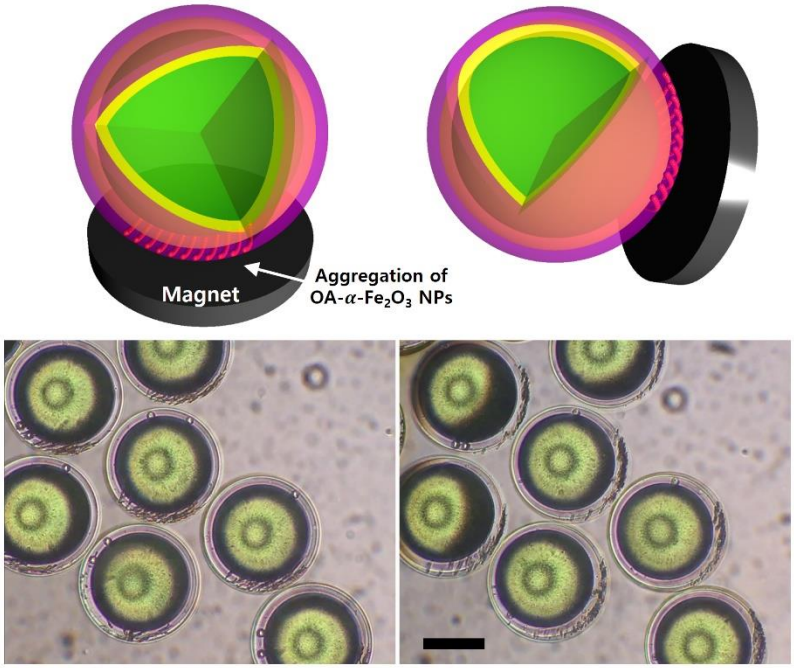

Figure 2.10. Schematic illustration of the remote-controllable motion and corresponding optical microscopy images of magnetoresponsive triple emulsion microcapsules with the polymer outer shell including aggregation of aligned oleic acid-capped iron oxide nanoparticles under external magnetic fields; from bottom (left image) and right (right image).

Further, through incorporation of magnetic nanoparticles into the polymer shell, we demonstrated the ability to functionalize the microcapsules. By using a monomer solution containing iron oxide nanoparticles for the outer shell phase, magnetoresponsive capsules were achieved. To induce alignment of magnetic moments of the hematite nanoparticles in the shell, an external magnetic field was applied to the capsules prior to photopolymerization, resulting in a net magnetic moment on the microcapsules. Due to the weak ferromagnetic nature of the nanoparticles at room temperature, application of a

magnetic field to the suspension induced interparticle dipole-dipole attraction and migration of the nanoparticles within the monomer solution surrounding each triple emulsion drop through magnetophoretic assembly. The hydrophobic oleic acid capped iron oxide nanoparticles remain inside the shell and thus, magnetic field-induced linear aggregation of the nanoparticles positioned the particles to one side, which minimized unwanted light scattering that would lower excitation intensity. The motion of the microcapsules decorated with the magnetic microfilaments could be controlled by application of an external magnet. As shown in **Figure 2.10**, remotely controlled movement of microcapsules was observed under the microscope.

2.4 Conclusion

We successfully designed a single-step microfluidic emulsification approach to produce monodisperse triple emulsion drops with an ultrathin inner separation layer for triplet-fusion-based photon upconversion. By controlling flow rates and surface affinity with geometric confinement, this process enables continuous generation of triple emulsion drops with high encapsulation efficiency, unaccompanied by defective drops. In addition, we polymerized the photocurable resin phase of the emulsion drops to form stable microcapsules containing a hydrocarbon oil which serves as an inert medium for TTA-based upconversion. The core oil can be modified to achieve significant improvement of upconversion emission yield by simply introducing the external heavy atom effect. Incorporation of light stabilizers into the solvent afforded remarkable enhancement of photochemical stability. It is noteworthy that our microcapsules exhibit strong TTA-UC intensity in both wet and dried states. Furthermore, functionalization of the thin shells with magnetic particles enables retraction and manipulation of the microcapsules in an aqueous phase environment. The latter presents a significant advantage for applications such as water treatment and photocatalysis, where aqueous media are prevalent.

CHAPTER 3. AMPLIFIED PHOTON UPCONVERSION BY PHOTONIC SHELL OF CHOLESTERIC LIQUID CRYSTALS

As an effective platform to exploit triplet-triplet annihilation-based photon upconversion (TTA-UC), microcapsules composed of a fluidic UC core and photonic shell are microfluidically prepared using a triple emulsion as the template. The photonic shell consists of cholesteric liquid crystals (CLCs) with a periodic helical structure, exhibiting a photonic bandgap (**Figure 3.1**). Combined with planar anchoring at the boundaries, the shell serves as a resonance cavity mirror for TTA-UC emission and enables spectral tuning of the UC under low power density excitation. Moreover, the CLC shell can be stabilized by introducing and polymerizing a reactive mesogen in the LC host. Due to spherical symmetry of the microcapsules, spontaneous emission of the delayed fluorescence is omnidirectionally amplified at the edge of the stop band. The present work demonstrates a wide range of opportunities provided by TTA-UC systems for the future design of low threshold photonic devices.

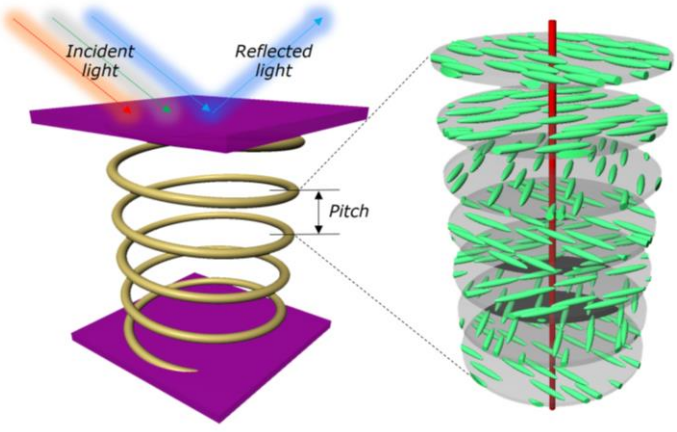

Figure 3.1. A helical structure of cholesteric liquid crystals with a band gap

3.1 Introduction

Photon upconverion (UC), an anti-Stokes process to convert two or more low energy photons into one high energy photon, is readily achieved by triplet fusion or triplet-triplet annihilation (TTA), involving intermolecular energy transfer between triplet metastable states.[31] In TTA-based UC systems, an organometallic porphyrin complex and aromatic hydrocarbon are typically used as a sensitizer and emitter, respectively.[52] Compared to conventional UC approaches such as two-photon absorption and second-harmonic generation, the triplet sensitizer enables utilization of non-coherent, low intensity continuous excitation, such as sunlight, as the pumping source; this has driven an expanding interest in UC research associated with solar energy harvesting applications.[16, 20, 54, 85] The long-lived sensitizer triplet states facilitate a series of triplet exciton diffusion steps through electron exchange; triplet-triplet energy transfer between sensitizer and emitter, and consecutive TTA between emitters. The effective exchange, which takes place by collisional spatial overlap among triplet states of chromophores, leads to generation of singlet excited state emitter molecules. Subsequently, emission of higher energy photons than those of the excitation source are produced. This phenomenon is typically referred to as "delayed fluorescence".[36] In case of imperfect exchange conditions such as slow diffusion rates, phosphorescence that arises from relaxation of sensitizer triplet excited states prevails.

The energy transfer sequence required for efficient TTA-UC, necessitates molecular mobility. Thus, a low viscosity liquid phase system is preferred, and as a result, practical implementation of TTA-UC has been limited. Recently, however, the development of microfluidic approaches, which enable the fabrication of double, triple

and even higher order emulsions with complicated interfaces and high uniformity,[78, 82] allows for encapsulation of fluidic media containing UC chromophores.[51, 71] The liquid phase core supports diffusive collision for highly efficient TTA-UC, while the solid phase shell provides mechanical integrity and protection from external threats such as singlet oxygen quenching. Notably, triple emulsions with an intermediate separation phase were recently demonstrated as an advanced core-shell template to inhibit undesired phosphorescence by avoiding cross-contamination between the active core and protective shell.

To date, encapsulation techniques, including the microfluidic approaches, have primarily focused on retaining maximum molecular mobility in UC core solutions. Therefore, photochemical efficiency is restricted to that of the base bulk mixture, which in turn, leads to limitations in the choice of constituents and their subsequent applications. Therefore, TTA-UC encapsulation methods that simultaneously achieve controlled emission intensity, coupled with controlled directionality are in great demand and remain as an unfulfilled objective.

The helical structures of cholesteric liquid crystals (CLCs) have a periodic modulation of the refractive index, which provides a photonic stop band.[86] CLCs exhibit structural colors from selective reflection at the stop band, whose wavelength is determined by their chiral pitch and the effective refractive index. Because the periodicity of their helix can be dynamically modulated with external stimuli, CLCs have been intensively studied for various photonic applications.[87-92] Through incorporation of CLCs into light emitting systems such as fluorescent dyes, an optical resonant cavity can be created, providing for precise manipulation of light propagation.[93-96]

3.2 Experimental Section

3.2.1 *Materials*

1-bromohexadecane (Sigma-Aldrich) with 4 wt% butylated hydroxytoluene (Sigm-Aldrich) and Tinuvin 765 (BASF) was used as a core oil phase. Palladium tetraphenyltetrabenzoporphyrin (PdTPBP, American Elements) and 9,10-bis(phenylethynyl) anthracene (BPEA, Sigma-Aldrich) were dissolved in the solution to be 0.176 mM and 2.64 mM, respectively. The inner shell and continuous phases were composed of 95:5 v/v D.I. water and glycerol (Sigma-Aldrich) containing 6 wt% PVA (Mw 13000-23000, 87-89% hydrolyzed, Sigma-Aldrich). The out shell phase was prepared by mixing a base CLC mixture (MLC-2149, Merck) and 20 wt% of reactive mesogen 1,4-bis-[4-(3-acryloyloxypropyloxy)benzoyloxy]-2-methylbenzene (RM-257, Merck) with 4 wt% of photoinitiator (Irgacure 2100, BASF) dissolved in dichloromethane. The solution was homogeneously mixed by ultrasonication and heated to 50-70 °C for overnight to fully evaporate the solvent.

3.2.2 *Device preparation and operation*

A microfluidic co-flow/flow-focusing device was designed to have two tapered glass cylindrical capillaries with different inner diameter (ID) in a square tube (AIT Glass). For injection, a capillary with 200 μm ID (AIT Glass) was tapered and sanded to have a 160 μm orifice. The inner surface of the capillary was rendered hydrophilic by infiltrating 2-[methoxy(polyehtyleneoxy)propyl] trimethoxy silane (Gelest). After incubation for 10 minutes, the outer surface of the capillary was exposed to 11-bromoundecyltrichlorosilane (Gelest) for 1 minute to render it hydrophobic. For

collection, another capillary with 580 μm ID (World Precision Instrument) was tapered and sanded to have a 300 μm orifice, then treated by dipping it into the hydrophilic agent. The two capillaries were inserted into the square tube in opposite direction and aligned to have 160 μm gap between tips. An additional capillary with a 170 μm outer diameter (VitroCom) was inserted into the injection capillary. Each fluid phase is injected through separate syringe pumps (Kd Scientific). For continuous production of triple emulsion drops, typical flow rates were set to be 1300, 100, 200 and 6000 μl hr^{-1} from innermost to continuous phase.

3.2.3 *Characterization*

The CLC helical structure of microcapsules was observed with a polarized optical microscope (BX51, Olympus) for both reflection and transmission modes. Absorption and photoluminescence measurements were carried out using UV-Vis spectrometer (8453, Agilent) and spectrofluorophotometer (RF-5301pc, Shimadzu), respectively. Reflectance and photoluminescence spectra of the microcapsules were measured by a spectrophotometer (QDI 202, Craic) mounted onto a fluorescent optical microscope (MD4000 M, Leica) with the customized filter cube (Semrock).

3.3 Results and Discussion

Here, we report the fabrication of triple emulsion capsules for enhanced TTA-based UC via use of a planar aligned CLC shell layer as an interference cavity mirror. To the best of our knowledge, this is the first demonstration of a fluidic TTA-UC capsule system integrated with an external photonic architecture. Using a microfluidic device, we present controlled formation of concentric triple emulsion drops that consist of an innermost UC oil core, an inner aqueous shell, and a photocurable CLC outer oil shell, all in a continuous water phase. The aqueous shell serves as both a physical barrier to prevent mixing between the core and the CLC shell and an internal alignment layer to render the CLC molecules tangentially anchored at the interface,[97] resulting in radial orientation of the helicoidal axes inside the shell.[95] As a result, the spherical confinement of the CLC phase corresponds to an isotropic photonic configuration.[95, 98-99] Photonic stop band of the helical CLCs in the shell allows the exploitation of the full potential of the diffusion-limited UC core; either the output intensity or the direction of the anti-Stokes emission can be tailored by positional control of the irradiated area.

3.3.1 Fabrication of triple emulsion TTA-UC capsules with CLC polymeric shells

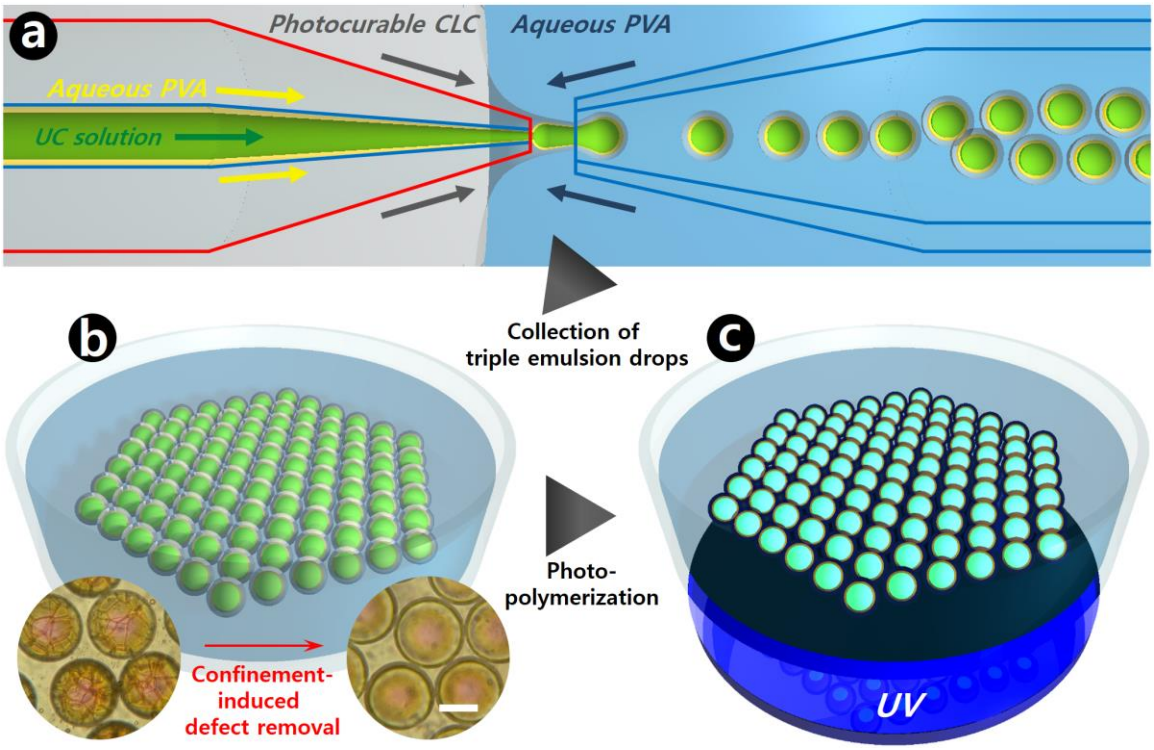

Figure 3.2. Schematic production process of triple emulsion microcapsules containing TTA-based UC cores and CLC shells. a) Continuous generation of triple emulsions with an ultrathin alignment separation layer between UC core and CLC shell via a single dripping instability in flow-focusing microfluidic device, b) Interface-assisted planar alignment of CLC in the outer shell which is sandwiched by two aqueous PVA solutions of inner layer and surrounding, and c) Polymerization of CLC shells under UV illumination. The scale bar is 100 μm.

To produce uniform triple-emulsion drops, we used a glass capillary microfluidic device which has a flow-focusing region between two tapered cylindrical capillaries arranged in a square tube. As shown in **Figure 3.2**a, concurrent core-sheath jet flow was formed within the small inner injection capillary through suppression of hydrodynamic

instabilities, and instantaneously emulsified by countercurrent flow resulting in a stream of triple emulsions. For precise handling of the fluid flow, surfaces of the capillaries were treated to have appropriate wetting affinity to the fluids; the tip and outer wall of the injection capillary were hydrophobic (red solid line) while the inner wall of the injector and all the walls of the collector had hydrophilic surfaces (blue solid line).

The core oil phase of the emulsion comprised a solution of a hydrocarbon and a pair of TTA-based UC sensitizer-emitter chromophores. We used 1-bromohexadecane as a relatively low viscosity medium which supports external heavy atom effects that enable high quantum efficiency via enhanced intersystem crossing, as described previously in Chapter 2. Light stabilizers such as butylated hydroxytoluene and Tinuvin 765 (4 wt%) were incorporated into the solution to circumvent quenching by reactive oxygen species, thereby enabling anaerobic conditions, and facilitating TTA-UC emission. As a red-to-cyan UC pair, palladium tetraphenyltetrabenzoporphyrin (PdTPBP) and 9,10-bis(phenylethynyl) anthracene (BPEA) were dissolved in the solution to serve as sensitizer and emitter, respectively. Upon selective excitation of the corresponding PdTPBP Q-band (around 630 nm), delayed BPEA singlet fluorescence occurred through a series of triplet-triplet energy transfer and annihilation steps (**Figure 3.3**). The UC solution was injected though the small capillary, and a 6 wt% polyvinyl alcohol (PVA, Mw 13000-23000, 87-89% hydrolyzed) aqueous solution containing 5 vol% glycerol was then injected through the untapered opening of the injection capillary. The two immiscible fluids (1-bromohexadecane and aqueous PVA solution; most proportion does not form a homogeneous solution at room temperature.) flowed coaxially, with the water forming a stable film along the wall as a result of its significant wetting affinity with the

capillary. For a sufficiently large flow rate of the innermost oil in a given inner aqueous flow, a stable oil jet could be generated in the injection capillary.

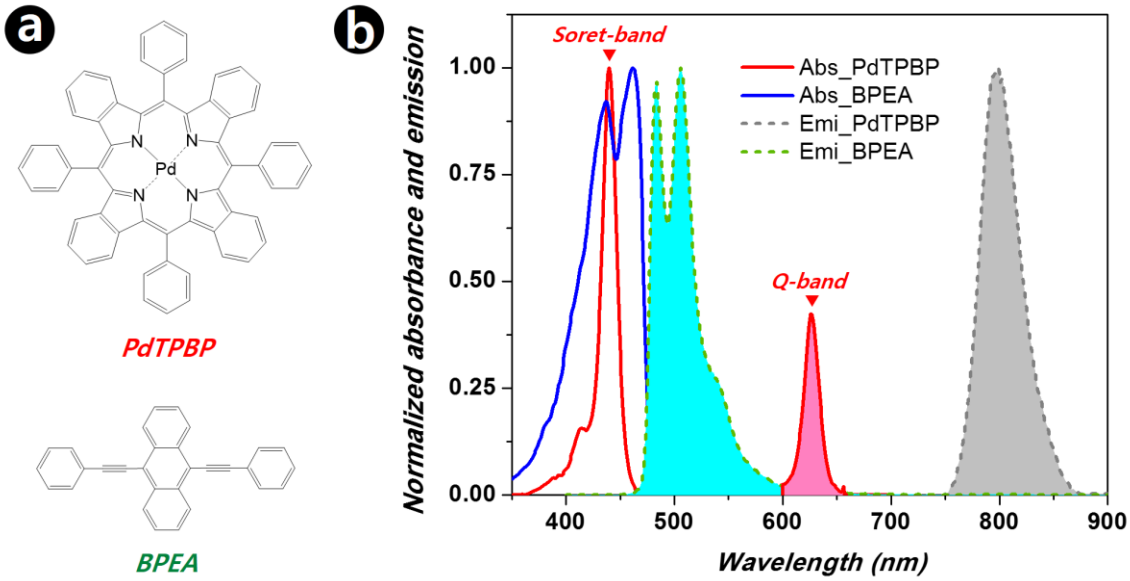

Figure 3.3. a) Molecular structures of chromophores used for a red-to-cyan TTA-based upconversion. b) Normalized absorbance and emission spectra of PdTPBP and BPEA dissolved in 1-bromohexadecane solution. The concentrations of PdTPBP and BPEA are about 8.8 μM and 132 μM, respectively; it was diluted from the base solution. Red, cyan and gray shading areas indicate bands of the selective excitation, upconverted emission and phosphorescent emission, respectively.

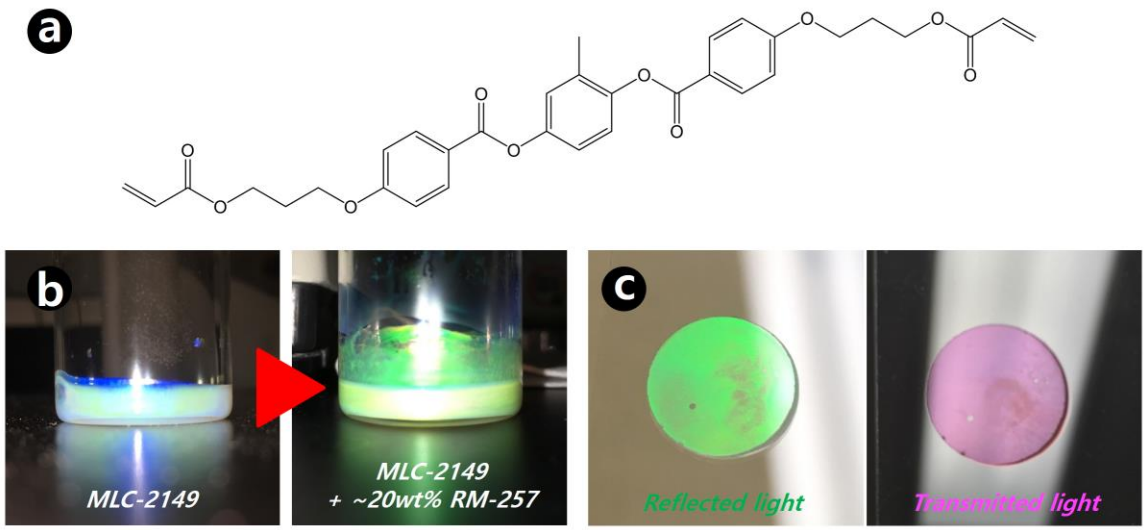

Figure 3.4. a) Molecular structure of reactive mesogen, RM-257, which has two acrylate functional groups. b) Digital images of MLC-2149 (base solution of chiral nematic liquid crystals) and CLC mixture including about 20 wt% RM-257 at normal flashing light. c) Reflectance and transmittance images of the polymerized CLC film between slide glasses.

The CLC was prepared by pre-mixing a chiral dopant and a nematic liquid crystal host, specifically, MLC-2149 (Merck). Depending on the concentration of the dopant, the resulting cholesteric structure exhibited different chiral pitch, thereby changing the wavelength of the stop band. As a crosslinker and secondary diluent host, the reactive mesogen RM-257 and 20 wt% photoinitiator was added to the CLC mixture to have a targeted optical band edge. For example, a MLC-2149 solution containing 10-20 wt% of RM-257 exhibits a normal-reflection stop band in the green (500-560 nm). As shown in **Figure 3.4**, the blue (~470 nm) stop band of MLC-2149 solution shifted to the green (~560 nm) by adding about 20 wt% of RM-257, which exhibits magenta in transmission as a combination of red and blue light. The viscous photocurable CLC solution was

injected as the outer oil phase through the interstice between the injection capillary and square tube, and a 6 wt% PVA aqueous solution containing 5 vol% glycerol was then injected as the continuous phase through the interstice between the collection capillary and the square tube. The jet of oil-in-water in the injection capillary became surrounded by the CLC prepolymer solution at the focusing region, and after passing through the widening channel of the collection tip, the compound jet broke up into monodisperse triple-emulsion drops within the continuous aqueous phase. The emulsions were then collected in a glass petri dish containing a 6 wt% PVA solution.

The liquid crystal molecules preferred to align parallel to the interface of the inner and surrounding aqueous phases, which was promoted at the boundary conditions with PVA and geometric confinement. The drops were initially opaque because of light scattering from oily streak defects in the shell (**Figure 3.2**b): these disappeared over time.[100] The geometric confinement of the shell with two spherical aqueous interfaces dramatically reduced the time of this process.[101] For a shell with a thickness of less than 10 μm, the process time was about one hour. In the final state there are still defects in the shell as a result of the spherical topology of the boundaries. In the case of nematic shells, the ground state consists of four disclination lines spanning the thickness of the shell.[97] In cholesteric shells, other defects are expected.[102] However, their number is still small and only affect the optical properties of the shells in their immediate vicinity. Hence, from this point of view, their effect is small and we do not explicitly discuss them any further. In their final state, the CLC shells of the emulsion drops were polymerized by a one second exposure to focused ultraviolet irradiation (**Figure 3.2**c). The capsules fully retained their optical quality, with little degradation in molecular order.

3.3.2 Planar alignment of CLC shell in triple emulsion capsules

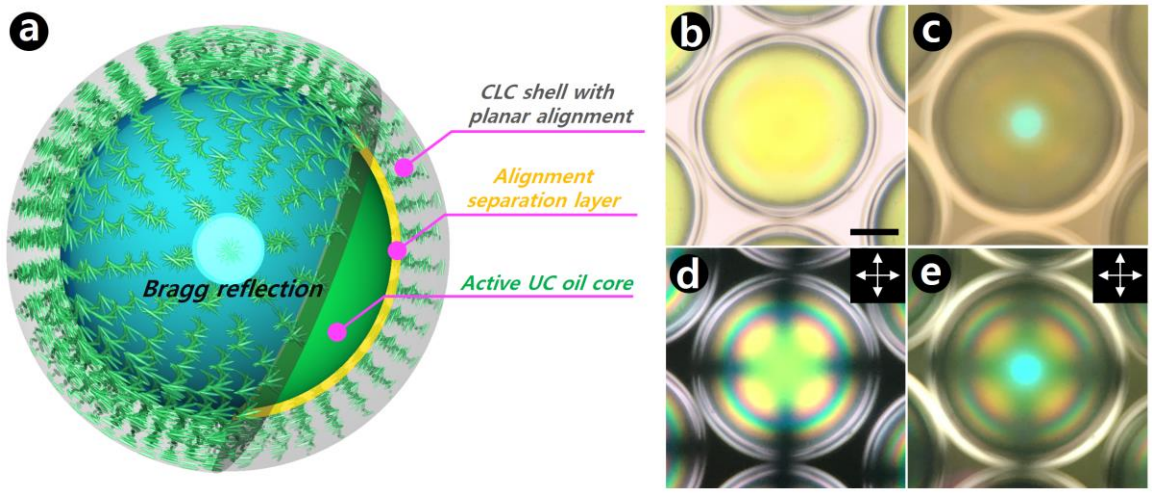

Figure 3.5. Distributed Bragg reflection from planar aligned CLC molecules in the outer shell of triple emulsion microcapsules. a) Schematic depicting the compartmentalized phases in a capsule. Since the defects in the shell due to the spherical topology only affect the optical properties of the shell locally, and there is always a small number of them present, for simplicity, we do not show them. Optical microscopy images in b) transmittance and c) reflectance. Cross-polarized microscopy images in d) transmittance and e) reflectance. The scale bar is 50 μm.

As shown in the schematic presented in **Figure 3.5**a, the resultant microcapsules were composed of an active UC oil core, an inner aqueous alignment separation layer, and an outer CLC shell. The core has a light yellowish green color due to red and blue spectral absorption of the UC chromophores (**Figure 3.5**b). The CLC shell possesses the periodic structure of the CLC with planar alignment. Therefore, the helical axis is aligned to be perpendicular to the interfaces, omnidirectionally reflecting the light in the stop band. The striking reflection color can be observed in the central region of the

microcapsules (**Figure 3.5**c). Satisfying Bragg conditions, the constructive reflection light at the stop band wavelength (λ) is determined by the length of a full twist in the CLC helix; $\lambda = p\, n_{\text{eff}} \sin\theta$, where p is the chiral pitch, n_{eff} is the effective refractive index, and θ is the angle of the incident light. Since the stop band is narrow, the microcapsules are transparent to nearly all other wavelengths (**Figure 3.6**b). To verify the configuration of the twisted axes in the CLC shell, optical textures of the microcapsules were taken using cross-polarized optical microscopy; these are shown in **Figure 3.6**d-e. Due to the optically birefringent nature of chiral nematic liquid crystals corresponding with the proximity of the pitch and the wavelengths of the incident light, a Maltese cross pattern with a set of concentric rings was observed in both transmission and reflection modes between crossed polarizers. Moving away from the center of the capsules, the large inclination of the helix axis in the curved geometry of the shell was projected in the oscillation plane of the light; the black cross turned darker as the capsule edges were approached.

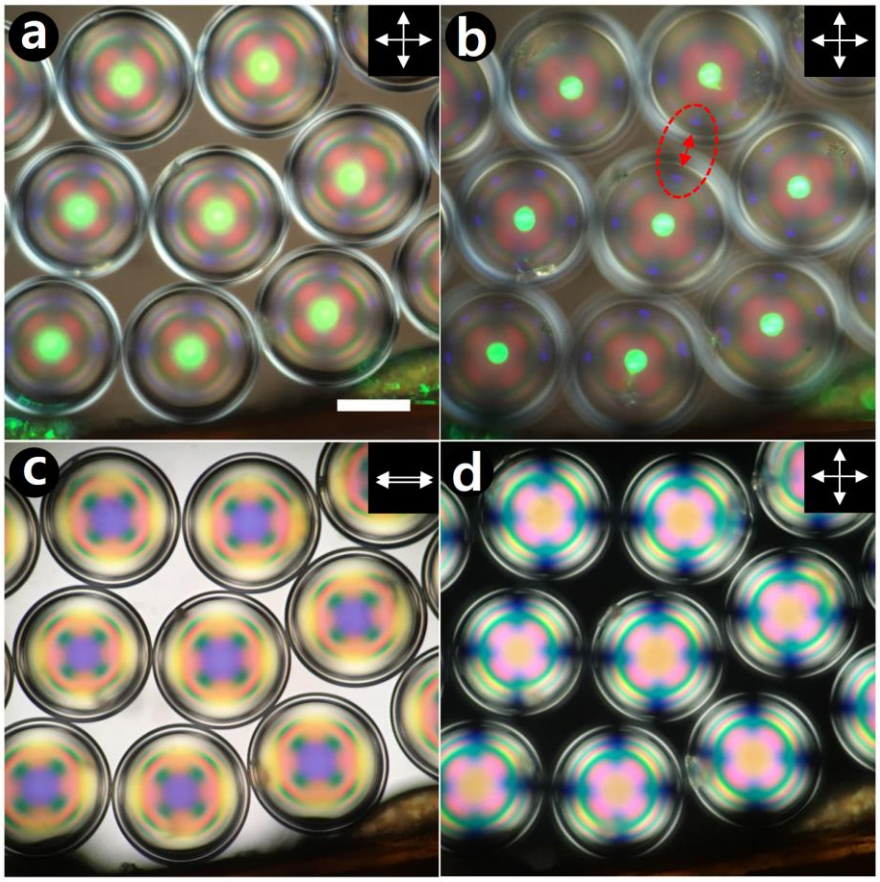

Figure 3.6. Optical microscopy images of double emulsion capsules with planar aligned CLC shell. a-b) Cross-polarized reflectance images taken by different focused planes at a) middle and b) top surface of the capsules. Red arrow in the doted circle indicates cross-communication between neighbor capsules. c-d) Transmittance images at clear focal plane between c) parallel and d) cross polarizers. The scale bar is 100 µm.

As collected in a confined space, the capsules with narrow size distribution were readily assembled into an ordered film having a hexagonal array. When the monodisperse microcapsules were placed close to others in the same plane, additional reflection patterns around the border developed due to photonic cross-communication with

neighboring capsules.[103] Incident light that impinged with a 45° orientation to the spherical surface was reflected between the interrogated and adjacent capsules, from which Bragg reflections were eventually observed in a direction normal to the substrate. Although these patterns were not discernable in the triple emulsion due to the low light source intensity, purple dots interacted between the emulsions where core oil was absent, were clearly observed under cross-polarized reflection as shown in **Figure 3.6**a-b. The reflection wavelength of the cross-communication patterns was estimated by $\lambda \cos 45^{o}$, which is consistent with 396 nm. Moreover, complementary colors of cross patterns and concentric rings between parallel and cross polarized reflectance images were observed as apparent optical evidence of radially oriented helical axes in the CLC shells (**Figure 3.6**c-d).

3.3.3 Amplified TTA-UC emission by photonic shell of planar CLC

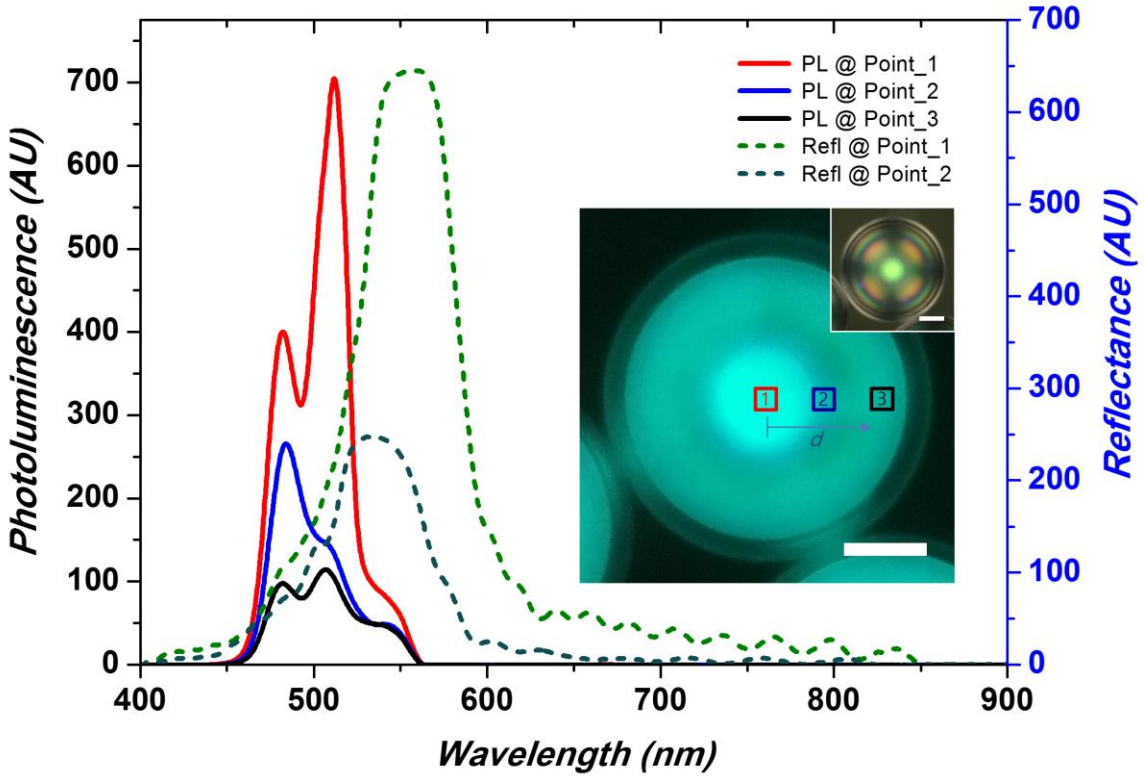

Figure 3.7. Amplified spontaneous emission (solid lines) of TTA-based upconversion in a triple emulsion microcapsule and optical reflection bandgap (dotted lines) of CLC shell. Fluorescence spectra and the associated microscopy image (inset) were obtained through a 561 nm short pass filter under tungsten lamp excitation with a 628±16 nm band pass filter. The distances of detected points 1, 2 and 3 from the center are 0, 34, and 70 µm, respectively. The small optical microscopy image (inset) was taken under cross-polarized microscopy. The scale bars are 50 µm.

Commensurate with Bragg's law, the reflection position of the stop band gradually shifted to shorter wavelength as the angle between the normal and reflecting vectors increased, which is a function of the horizontal distance (d) from the origin;

$\lambda\sqrt{1-(d/r)^2}$, where r is the radius of the microcapsules. As shown in **Figure 3.7**, the normal reflectance spectrum of the microcapsules was peaked around 560 nm at the center of the microcapsule and at about 530 nm when considering a region 34 μm away from the center. Owing to the radially fashioned helical axes, the CLC shell in the triple emulsions behaved as an omnidirectional distributed Bragg reflection (DBR) resonator for TTA-based upconversion. If the emission spectrum overlapped with the CLC photonic bandgap, a change in photoluminescence of the chromophores could be observed; the emission will be enhanced at the photonic band edges and suppressed at the stop band.[104] Due to the high density of electromagnetic states, a sharp rise in photoluminescence at the band edge is expected. Monochromatically filtered images in the cross polarized transmission displayed distinctive patterns combined with fluorescence of the core and diffraction of the shell; blue intensity in the capsule center was weaker than that for green, and the dark ring moved towards the periphery as the wavelength of the selective reflection was shorter along the axis of the capsule (**Figure 3.8**).

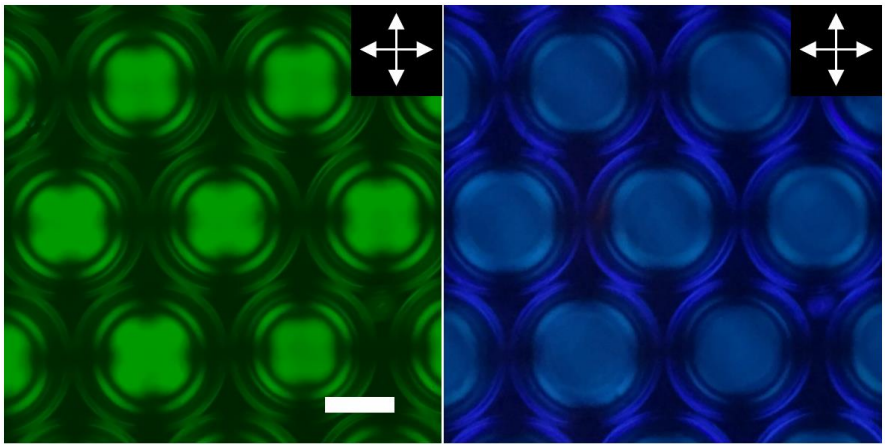

Figure 3.8. Optical microscopy images of triple emulsion capsules with planar aligned CLC shell under cross-polarizers with green (left) and blue (right) filters. The scale bar is 100 μm.

Using fluorescence microscopy, we observed amplified spontaneous emission (ASE) of delayed fluorescence from the microcapsules. As shown in the inset of **Figure 3.7**, fluorescence microscopy images exhibited characteristic concentric emission spectra under low intensity excitation using a 628±16 nm band pass filtered tungsten source. Due to spherical symmetry of the capsule, the extent of the resonance enhancement at a normal angle varied locally according to the shifted position of the stop band edge along the radial direction. Through a square aperture of the spectrophotometer integrated into the fluorescence microscope, we measured two dimensional spectra of the upconverted emission at different local positions. At the capsule center (point 1), very intense spontaneous emission was observed and the peak at about 510 nm significantly increased, a result that is consistent with the increase in density of states expected near the band edge at a normal angle. The ASE wavelength blue shifted with increased distance from the center, which corresponds to a shift of the stop band originating from the angle dependence of the helical resonance of the CLC. At point 2 (d ~34 μm), emission from the 480 nm peak appeared enhanced relative to that at 510 nm. In contrast, the resonance effect was not observed when the detection position was far from the spectral band of upconverted emission. Because the stop band is lower than 400nm at point 3 (d ~70 μm), spectral overlap did not occur; the relative ratio between the emission peaks is comparable to that of the bulk solution, the PdTPBP-BPEA pair at a fixed concentration in 1-bromohexadecane oil (cyan shading area in **Figure 3.3b**). In contrast with photon

localization in the vicinity of the band edge, we observed inhibition of spontaneous UC emission when the stop band of the CLC shell was fully covered over the emission spectrum. By adding about 12 wt% of RM-257 into the CLC solution, the central area of the capsules showed a cyan colored stop band (~510 nm band center) at a normal angle, resulting in weak green emission from the center (**Figure 3.9**).

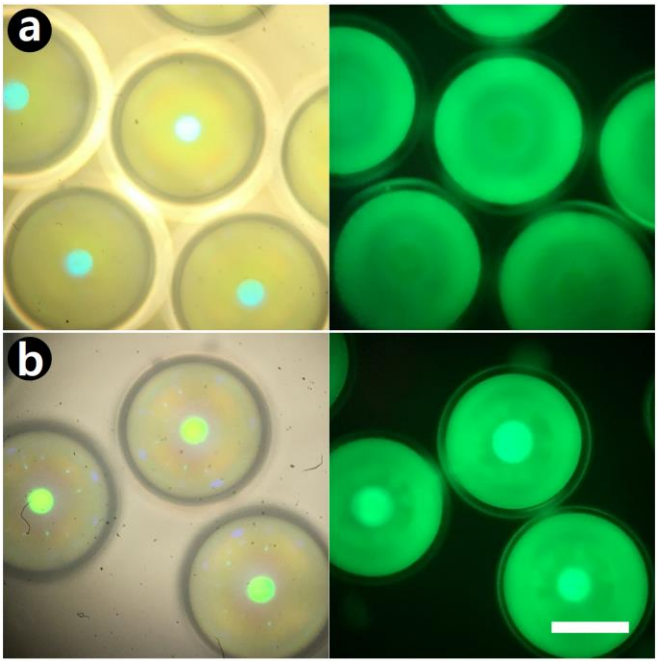

Figure 3.9. Optical microscopy images in reflectance (left, focused at top surface) and fluorescence images with a green filter (right, focused at middle) of triple emulsion capsules with planar aligned CLC shell having different stop band positions at a) ~510 nm and b) ~560 nm. The scale bar is 100 µm.

3.4 Conclusion

In conclusion, we describe a microfluidic approach to produce uniform light emitting microcapsules composed of a triplet fusion-based upconversion core modulated by CLC shell DBR resonator. By controlling fluid wettability in confined capillaries, ultrathin aqueous PVA solution is introduced into the triple emulsion as a middle layer which separates the TTA-UC core from the CLC shell without physical deterioration, and importantly supports planar alignment of CLC molecules at the interface. Owing to the small volume between the two parallel boundaries, helical arrangement of the CLC is readily achieved in a short time. The liquid crystal phase, including a reactive mesogen with high optical transparency, can be polymerized under UV irradiation. The cured microcapsules are stable in aqueous medium, which allows for a wide range of photonic applications, including photocatalysis and biomedical imaging. The periodic structure of CLCs in the shell supported angle-dependent ASE of delayed fluorescence from the core under low intensity excitation. Due to their uniformity, the microcapsules can be used not only as single omnidirectional light units, but also as building blocks for integrated photonic devices, which can potentially provide for structured microlasing properties with specific end uses, including photonic inks, random lasers and volumetric displays. Moreover, we expect that the thermochromic properties of CLCs have significant potential to control the bandgap, leading to dynamic tuning of ASE resonance upon TTA-UC.

CHAPTER 4. DOUBLE RESONANT PLASMON EFFECT OF GOLD NANORODS ON PHOTON UPCONVERSION

Photon upconversion assisted by triplet fusion is an attractive anti-Stokes phenomenon owing to its unique properties and great application potentials. However, it still faces many challenges in utilizing it for practical purposes. In order to efficiently enhance the delayed upconversion fluorescence, we propose a scheme exploiting the double resonant plasmon modes of gold nanorods. The longitudinal and transverse surface plasmon resonance of gold nanorods enables simultaneous enhancement of the excitation and emission efficiencies, respectively. Using an aromatic additive, tailored synthesis of colloidal gold nanorods with improved uniformity has been demonstrated through well-established protocols. Thiol-modified poly(ethylene glycol) has been used to replace conventional capping agents from the surfaces of gold nanorods to form a silica shell directly on the nanorods using the standard Stöber process. The obtained silica shells are uniform and homogeneous, and the method allows precise control over the thickness of the shell. The enhancement of upconverted emission intensity was demonstrated in around 10-20 nm of dielectric distance between gold nanorods and chromophores, so called hotspots. Approximately, a maximum 3-fold increase of fluorescence relative to that of the bare solution was observed for a 13 nm shell by the double resonance for red-to-cyan upconversion.

4.1 Introduction

Photon upconversion (UC) based on triplet-triplet annihilation (TTA) produces an anti-Stokes emission under low power-density of continuous excitation, such as sunlight, [38, 53] enabling a wide range of potential applications, including low-threshold integrated light sources for photovoltaics,[13-17] photocatalysis[18-20] and bioimaging.[23, 26, 74] It can combine two or more low frequency photons to generate one high frequency photon. The mechanism of TTA-UC processes lies in a series of diffusional energy transfer steps between two molecules, sensitizer and emitter: triplet-triplet energy transfer (TTEA) and TTA.[31] Upon irradiation, the triplet sensitizer enables its long-lived triplet excited state by enhancing intersystem crossing (ISC). In close proximity with an increased population of triplet states, energy transfer can occur between triplet states of the sensitizer and emitter. Then, two triplet excited states of emitter molecules undergo TTA, leading to subsequent generation of one singlet excited state. Finally, the upconverted fluorescence can be observed upon decay to the ground state.

Owing to the diffusion-limited nature of TTA-UC systems, effective media such as organic solvents with low viscosity and rubbery polymers with low glass transition temperature[31] had been widely studied to achieve high efficiencies of UC quantum yield. Still, however, there is a limited selection of inert, effective media to enhance the quantum yield in terms of energy transfer. Dye-doped polymer nanoparticles have been studied as an alternative to achieve confinement at the nanoscales, but stable upconverted emission is yet to be observed in ambient conditions.[65] Recently, microfluidic encapsulation approaches have been demonstrated as a new platform which enables retention of molecular mobility or triplet exciton diffusion in the UC core solution, but

also provides mechanical integrity and protection from external threats by a polymeric shell.[51] Although facilitation of energy transfer required for TTA-UC can result in maximum efficiency of the process, overall efficiency of the upconverted delayed fluorescence is related to the excitation, energy transfer and emission efficiencies, and improvement of the efficiency can be simply described as $\eta_{UC} = \eta_{Ex} \cdot \eta_{ET} \cdot \eta_{Em}$. To date, however, the majority of studies to determine the quantum yield have been carried out in terms of biomolecular interactions. Thus, there are still room to improve the efficiencies of the TTA-UC process regarding excitation (absorption) and emission.

Plasmonics has been one of the most exciting and active research areas in nanoscience and nanotechnology. Metallic nanostructures exhibit fascinating plasmonic properties, providing ways to manipulate electromagnetic waves beyond the diffraction limit[105] and to tailor light-matter interactions at the nanoscale[106] with potential applications ranging from bioscience,[107] catalysis,[108] photovoltaics[109] and sensors[110] to information technology uses such as imaging[111] and storage.[112] The excitation of localized surface plasmon resonance (SPR) in metal nanoparticles results in the nanoscale confinement of electromagnetic fields near the metal surface and a significant enhancement in the local density of optical states.[113] These properties have been widely employed to study the interactions between plasmons and fluorophores, such as fluorescence enhancement.[114] In principle, for plasmon-enhanced fluorescence, there are two kinds of enhancement schemes: excitation enhancement and emission enhancement. The excitation wavelength of pumping sources and the emission wavelength of fluorescence molecules are described as λ_{Ex} and λ_{Em}, respectively. When the SPR wavelength of the metal particle is simultaneously matched with λ_{Ex} and λ_{Em}, the highest

efficiencies of both excitation and emission are expected to be achieved by tailoring the electromagnetic field at the position of an upconverting chromophore pair in a given medium.

4.2 Experimental Section

4.2.1 Materials

As an aromatic additive to synthesis of gold nanorods, sodium 3-methylsalicylate (NaMS, >97.0%) were purchased from TCI America. For seeded mediated growth of gold nanorods, hexadecyltrimethylammonium bromide (CTAB, >98.0%), hydrogen tetrachloroaurate trihydrate ($HAuCl_4 \cdot 3H_2O$), L-ascorbic acid (AA, >99%), silver nitrate ($AgNO_3$, >99%), sodium borohydride ($NaBH_4$, 99%) and (O-[2-(3-mercaptopropionylamino)ethyl]-O'-methyl-poly(ethylene glycol) (mPEG-SH, MW 5000) were purchased from Sigma-Aldrich. For silica coating by the Stöber method, tetraethyl orthosilicate (TEOS, 99.999%), ammonium hydroxide solution (NH_4OH, 28% in water), ethanol (absolute, >99.8%) and isopropyl alcohol (IPA, >99.7%) were also purchased from Sigma-Aldrich.

4.2.2 Synthesis of gold nanorods

To prepare the seed solution, a 10 ml of 0.1 M CTAB solution with the gold precursor, 0.25 mM $HAuCl_4$, was dissolved in D.I. water at 70 ^oC. A 1 ml ice-cold water with fresh 0.06 M $NaBH_4$ was prepared and then added into the Au-CTAB complex solution at 30 ^oC under vigorous stirring (1150 rpm) for 2 min. The light brown seed solution was aged at room temperature for 30 min before use.

To prepare the growth solution, a 250 ml of 0.1 M CTAB solution with an aromatic additive, 25 mM NaMS, was dissolved in D.I water at 70 ^oC. Afterwards, a 6ml of 4 mM $AgNO_3$ and a 250 ml of 1 mM $HAuCl_4$ were added into the CTAB solution, it

was kept undisturbed at 30 ^{o}C for 15 min and then stirred at 400 rpm for 15 min. The solution was vigorously stirred for 30 sec after a 1 ml of 0.064 M AA was added into the mixture. The growth solution was used right after preparation.

Lastly, 0.8 ml of the seed solution was added into the growth solution. The resultant mixture was stirred for 30 sec and kept undisturbed at 30 ^{o}C for 12 hr for AuNR growth. The suspension was washed twice by centrifugation at 7500 rpm for 40 min and redispersed in a 250 ml of 1 mM CTAB solution.

4.2.3 Silica coating on gold nanorods

To facilitate the growth of uniform silica shells, a thiolated PEG was used to replace the surface capping agents CTAB on the AuNRs. A 0.3 ml of 18.75 mM mPEG-SH aqueous solution was added dropwise into a 10 ml AuNR suspension in 1 mM CTAB under vigorous stirring. After 3 hr, the reaction was stopped and the solution was washed twice by centrifugation at 7500 rpm for 20 min and redispersed in 15.6 ml of ethanol.

A solution of 1.8 ml of water and 0.143 ml NH_4OH (28% in water) were mixed with the 7.8 ml of AuNRs in ethanol. To control thickness of the silica coating, different amounts (between 0.4 ml and 1.2 ml) of TEOS solution (1 vol% in IPA) was injected dropwise into the mixture under gentle stirring. After a 2 hr reaction time, the solution was washed twice by centrifugation at 7500 rpm for 20 min and redispersed in 10ml of ethanol or water.

4.2.4 Preparation of chromophores-embedded solution with silica-coated gold nanorods

As red-to-cyan UC stock solutions, platinum tetraphenyltetrabenzoporphyrin (PtTPBP, Frontier Scientific) and 9,10-bis(phenylethynyl) anthracene (BPEA, Sigma-Aldrich) were separately dissolved in 1-bromohexadecane by heating at 75 °C. The final concentrations of PdTPBP and BPEA were about 0.22 mM and 2.64 mM, respectively. 5 vol% of the ethanol suspension with silica-coated gold nanorods was added to the mixture and heated to 60 ^{o}C to selectively evaporate ethanol overnight.

4.2.5 Characterization

Absorbance and photoluminescence measurements were carried out using UV-Vis spectrometer (8453, Agilent) and spectrofluorophotometer (RF-5301pc, Shimadzu), respectively. The size of AuNRs and the thickness of silica coating were measured by transmission electron microscopy (HT7700, Hitachi) after the sample was dried on a carbon-coated copper grid (200 mesh, Electron Microscopy Sciences). Dark field in reflection mode for AuNRs was observed using an optical microscope (Olympus) equipped with a hyperspectral image system (CytoViva).

4.3 Results and Discussion

4.3.1 Improved synthesis of monodisperse gold nanorods using aromatic salt

Gold naorods are rod-shaped plasmonic nanoparticles with tunable, size dependent optical responses and a wide array of unique optical properties.[115-116] Gold nanorods absorb and scatter light more strongly than spherical nanoparticles, resulting in stronger field effects.[117] Due to photon confinement, strong electromagnetic fields are generated at the metal surface. The influence of the size on the surface plasmon resonance is relatively small in comparison to the effects of a change in shape: the SPR of gold nanoparticles is in a range from 520 to 580 nm when the size is controlled between 20-100 nm in diameter.[118] In addition, gold nanorod plasmon bands are readily tuned by changing the aspect ratio.[115]

Seed-mediated growth in the presence of the cationic surfactant CTAB has been widely adopted for the preparation of gold NRs.[115, 119] The NRs obtained typically exhibit LSPRs greater than 700 nm, corresponding to a NR aspect ratio larger than 2.8. Preparation of gold NRs of relatively small aspect ratio has been demonstrated using mild oxidation with Au(III)-CTAB complexes,[120] O_2 or H_2O_2 in an acidic environment,[121-122] anisotropic chemical etching with cyanide or ferric chloride,[123-124] laser-induced thermal heating,[125] and controlled overgrowth of preformed gold NRs.[126] However, these post-synthetic modification strategies usually offer limited control over size and shape uniformity of the final products. Thus, a one-step synthesis of monodisperse short gold NRs with LSPRs in the visible region is still desirable.

To grow short gold NRs, here we used salicylate-based organic salts as the aromatic additive together with CTAB whose concentration was reduced by 50% compared to the standard recipes (0.1 M).[127] It has been widely accepted that the hydrophobic benzene ring of the additive tends to penetrate the hydrophobic alkyl chain of the CTAB monomer.[128] Meanwhile, the salicylate anion can orient in such a way that the negatively charged COO^- group stands perpendicular to the surfactant and projects radially from the surface of the micelle into the bulk aqueous solution.[129] These two factors change synergistically the micellar packing parameter. Insertion of the phenyl moiety of the salts increases the effective volume of the hydrophobic chain of the CTAB micelle. Anion association reduces the micellar surface charge and decreases the effective area of the polar headgroup by reducing the electrostatic repulsion between the quaternary ammonium groups, promoting the spherical to rod-like micellar transition. In this work, the aromatic salt additive for gold NR synthesis is sodium 3-methylsalicylate (NaMS). **Figure 4.1**a-b shows the TEM images of gold NRs synthesized without and with 25mM NaMS present in the growth solution. The additive-assisted NRs have a relatively uniform average diameter of 15 nm and a length of 30 nm (corresponding to an aspect ratio of 2), giving rise to a LSPR peak centered at around 630 nm. Compared to the control sample, the strong and sharp LSPR peak was observed in the gold NRs sample with the aromatic salt additive shown in UV-Vis absorption graph of **Figure 4.1**c. The level of shape impurities such as spherical nanoparticles or nanoplates in as-synthesized samples is dramatically lower than those of previous gold NR preparations using silver-assisted seed-mediated growth, which was also evidenced by the

significantly reduced TSPR peak at around 520 nm of the gold NRs sample with the additive (**Figure 4.1**c).

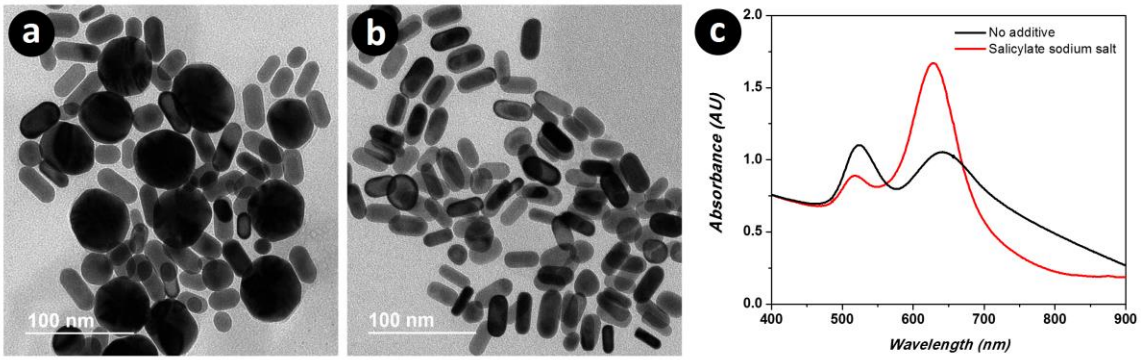

Figure 4.1. Synthesis of gold NRs with LSPR at around 630 nm. a) and b) TEM images of gold NRs synthesized (a) without and (b) with sodium 3-methylsalicylate salt additive in growth solution. c) UV-vis spectra of gold NRs corresponded to (a) and (b). Each spectrum was normalized to 0.76 by its absorption at 400 nm.

4.3.2 Double resonant plasmon modes of gold nanorods for TTA-UC

Here we propose a scheme utilizing the double resonant plasmon modes: the collective oscillation of conduction band electrons on the surface of gold nanorods give rise to two plasmonic resonance bands, the wavelength of which are defined by the aspect ratio and can be tuned from the visible to the near-infrared. The longitudinal and transverse surface plasmon resonance modes are simultaneously utilized to enhance the excitation and emission efficiency, respectively.

For TTA-UC an organometallic complex and an aromatic hydrocarbon are used as the sensitizer and emitter, respectively. Upon irradiation, the metal-to-ligand charge-transfer (MLCT) characteristics of the sensitizer enables its long-lived triplet excited state

by enhancing the intersystem crossing (ISC) rate, which results in triplet-triplet energy transfer (TTET) from the sensitizer to the acceptor. With the increased population of triplet acceptors, there becomes large probability that two triplet excited acceptor molecules then undergo TTA through direct collision which leads subsequent generation of one singlet excited state, producing the upconverted fluorescence upon decay to the ground state.

As a red-to-cyan UC pair, platinum (or palladium) tetraphenyl-tetrabenzoporphyrin (PtTPBP or PdTPBP) and 9,10-bis(phenylethynyl) anthracene (BPEA) were dissolved in 1-bromohexadecane to serve as sensitizer and emitter, respectively. 1-bromohexadecane was chosen as a medium for TTA-UC because of its relatively low viscosity, transparency and non-volatile nature. It also exhibits better solvation capacity for chromophores because of the increased strength of the intermolecular forces or the polarity derived from the strongly electronegative halogen atom. More importantly, incorporation of heavy atoms into the solvent increases spin-orbital coupling of the excited singlet and triplet states, resulting in enhancement of intersystem crossing, increased lifetime of phosphorescent decay, and significant improvement of the UC quantum efficiency. Upon selective excitation of the corresponding PtTPBP Q-band (peak around 620 nm) or PdTPBP Q-band (peak around 630 nm), delayed BPEA singlet fluorescence (green shading area with peaks around 480 nm and 510 nm, UC) occurred through a series of triplet-triplet energy transfer and annihilation steps (**Figure 4.2**). Phosphorescence emissions (dark yellow or gray shading areas, DC) were also observed from decay of the triplet excited state of the sensitizers when rate of energy transfer was limited.

The targeted aspect ratio of the gold NRs was around two because the LSPR band with the peak at around 630 nm (light red shading area) can be overlapped with two sensitizers' absorbance (Q-bands) and the TSPR band with the peak at around 520 nm (light green shading area) can be matched with BPEA's emission, as shown in **Figure 4.2**.

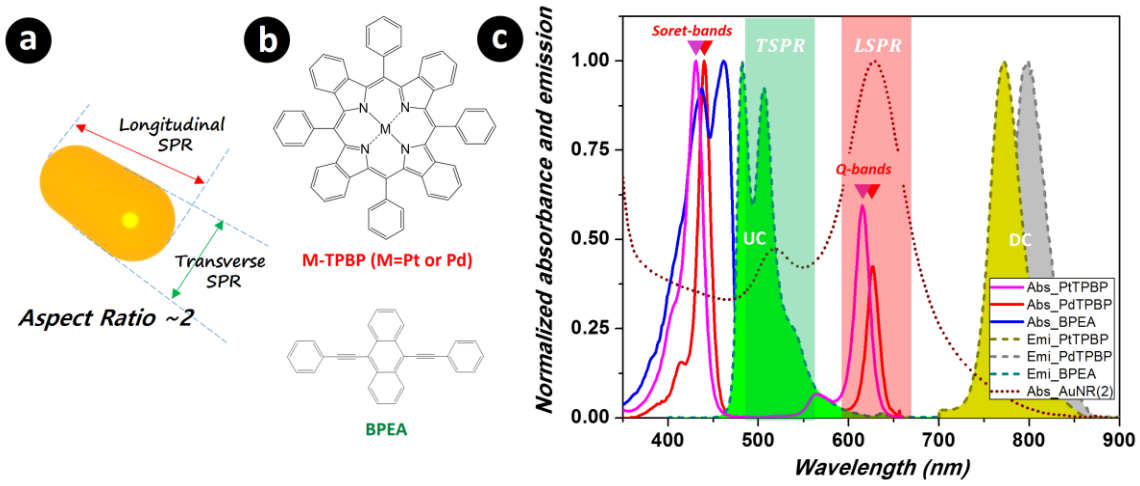

Figure 4.2. Upconverted fluorescence enhancement mechanism assisted by the LSPR and TSPR modes of gold nanorods. a) Schematic of the gold nanorods with aspect ratio of 2 (corresponding to the sample of Figure 4.1b), b) Molecular structures of sensitizer and emitter for red-to-green upconversion, and c) Normalized absorbance and emission of sensitizers and emitter dissolved in 1-bromohexadecane, and normalized absorbance of the gold nanorods dispersed in CTAB solution.

4.3.3 mPEG-mediated silica coating on gold nanorods for controlled dielectric spacer

It is known that fluorescence excitation and emission processes can be altered when a fluorophore is near a plasmonic nanoparticle.[130] The electromagnetic field strength is most concentrated at the surface of the plasmonic nanoparticles and decays exponentially as a function of distance. The nanoparticle and fluorophore form an electromagnetically coupled system, which when excited leads to additional de-excitation pathways. This results in higher excitation rates and/or enhanced radiative decay rates of the fluorophore and fluorescence emission enhancement. However, in some instances, fluorescence may instead be quenched if the excited fluorophores relax rapidly by nonradiative energy transfer into the surface plasmon resonance. Because of these two competing processes at a certain distance from the plasmon surface, energy transfer into the plasmon is reduced but the electromagnetic field strength can still be enough to enhance fluorescence emission.

As a dielectric spacer, silica allows for good control of distance between chromophores and gold nanorods.[131] Although the CTAB bilayer on the surface of the gold NRs in as-synthesized samples helps to prevent aggregation, the nanoparticles were easily merged each other after washing step, as shown in the TEM image of **Figure 4.3**a. Moreover, the successful growth silica shells on the nanoparticles stabilized in CTAB solution was hindered by the low chemical affinity between components. Therefore, surface priming for silica coating with coupling agents, surfactant, and polymers has been widely reported to increase the affinity of the gold surface toward silica, but also to provide the colloids with sufficient stability to be transferred into ethanol or isopropanol so that the Stöber method can be used for the growth of uniform silica shells on gold

nanoparticles. As a rapid and simple strategy, using a type of methoxy-poly(ethylene glycol)-thiol (mPEG-SH) as a ligand exchange coupling agent allows homogeneous coating with a high degree of control over shell thickness.[132] Driven by the strong interaction of thiol groups with the gold surface, original capping agents (CTAB bilayers) were replaced with mPEG-SH. As shown in **Figure 4.3**b, the mPEG-capped nanoparticles were very stable after washing and readily transferred into a base solution, i.e. ethanol/ammonia mixture, where growth of silica coating can be directly carried out on the particle surfaces through the standard coating method, limiting formation of free silica nanoparticles (**Figure 4.3**c). The resultant silica-coated gold nanorods were stable with no observed aggregation, allowing investigation of distance-dependent fluorescence behavior.

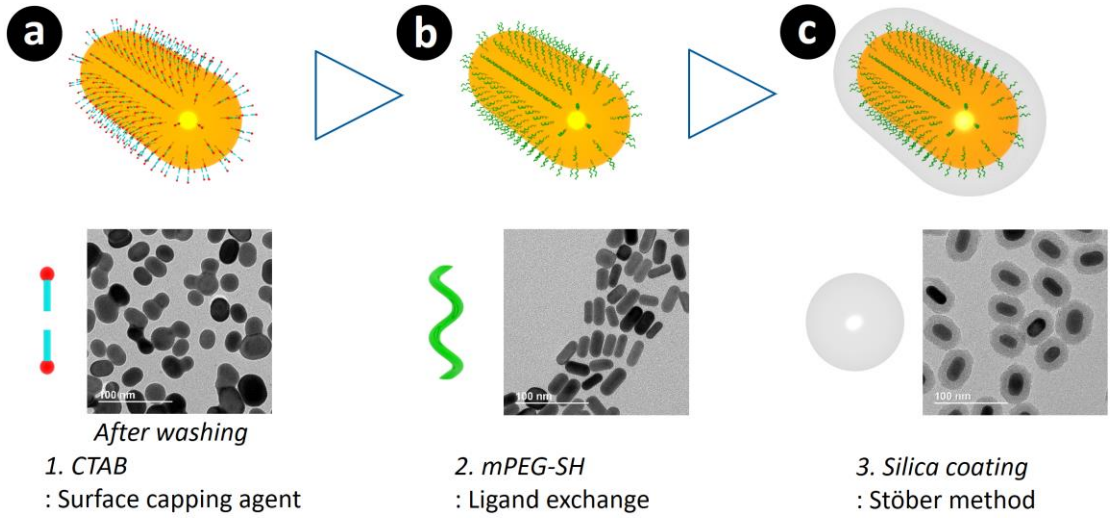

Figure 4.3. mPEG-mediated silica coating of gold nanorods. a) Co-agglomeration of as-synthesized gold nanorods during washing step, b) Ligand exchange with mPEG-

thiol capping agent on surface of the gold nanorods, and c) Uniform silica coating on gold nanorods transferred to base ethanol by standard Stöber method.

4.3.4 Distance-dependent resonance effect of silica-coated gold nanorods on upconverted fluorescence

In the present method, the thickness of the silica coating on mPEG-capped gold nanorods was precisely controlled by adding different amounts of precursor TEOS into the mixture. The hydrolysis and condensation of tetraalkylsilicates to form silica can be catalysed by a change in pH. As a result, highly reproducible silica shells for the dielectric layer were achieved for control of chromophore-metal distances. A different amount of TEOS solution (1 vol% in IPA), between 0.4 ml and 1.2 ml, was injected dropwise into the mixture, resulting in three different thicknesses of silica shells in a range from around 7 nm to 22 nm. It is easy to measure the thickness by TEM as shown in **Figure 4.4**. As aforementioned, the silica coating reduced aggregation of the gold nanorods, increased solubility of the nanorods in organic solvents, and is easily functionalized further with various silanes. **Figure 4.5** shows that well-spread gold nanorods with 13 nm silica shells were produced after ethanol was fully evaporated from the concentrated sample.

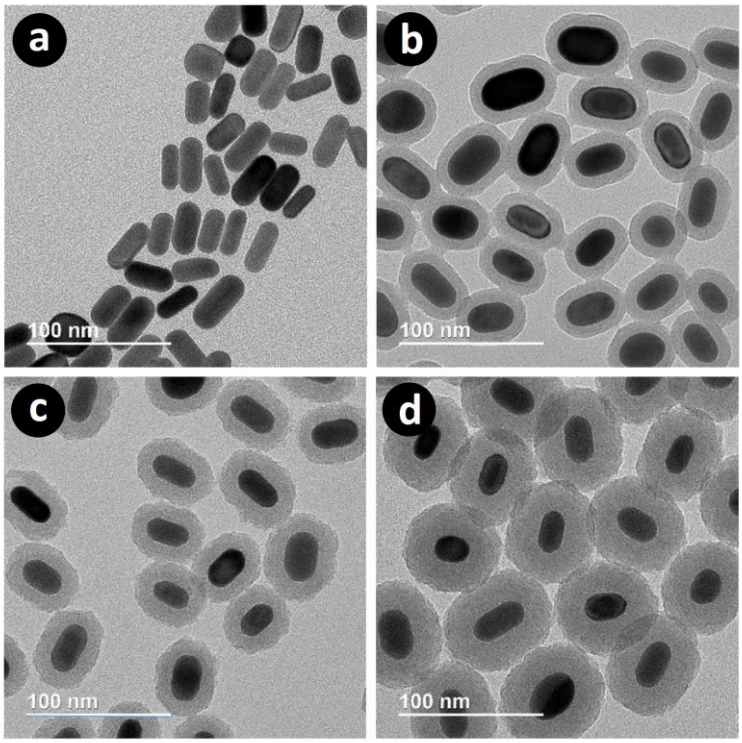

Figure 4.4. Highly controlled silica coating of gold nanorods with different thickness. TEM images of a) mPEG-capped gold nanorods, b) around 7.5 nm, c) 13 nm, and d) 22.5 nm thickness formation of silica shells on gold nanorods.

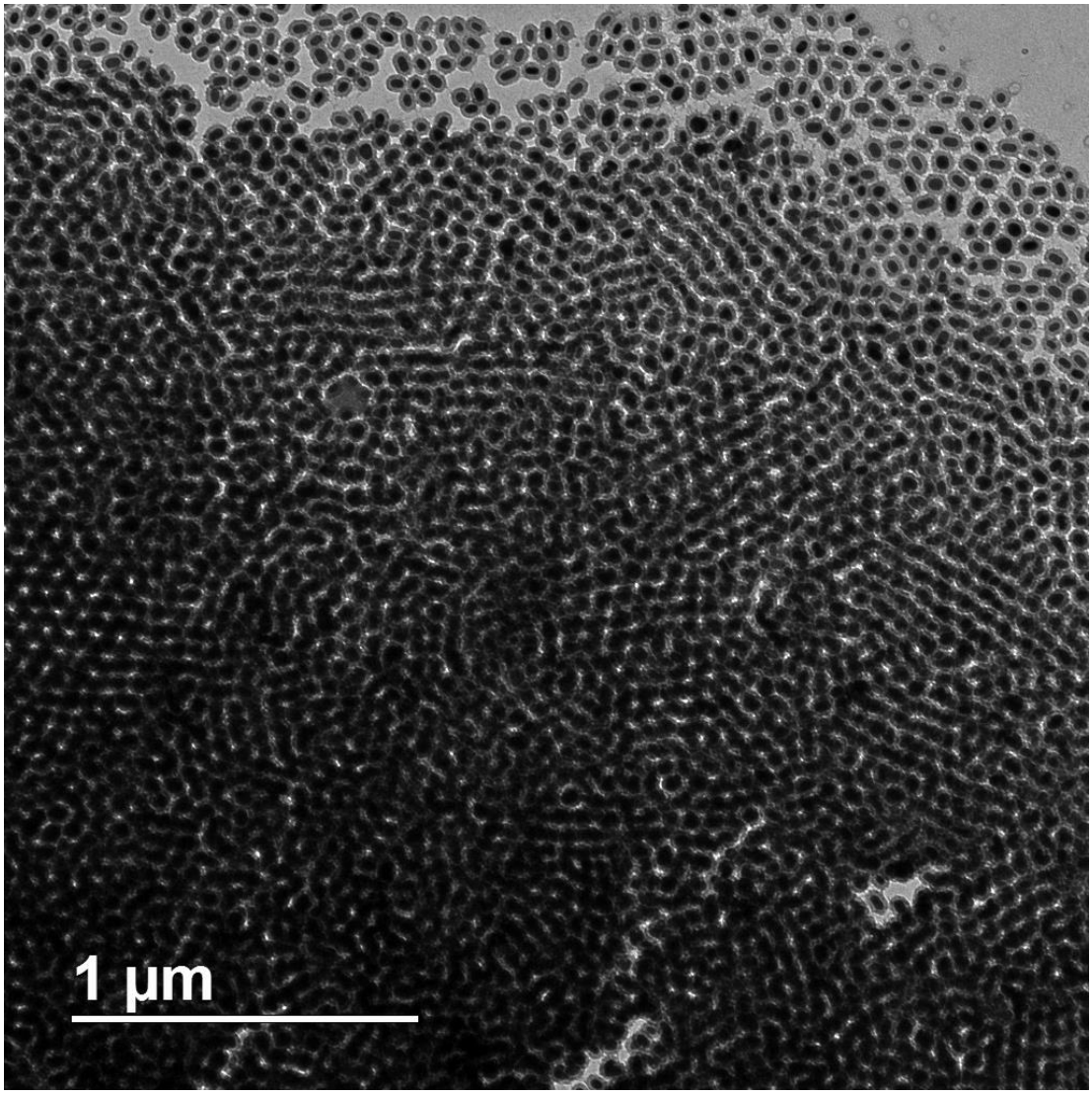

Figure 4.5. TEM image of gold nanorods with 13 nm of silica shell after slow evaporation of ethanol at room temperature.

The relative intensities of UC emission relative to bare UC brominated oil solution without gold nanorods were plotted as a function of silica shell thickness. It is noted that the sample for 0 nm thickness of silica shell refers mPEG-capped gold nanorods before silica coating process. No emission was detected from mPEG-capped or silica-coated gold nanorods alone, without chromophores, suggesting that scattering from

the nanorods was minimal. The results of the steady-state upconverted fluorescence measurement are shown in **Figure 4.6**, where the inset depicts dark-field images of gold nanorods dispersed in the UC solution. The highest enhancement was observed at 13 nm thickness, showing approximately a three-fold increase of upconverted emission intensity compared to the bare UC solution which contained PtTPBP and BPEA. However, a closer distance between chromophores and nanoparticles (without silica coating) reduced the emission intensity, which might be attributed to quenching mechanisms such as nonradiative relaxation.

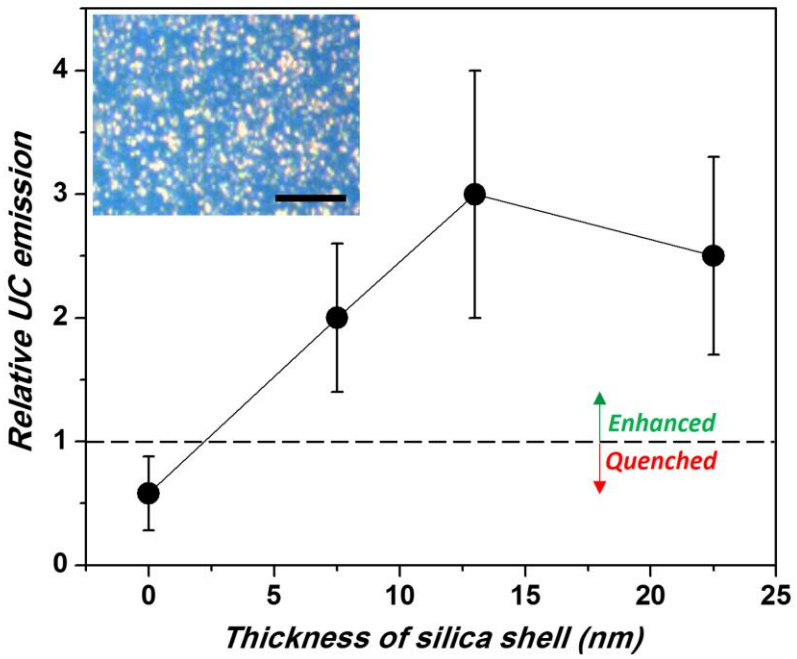

Figure 4.6. Steady-state relative intensity of upconverted delayed fluorescence from a red-to-cyan PtTPBP and BPEA pair dissolved in 1-bromohexadecane solution including gold nanorods with different thickness of silica shell relative to pristine UC solution without gold nanorods. Inset shows dark-field optical microscopy of silica-coated gold nanorods in UC solution. The scale bar is 20 µm.

4.4 Conclusion

We have observed distance-dependent TTA-UC emission of a PtTPBP and BPEA pair solution with silica-coated gold nanorods when there were spectral overlap between the nanorod LSPR/TSPR bands and the chromophores absorption/emission bands. By introducing an aromatic salt additive into the seed-mediated synthesis of gold nanorods, uniform gold nanorods with LSPR less than 700 nm were produced. Using poly(ethylene glycol) as a primer coupling agent for silica coating of gold nanorods, homogenous coatings with different thicknesses of silica shell were achieved through the standard Stöber method. Steady-state photoluminescence measurements demonstrated that an increase in upconverted delayed fluorescence with approximately a three-fold increase in maximum intensity was observed at a shell thickness of 13 nm silica on the gold nanorods. Quenching was also observed at a closer distance than the 'hotspot', resulting in the reduction in the upconverted intensity. These results reveal that plasmon-chromophore coupling is a viable option to increase the potential for highly integrated applications of photon management such as photovoltaics, photocatalysts, and bioimaging.

CHAPTER 5. CONCLUSION AND FUTURE WORK

5.1 Conclusion

The triplet fusion-based delayed fluorescence is a result of the following three steps: (1) light absorption, (2) a series of energy transfers (TTEA and TTA), and (3) emission, as described in **Figure 1.8**. Thus, each step or a combination of multiple steps could be considered as guidelines to improve the overall efficiency of upconversion. The emission intensity in such bimolecular systems is a quadratic function of the excitation power in a weak annihilation limit which is involved in most cases for practical applications. Thus, local surface plasmon resonance has been proposed to enhance the efficiency of absorption, emission or both, simultaneously for higher probability of light-matter interaction. Second, the exchange energy transfer has been verified as a diffusion-limited process which requires fast bimolecular mobility to efficiently overlap wavefunctions. Thus, most research efforts have been extensively focused on embedding and encapsulation methods for minimizing restriction of molecular diffusion. Lastly, the emission happens at any directional way after annihilation in energy transfer step, resulting in a restriction of the quantum yield to that of bulk base solutions and a limitation of materials choice. To date, very few studies have been carried out for TTA-UC to achieve a low threshold emission with photonic structures which could create an optical resonance cavity.

In chapter 2, we designed a single-step microfluidic emulsification approach to produce monodisperse triple emulsion capsules with an ultrathin intermediate layer that can fully isolate the core oil from the outer phase, which provides high encapsulation

efficiency while avoiding cross-contamination. By introducing the external heavy atom effect, 1-bromohexadecane oil core shows three-times higher upconverted quantum efficiency than hexadecane. Also, light stabilizers afforded remarkable improvement of photochemical stability under ambient condition. Furthermore, localized magneto-responsive functionalization of the microcapsule shell was demonstrated without unwanted light scattering.

In chapter 3, we described a microfluidic approach to produce uniform microcapsules of a triplet fusion-based upconversion with CLC outer shell. Through the confined capillaries, aqueous PVA solution was introduced into the triple emulsion as a middle layer as well as continuous phase which support planar alignment of CLC molecules at the interface. The liquid crystal phase, including a reactive mesogen with high optical transparency, can be polymerized under UV irradiation. The radially oriented helical structure of CLCs in the shell induced omnidirectional, but angle-dependent ASE of the delayed fluorescence from the core under low intensity excitation.

In chapter 4, we studied distance-dependent double resonant plasmon effects of silica-coated gold nanorods on TTA-UC emission, which was prepared by spectral overlap between the LSPR/TSPR bands of the gold nanorods and the excitation/emission bands of the chromophores. By introducing an aromatic salt additive into the seed-mediated synthesis of the gold nanorods, uniform gold nanorods with 620 nm LSPR (aspect ratio ~2) were obtained. Using a primer coupling agent, mPEG-thiol, a homogenous coating of silica on the gold nanorods was readily achieved through the standard coating method. Steady-state photoluminescence demonstrated an increase in

the delayed fluorescence with approximately a three-fold increase in maximum intensity with a silica shell thickness of 13 nm.

In summary, we successfully demonstrated the concept proposed in this thesis objective to achieve highly efficient TTA-UC under relatively low power density excitation for practical use. We first designed a single-step microfluidic encapsulation approach to develop the advanced core-shell structures, which allows us to maximize the effective energy transfer and thus significantly enhance the quantum yield. By incorporating an external photonic structure as an optical cavity into the capsule, moreover, amplified spontaneous upconverted emission was produced under a low intensity continuous-wave excitation. Finally, we showed that a large improvement of the delayed fluorescence can result from the local surface plasmon resonance coupling effect of gold metal nanoparticles by enhancing the absorption/emission efficiencies. In terms of materials science and engineering perspectives, our promising results would be expected to greatly contribute to developing new structures/methods and their potential applications.

5.2 Future Work

One of the greatest challenges facing our society is identification of new, reliable sources of clean energy. One attractive candidate is solar energy. The quantity of solar energy, a readily available renewable resource that impinges the Earth on a daily basis, is more than four orders of magnitude higher than the world's total daily energy use, estimated as 15 TW. Thus, the ability to harness and store solar energy in a cost-effective way could significantly and sustainably alleviate our growing global energy needs.

As transparent photovoltaics for building integration, dye-sensitized solar cells (DSCs) are potential candidates due to their transparency, low-cost manufacture, adjustable light absorption range and considerable temperature tolerance. However, DSCs require porous think electrode or additional scattering layer for high photon-to-electric conversion efficiency, causing opacity of electrode. In addition, the use of a large area electrode greatly increases the resistance of the electrode, thereby greatly reducing the efficiency of the solar cell. As an alternative, luminescent solar concentrators (LSCs) are proposed as an important element to solve a dilemma of highly transparent and highly efficient solar-to-electric conversion of the conventional solar cells.

Electrochemical photolysis of water is considered as an appealing, viable means of renewable energy generation to afford the simplest and most effective chemical fuel, hydrogen, in the world. Thus, the development of stable, high-performance photocatalysts represents a formidable challenge. To Among the barriers, the most challenge is the identification of suitable materials to allow utilization of the complete solar spectrum, particularly at lower energies with respect to the semiconductor bandgap.

5.2.1 Luminescent solar concentrator for solar energy harvesting

Photon upconversion of sunlight is an emerging concept to improve solar energy conversion efficiency. For conventional solar cells, one of the major energy loss mechanisms is the transmission of sub-bandgap photons. The use of upconversion materials provides a solution to the transmission loss by converting two sub-bandgap photons into one above-bandgap photon. Despite the emerging prospects, the integration of upconversion materials with existing systems has not resulted in much improved solar cell performance. One major limiting factor to the low conversion efficiency is the spatial incorporation of upconversion materials into solar cells. Only a small fraction of the upconverted light is captured by the solar cell because of energy loss due to internal scattering. In order words, a smaller distance between photoactive materials and the UC system improves performance in devices because the intensity of light emission is inversely proportional to the square of the distance from the origin of the source.

As a new way to achieve high efficiency, a luminescent solar concentrator (LSC) was proposed with transparent building integrated photovoltaics. A thin film of the LSC panel enables collection of a wide frequency range of photons from solar irradiation over a large area and was shown to produce concentrated light by trapping and directing the generated photons in the panel through total internal reflection. Fluorescent, active materials in a transparent medium absorb sunlight even at a large incident angle and then the produced light above a particular critical angle get reflected along two parallel boundaries. The resultant high density photons with a narrow frequency range are gathered around the edges of the panel to efficiently generate electric power through the attached solar cells, as shown in **Figure 5.1**.

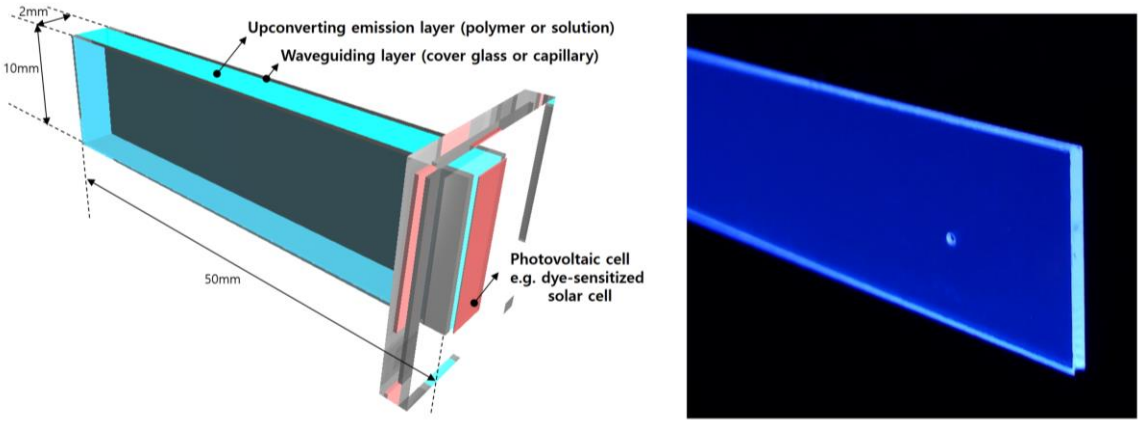

Figure 5.1. Proposed concept of triplet-fusion luminescent solar concentrator for solar energy harvesting.

5.2.2 Artificial photosynthesis for solar water-splitting

Photoelectrochemical water splitting using a particulate photocatalyst and inexhaustible solar energy has attracted significant attention as a potential means of large-scale hydrogen production from renewable resources, which avoids greenhouse gas production.[133] Because improving the efficiency of water-splitting reactions requires the device to be optimized in terms of its material selection and structure, developing new and more efficient photocatalysts has been important to harvest a large fraction of the solar spectrum. However, widely used semiconductor materials can absorb only photons within a fairly narrow wavelength range due to their higher bandgap than visible light. For example, the anatase phase of titanium dioxide has high photocatalytic activity, possesses a large bandgap of about 3.2 eV and absorption edge at 386 nm which lies in the near UV range. Thus the material is restricted from effectively utilizing solar photon energy. As a result, research efforts have been devoted to modifying traditional photocatalysts to shift the absorption threshold towards visible light or to look for new

carbon-based lower bandgap alternatives. Despite bandgap modifications, significant drawbacks such as relatively low efficiency of hydrogen evolution and production rate remain.

To achieve the 10% solar-to-hydrogen efficiency target, a semiconductor with a maximum bandgap of 2.3-2.4 eV is required.[134] An alternative strategy towards realizing sub-bandgap photon capture and conversion lies in the phenomenon of regenerative photochemical upconversion based on sensitized-TTA, a process that results in the frequency upconversion of sunlight (**Figure 5.2**). One of the proposed schemes is the D3 system, a three photon dual bandgap configuration where two photons with lower energy are involed in UC energy transfer and one photon with higher energy is directly absorbed into the photocatalyst per hydrogen molecule.[135] A key challenge for this artificial photosynthesis system is to utilize the electron-hole pairs generated by broad photon absorption and energy transfer to drive multi-electron chemistry. However, to date, there have been relatively few quantitative studies into the charge carrier dynamics related to system design with photon upconversion.

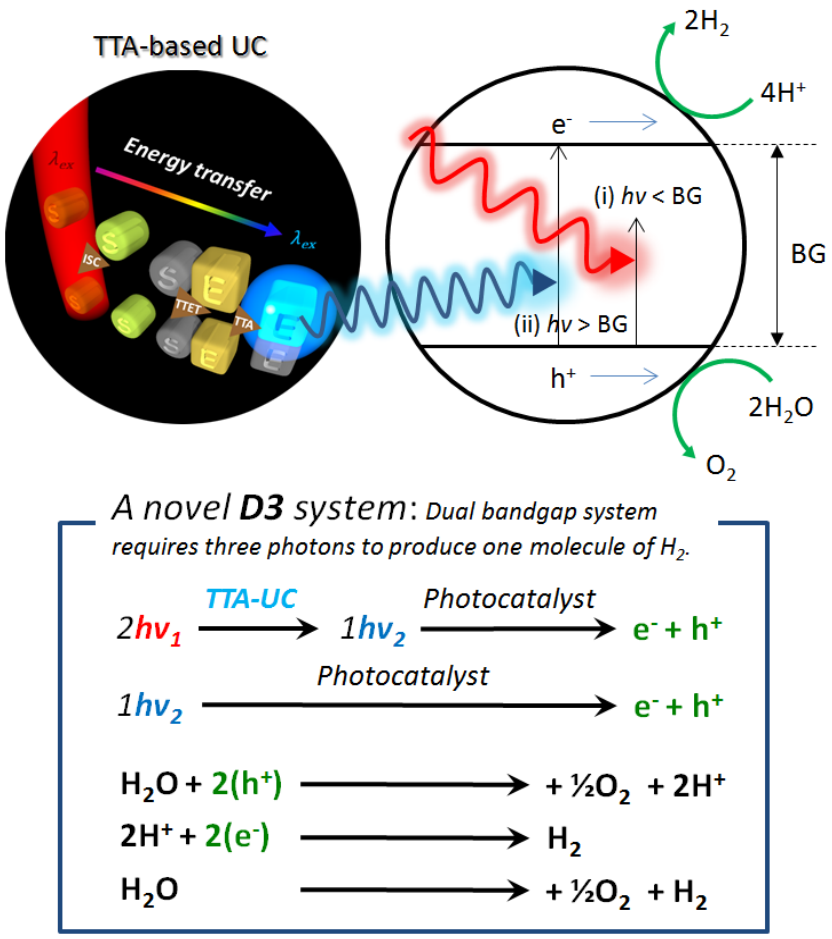

Figure 5.2. Proposed concept of photocatalytic water splitting system facilitated by sensitized triplet-fusion.

REFERENCES

1. West, W., Absorption of electromagnetic radiation. *AccessScience* **2014,** McGraw-Hill Education.

2. Jablonski, A., Efficiency of Anti-Stokes Fluorescence in Dyes. *Nature* **1933,** *131*, 839-840.

3. Franck, J.; Dymond, E. G., Elementary processes of photochemical reactions. *Transactions of the Faraday Society* **1926,** *21*, 536-542.

4. Condon, E., A Theory of Intensity Distribution in Band Systems. *Physical Review* **1926,** *28* (6), 1182-1201.

5. Kasha, M., Characterization of electronic transitions in complex molecules. *Discussions of the Faraday Society* **1950,** *9* (0), 14-19.

6. Lakowicz, J. R., Principles of Fluorescence Spectroscopy. *Springer US ed* **2006**.

7. Harriman, A., Electronic energy transfer. *Physical Chemistry Chemical Physics* **2010,** *12* (27), 7317-7318.

8. Skourtis, S. S.; Liu, C.; Antoniou, P.; Virshup, A. M.; Beratan, D. N., Dexter energy transfer pathways. *Proceedings of the National Academy of Sciences* **2016,** *113* (29), 8115-8120.

9. Th., F., Transfer Mechanisms of Electronic Excitation Energy. *Radiation Research Supplement* **1960,** *2*, 326-339.

10. Forster, T., 10th Spiers Memorial Lecture. Transfer mechanisms of electronic excitation. *Discussions of the Faraday Society* **1959,** *27* (0), 7-17.

11. Dexter, D. L., A Theory of Sensitized Luminescence in Solids. *The Journal of Chemical Physics* **1953,** *21* (5), 836-850.

12. Monguzzi, A.; Tubino, R.; Meinardi, F., Upconversion-induced delayed fluorescence in multicomponent organic systems: Role of Dexter energy transfer. *Physical Review B* **2008,** *77* (15), 155122.

13. de Wild, J.; Meijerink, A.; Rath, J. K.; van Sark, W. G. J. H. M.; Schropp, R. E. I., Upconverter solar cells: materials and applications. *Energy & Environmental Science* **2011,** *4* (12), 4835-4848.

14. Atre, A. C.; Dionne, J. A., Realistic upconverter-enhanced solar cells with non-ideal absorption and recombination efficiencies. *Journal of Applied Physics* **2011,** *110* (3), 034505.

15. Shan, G.-B.; Demopoulos, G. P., Near-Infrared Sunlight Harvesting in Dye-Sensitized Solar Cells Via the Insertion of an Upconverter-TiO2 Nanocomposite Layer. *Advanced Materials* **2010,** *22* (39), 4373-4377.

16. Cheng, Y. Y.; Fuckel, B.; MacQueen, R. W.; Khoury, T.; Clady, R. G. C. R.; Schulze, T. F.; Ekins-Daukes, N. J.; Crossley, M. J.; Stannowski, B.; Lips, K.; Schmidt, T. W., Improving the light-harvesting of amorphous silicon solar cells with photochemical upconversion. *Energy & Environmental Science* **2012,** *5* (5), 6953-6959.

17. Singh-Rachford, T. N.; Lott, J.; Weder, C.; Castellano, F. N., Influence of Temperature on Low-Power Upconversion in Rubbery Polymer Blends. *Journal of the American Chemical Society* **2009,** *131* (33), 12007-12014.

18. Zhang, Z.; Wang, W.; Yin, W.; Shang, M.; Wang, L.; Sun, S., Inducing photocatalysis by visible light beyond the absorption edge: Effect of upconversion agent on the photocatalytic activity of Bi2WO6. *Applied Catalysis B: Environmental* **2010,** *101* (1–2), 68-73.

19. Qin, W.; Zhang, D.; Zhao, D.; Wang, L.; Zheng, K., Near-infrared photocatalysis based on YF3 : Yb3+,Tm3+/TiO2 core/shell nanoparticles. *Chemical Communications* **2010,** *46* (13), 2304-2306.

20. Khnayzer, R. S.; Blumhoff, J.; Harrington, J. A.; Haefele, A.; Deng, F.; Castellano, F. N., Upconversion-powered photoelectrochemistry. *Chemical Communications* **2012,** *48* (2), 209-211.

21. Wang, F.; Han, Y.; Lim, C. S.; Lu, Y.; Wang, J.; Xu, J.; Chen, H.; Zhang, C.; Hong, M.; Liu, X., Simultaneous phase and size control of upconversion nanocrystals through lanthanide doping. *Nature* **2010,** *463* (7284), 1061-1065.

22. Miteva, T.; Yakutkin, V.; Nelles, G.; Baluschev, S., Annihilation assisted upconversion: all-organic, flexible and transparent multicolour display. *New Journal of Physics* **2008,** *10* (10), 103002.

23. Liu, Q.; Yang, T.; Feng, W.; Li, F., Blue-Emissive Upconversion Nanoparticles for Low-Power-Excited Bioimaging in Vivo. *Journal of the American Chemical Society* **2012,** *134* (11), 5390-5397.

24. Lim, S. F.; Riehn, R.; Ryu, W. S.; Khanarian, N.; Tung, C.-k.; Tank, D.; Austin, R. H., In Vivo and Scanning Electron Microscopy Imaging of Upconverting Nanophosphors in Caenorhabditis elegans. *Nano Letters* **2005,** *6* (2), 169-174.

25. Haase, M.; Schäfer, H., Upconverting Nanoparticles. *Angewandte Chemie International Edition* **2011,** *50* (26), 5808-5829.

26. Wohnhaas, C.; Turshatov, A.; Mailänder, V.; Lorenz, S.; Baluschev, S.; Miteva, T.; Landfester, K., Annihilation Upconversion in Cells by Embedding the Dye System in Polymeric Nanocapsules. *Macromolecular Bioscience* **2011,** *11* (6), 772-778.

27. Wang, F.; Deng, R.; Wang, J.; Wang, Q.; Han, Y.; Zhu, H.; Chen, X.; Liu, X., Tuning upconversion through energy migration in core–shell nanoparticles. *Nature Materials* **2011,** *10* (12), 968-973.

28. Baluschev, S.; Yakutkin, V.; Miteva, T.; Avlasevich, Y.; Chernov, S.; Aleshchenkov, S.; Nelles, G.; Cheprakov, A.; Yasuda, A.; Müllen, K.; Wegner, G., Blue-Green Up-Conversion: Noncoherent Excitation by NIR Light. *Angewandte Chemie International Edition* **2007,** *46* (40), 7693-7696.

29. Auzel, F., Upconversion and Anti-Stokes Processes with f and d Ions in Solids. *Chemical Reviews* **2003,** *104* (1), 139-174.

30. Suyver, J. F.; Aebischer, A.; Biner, D.; Gerner, P.; Grimm, J.; Heer, S.; Krämer, K. W.; Reinhard, C.; Güdel, H. U., Novel materials doped with trivalent lanthanides and transition metal ions showing near-infrared to visible photon upconversion. *Optical Materials* **2005,** *27* (6), 1111-1130.

31. Singh-Rachford, T. N.; Castellano, F. N., Photon upconversion based on sensitized triplet–triplet annihilation. *Coordination Chemistry Reviews* **2010,** *254* (21–22), 2560-2573.

32. Monguzzi, A.; Tubino, R.; Hoseinkhani, S.; Campione, M.; Meinardi, F., Low power, non-coherent sensitized photon up-conversion: modelling and perspectives. *Physical Chemistry Chemical Physics* **2012,** *14* (13), 4322-4332.

33. Islangulov, R. R.; Castellano, F. N., Photochemical Upconversion: Anthracene Dimerization Sensitized to Visible Light by a RuII Chromophore. *Angewandte Chemie International Edition* **2006,** *45* (36), 5957-5959.

34. Ji, S.; Guo, H.; Wu, W.; Wu, W.; Zhao, J., Ruthenium(II) Polyimine–Coumarin Dyad with Non-emissive 3IL Excited State as Sensitizer for Triplet–Triplet Annihilation Based Upconversion. *Angewandte Chemie International Edition* **2011,** *50* (36), 8283-8286.

35. Parker, C. A.; Hatchard, C. G., Delayed Fluorescence from Solutions of Anthracene and Phenathrene. *Proceedings of the Royal Society of London Series a-Mathematical and Physical Sciences* **1962,** *269* (1339), 574-584.

36. Parker, C. A.; Hatchard, C. G.; Joyce, T. A., Selective and Mutual Sensitization of Delayed Fluorescence. *Nature* **1965,** *205* (4978), 1282-1284.

37. Shockley, W.; Queisser, H. J., Detailed Balance Limit of Efficiency of p-n Junction Solar Cells. *Journal of Applied Physics* **1961,** *32* (3), 510-519.

38. Yeh, A. T.; Shank, C. V.; McCusker, J. K., Ultrafast Electron Localization Dynamics Following Photo-Induced Charge Transfer. *Science* **2000,** *289* (5481), 935-938.

39. Terenin, A.; Ermolaev, V., Sensitized phosphorescence in organic solutions at low temperature. Energy transfer between triplet states. *Transactions of the Faraday Society* **1956,** *52* (0), 1042-1052.

40. Saltiel, J.; March, G. R.; Smothers, W. K.; Stout, S. A.; Charlton, J. L., Spin-statistical factor in the triplet-triplet annihilation of anthracene triplets. *Journal of the American Chemical Society* **1981,** *103* (24), 7159-7164.

41. Birks, J. B., The quintet state of the pyrene excimer. *Physics Letters A* **1967,** *24* (9), 479-480.

42. Cheng, Y. Y.; Khoury, T.; Clady, R. G. C. R.; Tayebjee, M. J. Y.; Ekins-Daukes, N. J.; Crossley, M. J.; Schmidt, T. W., On the efficiency limit of triplet-triplet annihilation for photochemical upconversion. *Physical Chemistry Chemical Physics* **2010,** *12* (1), 66-71.

43. Haefele, A.; Blumhoff, J.; Khnayzer, R. S.; Castellano, F. N., Getting to the (Square) Root of the Problem: How to Make Noncoherent Pumped Upconversion Linear. *The Journal of Physical Chemistry Letters* **2012,** *3* (3), 299-303.

44. Monguzzi, A.; Mezyk, J.; Scotognella, F.; Tubino, R.; Meinardi, F., Upconversion-induced fluorescence in multicomponent systems: Steady-state excitation power threshold. *Physical Review B* **2008,** *78* (19), 195112.

45. Bachilo, S. M.; Weisman, R. B., Determination of Triplet Quantum Yields from Triplet−Triplet Annihilation Fluorescence. *The Journal of Physical Chemistry A* **2000,** *104* (33), 7711-7714.

46. Förster, T., Zwischenmolekulare Energiewanderung und Fluoreszenz. *Annalen der Physik* **1948,** *437* (1-2), 55-75.

47. Perrin, F., Loi de décroissance du pouvoir fluorescent en fonction de la concentration. *Comptes Rendus de l'Académie des Sciences* **1924,** *178*, 1978.

48. Inokuti, M.; Hirayama, F., Influence of Energy Transfer by the Exchange Mechanism on Donor Luminescence. *The Journal of Chemical Physics* **1965,** *43* (6), 1978-1989.

49. Speiser, S., Photophysics and Mechanisms of Intramolecular Electronic Energy Transfer in Bichromophoric Molecular Systems: Solution and Supersonic Jet Studies. *Chemical Reviews* **1996,** *96* (6), 1953-1976.

50. Avila, V.; Previtali, C. M.; Chesta, C. A., Free energy dependence of the diffusion-limited quenching rate constants in photoinduced electron transfer processes. *Photochemical & Photobiological Sciences* **2008,** *7* (1), 104-108.

51. Kang, J.-H.; Reichmanis, E., Low-Threshold Photon Upconversion Capsules Obtained by Photoinduced Interfacial Polymerization. *Angewandte Chemie International Edition* **2012,** *51* (47), 11841-11844.

52. Zhao, J.; Ji, S.; Guo, H., Triplet-triplet annihilation based upconversion: from triplet sensitizers and triplet acceptors to upconversion quantum yields. *RSC Advances* **2011,** *1* (6), 937-950.

53. Lees, A. J., Luminescence properties of organometallic complexes. *Chemical Reviews* **1987,** *87* (4), 711-743.

54. Gray, V.; Dzebo, D.; Abrahamsson, M.; Albinsson, B.; Moth-Poulsen, K., Triplet-triplet annihilation photon-upconversion: towards solar energy applications. *Physical Chemistry Chemical Physics* **2014,** *16* (22), 10345-10352.

55. Cheng, Y. Y.; Nattestad, A.; Schulze, T. F.; MacQueen, R. W.; Fuckel, B.; Lips, K.; Wallace, G. G.; Khoury, T.; Crossley, M. J.; Schmidt, T. W., Increased upconversion performance for thin film solar cells: a trimolecular composition. *Chemical Science* **2016,** *7* (1), 559-568.

56. Goldschmidt, J. C.; Fischer, S., Upconversion for Photovoltaics – a Review of Materials, Devices and Concepts for Performance Enhancement. *Advanced Optical Materials* **2015,** *3* (4), 510-535.

57. Jortner, J.; Choi, S.-i.; Katz, J. L.; Rice, S. A., Triplet Energy Transfer and Triplet-Triplet Interaction in Aromatic Crystals. *Physical Review Letters* **1963,** *11* (7), 323-326.

58. Steinberg, I. Z.; Katchalski, E., Theoretical Analysis of the Role of Diffusion in Chemical Reactions, Fluorescence Quenching, and Nonradiative Energy Transfer. *The Journal of Chemical Physics* **1968,** *48* (6), 2404-2410.

59. Thomas, D. D.; Carlsen, W. F.; Stryer, L., Fluorescence energy transfer in the rapid-diffusion limit. *Proceeding of the National Academy of Sciences* **1978,** *75* (12), 5746-5750.

60. Kohler, A.; Bassler, H., What controls triplet exciton transfer in organic semiconductors? *Journal of Materials Chemistry* **2011,** *21* (12), 4003-4011.

61. Islangulov, R. R.; Lott, J.; Weder, C.; Castellano, F. N., Noncoherent Low-Power Upconversion in Solid Polymer Films. *Journal of the American Chemical Society* **2007,** *129* (42), 12652-12653.

62. Kim, J.-H.; Deng, F.; Castellano, F. N.; Kim, J.-H., High Efficiency Low-Power Upconverting Soft Materials. *Chemistry of Materials* **2012,** *24* (12), 2250-2252.

63. Monguzzi, A.; Bianchi, F.; Bianchi, A.; Mauri, M.; Simonutti, R.; Ruffo, R.; Tubino, R.; Meinardi, F., High Efficiency Up-Converting Single Phase Elastomers for Photon Managing Applications. *Advanced Energy Materials* **2013,** *3* (5), 680-686.

64. Simon, Y. C.; Bai, S.; Sing, M. K.; Dietsch, H.; Achermann, M.; Weder, C., Low-Power Upconversion in Dye-Doped Polymer Nanoparticles. *Macromolecular Rapid Communications* **2012,** *33* (6-7), 498-502.

65. Monguzzi, A.; Frigoli, M.; Larpent, C.; Tubino, R.; Meinardi, F., Low-Power-Photon Up-Conversion in Dual-Dye-Loaded Polymer Nanoparticles. *Advanced Functional Materials* **2012,** *22* (1), 139-143.

66. Mahato, P.; Monguzzi, A.; Yanai, N.; Yamada, T.; Kimizuka, N., Fast and long-range triplet exciton diffusion in metal-organic frameworks for photon upconversion at ultralow excitation power. *Nature Materials* **2015,** *14* (9), 924-930.

67. Oldenburg, M.; Turshatov, A.; Busko, D.; Wollgarten, S.; Adams, M.; Baroni, N.; Welle, A.; Redel, E.; Wöll, C.; Richards, B. S.; Howard, I. A., Photon Upconversion at Crystalline Organic–Organic Heterojunctions. *Advanced Materials* **2016,** *28* (38), 8477-8482.

68. Mahato, P.; Yanai, N.; Sindoro, M.; Granick, S.; Kimizuka, N., Preorganized Chromophores Facilitate Triplet Energy Migration, Annihilation and Upconverted Singlet Energy Collection. *Journal of the American Chemical Society* **2016,** *138* (20), 6541-6549.

69. Sripathy, K.; MacQueen, R. W.; Peterson, J. R.; Cheng, Y. Y.; Dvorak, M.; McCamey, D. R.; Treat, N. D.; Stingelin, N.; Schmidt, T. W., Highly efficient photochemical upconversion in a quasi-solid organogel. *Journal of Materials Chemistry C* **2015,** *3* (3), 616-622.

70. Vadrucci, R.; Weder, C.; Simon, Y. C., Organogels for low-power light upconversion. *Materials Horizons* **2015,** *2* (1), 120-124.

71. Kim, J.-H.; Kim, J.-H., Encapsulated Triplet–Triplet Annihilation-Based Upconversion in the Aqueous Phase for Sub-Band-Gap Semiconductor Photocatalysis. *Journal of the American Chemical Society* **2012,** *134* (42), 17478-17481.

72. Tzenka, M.; Vladimir, Y.; Gabriele, N.; Stanislav, B., Annihilation assisted upconversion: all-organic, flexible and transparent multicolour display. *New Journal of Physics* **2008,** *10* (10), 103002.

73. Kwon, O. S.; Kim, J.-H.; Cho, J. K.; Kim, J.-H., Triplet–Triplet Annihilation Upconversion in CdS-Decorated SiO2 Nanocapsules for Sub-Bandgap Photocatalysis. *ACS Applied Materials & Interfaces* **2015,** *7* (1), 318-325.

74. Liu, Q.; Yin, B.; Yang, T.; Yang, Y.; Shen, Z.; Yao, P.; Li, F., A General Strategy for Biocompatible, High-Effective Upconversion Nanocapsules Based on Triplet–Triplet Annihilation. *Journal of the American Chemical Society* **2013,** *135* (13), 5029-5037.

75. Kim, J.-H.; Deng, F.; Castellano, F. N.; Kim, J.-H., Red-to-Blue/Cyan/Green Upconverting Microcapsules for Aqueous- and Dry-Phase Color Tuning and Magnetic Sorting. *ACS Photonics* **2014,** *1* (4), 382-388.

76. Olmsted, J., Calorimetric determinations of absolute fluorescence quantum yields. *The Journal of Physical Chemistry* **1979,** *83* (20), 2581-2584.

77. Abate, A. R.; Thiele, J.; Weitz, D. A., One-step formation of multiple emulsions in microfluidics. *Lab on a Chip* **2011,** *11* (2), 253-258.

78. Kim, S.-H.; Weitz, D. A., One-Step Emulsification of Multiple Concentric Shells with Capillary Microfluidic Devices. *Angewandte Chemie International Edition* **2011,** *50* (37), 8731-8734.

79. Lee, S. S.; Kim, S. K.; Won, J. C.; Kim, Y. H.; Kim, S.-H., Reconfigurable Photonic Capsules Containing Cholesteric Liquid Crystals with Planar Alignment. *Angewandte Chemie International Edition* **2015,** *54* (50), 15266-15270.

80. Guillot, P.; Colin, A.; Utada, A. S.; Ajdari, A., Stability of a Jet in Confined Pressure-Driven Biphasic Flows at Low Reynolds Numbers. *Physical Review Letters* **2007,** *99* (10), 104502.

81. Humphry, K. J.; Ajdari, A.; Fernández-Nieves, A.; Stone, H. A.; Weitz, D. A., Suppression of instabilities in multiphase flow by geometric confinement. *Physical Review E* **2009,** *79* (5), 056310.

82. Utada, A. S.; Lorenceau, E.; Link, D. R.; Kaplan, P. D.; Stone, H. A.; Weitz, D. A., Monodisperse Double Emulsions Generated from a Microcapillary Device. *Science* **2005,** *308* (5721), 537-541.

83. McGlynn, S. P.; Daigre, J.; Smith, F. J., External Heavy-Atom Spin—Orbital Coupling Effect. IV. Intersystem Crossing. *The Journal of Chemical Physics* **1963,** *39* (3), 675-679.

84. McCarthy, W. J.; Dunlap®, K. L., Solvents showing the external heavy atom effect in phosphorimetry. *Talanta* **1970,** *17* (4), 305-317.

85. Schmidt, T. W.; Castellano, F. N., Photochemical Upconversion: The Primacy of Kinetics. *The Journal of Physical Chemistry Letters* **2014,** *5* (22), 4062-4072.

86. Mitov, M., Cholesteric Liquid Crystals with a Broad Light Reflection Band. *Advanced Materials* **2012,** *24* (47), 6260-6276.

87. Tamaoki, N., Cholesteric Liquid Crystals for Color Information Technology. *Advanced Materials* **2001,** *13* (15), 1135-1147.

88. Choi, S. S.; Morris, S. M.; Huck, W. T. S.; Coles, H. J., Electrically Tuneable Liquid Crystal Photonic Bandgaps. *Advanced Materials* **2009,** *21* (38-39), 3915-3918.

89. White, T. J.; McConney, M. E.; Bunning, T. J., Dynamic color in stimuli-responsive cholesteric liquid crystals. *Journal of Materials Chemistry* **2010,** *20* (44), 9832-9847.

90. Li, Y.; Urbas, A.; Li, Q., Reversible Light-Directed Red, Green, and Blue Reflection with Thermal Stability Enabled by a Self-Organized Helical Superstructure. *Journal of the American Chemical Society* **2012,** *134* (23), 9573-9576.

91. Lee, S. S.; Kim, B.; Kim, S. K.; Won, J. C.; Kim, Y. H.; Kim, S.-H., Robust Microfluidic Encapsulation of Cholesteric Liquid Crystals Toward Photonic Ink Capsules. *Advanced Materials* **2015,** *27* (4), 627-633.

92. Aβhoff, S. J.; Sukas, S.; Yamaguchi, T.; Hommersom, C. A.; Le Gac, S.; Katsonis, N., Superstructures of chiral nematic microspheres as all-optical switchable distributors of light. *Scientific Reports* **2015,** *5*, 14183.

93. Finkelmann, H.; Kim, S. T.; Muñoz, A.; Palffy-Muhoray, P.; Taheri, B., Tunable Mirrorless Lasing in Cholesteric Liquid Crystalline Elastomers. *Advanced Materials* **2001,** *13* (14), 1069-1072.

94. Coles, H.; Morris, S., Liquid-crystal lasers. *Nature Photonics* **2010,** *4* (10), 676-685.

95. Uchida, Y.; Takanishi, Y.; Yamamoto, J., Controlled Fabrication and Photonic Structure of Cholesteric Liquid Crystalline Shells. *Advanced Materials* **2013,** *25* (23), 3234-3237.

96. Zhu, J.-L.; Li, W.-H.; Sun, Y.; Lu, J.-G.; Song, X.-L.; Chen, C.-Y.; Zhang, Z.; Su, Y., Random laser emission in a sphere-phase liquid crystal. *Applied Physics Letters* **2015,** *106* (19), 191903.

97. Fernández-Nieves, A.; Vitelli, V.; Utada, A. S.; Link, D. R.; Márquez, M.; Nelson, D. R.; Weitz, D. A., Novel Defect Structures in Nematic Liquid Crystal Shells. *Physical Review Letters* **2007,** *99* (15), 157801.

98. Humar, M.; Muševič, I., 3D microlasers from self-assembled cholesteric liquid-crystal microdroplets. *Optics Express* **2010,** *18* (26), 26995-27003.

99. Chen, L.; Li, Y.; Fan, J.; Bisoyi, H. K.; Weitz, D. A.; Li, Q., Photoresponsive Monodisperse Cholesteric Liquid Crystalline Microshells for Tunable Omnidirectional Lasing Enabled by a Visible Light-Driven Chiral Molecular Switch. *Advanced Optical Materials* **2014,** *2* (9), 845-848.

100. Zapotocky, M.; Ramos, L.; Poulin, P.; Lubensky, T. C.; Weitz, D. A., Particle-Stabilized Defect Gel in Cholesteric Liquid Crystals. *Science* **1999,** *283* (5399), 209-212.

101. Geng, Y.; Noh, J.; Drevensek-Olenik, I.; Rupp, R.; Lenzini, G.; Lagerwall, J. P. F., High-fidelity spherical cholesteric liquid crystal Bragg reflectors generating unclonable patterns for secure authentication. *Scientific Reports* **2016,** *6*, 26840.

102. Darmon, A.; Benzaquen, M.; Seč, D.; Čopar, S.; Dauchot, O.; Lopez-Leon, T., Waltzing route toward double-helix formation in cholesteric shells. *Proceedings of the National Academy of Sciences* **2016,** *113* (34), 9469-9474.

103. Noh, J.; Liang, H.-L.; Drevensek-Olenik, I.; Lagerwall, J. P. F., Tuneable multicoloured patterns from photonic cross-communication between cholesteric liquid crystal droplets. *Journal of Materials Chemistry C* **2014,** *2* (5), 806-810.

104. Kopp, V. I.; Fan, B.; Vithana, H. K. M.; Genack, A. Z., Low-threshold lasing at the edge of a photonic stop band in cholesteric liquid crystals. *Optics Letters* **1998,** *23* (21), 1707-1709.

105. Gramotnev, D. K.; Bozhevolnyi, S. I., Plasmonics beyond the diffraction limit. *Nature Photonics* **2010,** *4* (2), 83-91.

106. de Leon, N. P.; Shields, B. J.; Yu, C. L.; Englund, D. E.; Akimov, A. V.; Lukin, M. D.; Park, H., Tailoring Light-Matter Interaction with a Nanoscale Plasmon Resonator. *Physical Review Letters* **2012,** *108* (22), 226803.

107. Nguyen, H.; Park, J.; Kang, S.; Kim, M., Surface Plasmon Resonance: A Versatile Technique for Biosensor Applications. *Sensors* **2015,** *15* (5), 10481.

108. Christopher, P.; Xin, H.; Linic, S., Visible-light-enhanced catalytic oxidation reactions on plasmonic silver nanostructures. *Nature Chemistry* **2011,** *3* (6), 467-472.

109. Atwater, H. A.; Polman, A., Plasmonics for improved photovoltaic devices. *Nature Materials* **2010,** *9* (3), 205-213.

110. Homola, J.; Yee, S. S.; Gauglitz, G., Surface plasmon resonance sensors: review. *Sensors and Actuators B: Chemical* **1999,** *54* (1–2), 3-15.

111. Yu, H.; Shan, X.; Wang, S.; Chen, H.; Tao, N., Plasmonic Imaging and Detection of Single DNA Molecules. *ACS Nano* **2014,** *8* (4), 3427-3433.

112. Mansuripur, M.; Zakharian, A. R.; Lesuffleur, A.; Oh, S.-H.; Jones, R. J.; Lindquist, N. C.; Im, H.; Kobyakov, A.; Moloney, J. V., Plasmonic nano-structures for optical data storage. *Opt. Express* **2009,** *17* (16), 14001-14014.

113. Hutter, E.; Fendler, J. H., Exploitation of Localized Surface Plasmon Resonance. *Advanced Materials* **2004,** *16* (19), 1685-1706.

114. Ming, T.; Chen, H.; Jiang, R.; Li, Q.; Wang, J., Plasmon-Controlled Fluorescence: Beyond the Intensity Enhancement. *The Journal of Physical Chemistry Letters* **2012,** *3* (2), 191-202.

115. Nikoobakht, B.; El-Sayed, M. A., Preparation and Growth Mechanism of Gold Nanorods (NRs) Using Seed-Mediated Growth Method. *Chemistry of Materials* **2003,** *15* (10), 1957-1962.

116. Lohse, S. E.; Murphy, C. J., The Quest for Shape Control: A History of Gold Nanorod Synthesis. *Chemistry of Materials* **2013,** *25* (8), 1250-1261.

117. Pérez-Juste, J.; Pastoriza-Santos, I.; Liz-Marzán, L. M.; Mulvaney, P., Gold nanorods: Synthesis, characterization and applications. *Coordination Chemistry Reviews* **2005,** *249* (17–18), 1870-1901.

118. Orendorff, C. J.; Sau, T. K.; Murphy, C. J., Shape-Dependent Plasmon-Resonant Gold Nanoparticles. *Small* **2006,** *2* (5), 636-639.

119. Jana, N. R.; Gearheart, L.; Murphy, C. J., Seed-Mediated Growth Approach for Shape-Controlled Synthesis of Spheroidal and Rod-like Gold Nanoparticles Using a Surfactant Template. *Advanced Materials* **2001,** *13* (18), 1389-1393.

120. Rodríguez-Fernández, J.; Pérez-Juste, J.; Mulvaney, P.; Liz-Marzán, L. M., Spatially-Directed Oxidation of Gold Nanoparticles by Au(III)−CTAB Complexes. *The Journal of Physical Chemistry B* **2005,** *109* (30), 14257-14261.

121. Tsung, C.-K.; Kou, X.; Shi, Q.; Zhang, J.; Yeung, M. H.; Wang, J.; Stucky, G. D., Selective Shortening of Single-Crystalline Gold Nanorods by Mild Oxidation. *Journal of the American Chemical Society* **2006,** *128* (16), 5352-5353.

122. Ni, W.; Kou, X.; Yang, Z.; Wang, J., Tailoring Longitudinal Surface Plasmon Wavelengths, Scattering and Absorption Cross Sections of Gold Nanorods. *ACS Nano* **2008,** *2* (4), 677-686.

123. Jana, N. R.; Gearheart, L.; Obare, S. O.; Murphy, C. J., Anisotropic Chemical Reactivity of Gold Spheroids and Nanorods. *Langmuir* **2002,** *18* (3), 922-927.

124. Zou, R.; Guo, X.; Yang, J.; Li, D.; Peng, F.; Zhang, L.; Wang, H.; Yu, H., Selective etching of gold nanorods by ferric chloride at room temperature. *CrystEngComm* **2009,** *11* (12), 2797-2803.

125. Link, S.; Burda, C.; Nikoobakht, B.; El-Sayed, M. A., Laser-Induced Shape Changes of Colloidal Gold Nanorods Using Femtosecond and Nanosecond Laser Pulses. *The Journal of Physical Chemistry B* **2000,** *104* (26), 6152-6163.

126. Sohn, K.; Kim, F.; Pradel, K. C.; Wu, J.; Peng, Y.; Zhou, F.; Huang, J., Construction of Evolutionary Tree for Morphological Engineering of Nanoparticles. *ACS Nano* **2009,** *3* (8), 2191-2198.

127. Ye, X.; Jin, L.; Caglayan, H.; Chen, J.; Xing, G.; Zheng, C.; Doan-Nguyen, V.; Kang, Y.; Engheta, N.; Kagan, C. R.; Murray, C. B., Improved Size-Tunable Synthesis of Monodisperse Gold Nanorods through the Use of Aromatic Additives. *ACS Nano* **2012,** *6* (3), 2804-2817.

128. Hassan, P. A.; Yakhmi, J. V., Growth of Cationic Micelles in the Presence of Organic Additives. *Langmuir* **2000,** *16* (18), 7187-7191.

129. Lin, Z.; Cai, J. J.; Scriven, L. E.; Davis, H. T., Spherical-to-Wormlike Micelle Transition in CTAB Solutions. *The Journal of Physical Chemistry* **1994,** *98* (23), 5984-5993.

130. Lakowicz, J. R., Radiative decay engineering 5: metal-enhanced fluorescence and plasmon emission. *Analytical Biochemistry* **2005,** *337* (2), 171-194.

131. Wu, W.-C.; Tracy, J. B., Large-Scale Silica Overcoating of Gold Nanorods with Tunable Shell Thicknesses. *Chemistry of Materials* **2015,** *27* (8), 2888-2894.

132. Fernández-López, C.; Mateo-Mateo, C.; Álvarez-Puebla, R. A.; Pérez-Juste, J.; Pastoriza-Santos, I.; Liz-Marzán, L. M., Highly Controlled Silica Coating of PEG-Capped Metal Nanoparticles and Preparation of SERS-Encoded Particles. *Langmuir* **2009,** *25* (24), 13894-13899.

133. Tachibana, Y.; Vayssieres, L.; Durrant, J. R., Artificial photosynthesis for solar water-splitting. *Nature Photonics* **2012,** *6* (8), 511-518.

134. Abdi, F. F.; Han, L.; Smets, A. H. M.; Zeman, M.; Dam, B.; van de Krol, R., Efficient solar water splitting by enhanced charge separation in a bismuth vanadate-silicon tandem photoelectrode. *Nature Communications* **2013,** *4*.

135. Walter, M. G.; Warren, E. L.; McKone, J. R.; Boettcher, S. W.; Mi, Q.; Santori, E. A.; Lewis, N. S., Solar Water Splitting Cells. *Chemical Reviews* **2010,** *110* (11), 6446-6473.